MULTI-SCALE NONLINEAR CONSTITUTIVE MODELS USING ARTIFICIAL NEURAL NETWORKS

A Dissertation
Presented to
The Academic Faculty

By

Hoan-Kee Kim

In Partial Fulfillment
Of the Requirements for the Degree
Doctor of Philosophy in the
School of Civil & Environmental Engineering

Georgia Institute of Technology

April 2008

MULTI-SCALE NONLINEAR CONSTITUTIVE MODELS
USING
ARTIFICIAL NEURAL NETWORKS

Approved by:

Dr. Rami M. Haj-Ali, Advisor
School of Civil & Environmental Engineering
Georgia Institute of Technology

Dr. Arash Yavari
School of Civil & Environmental Engineering
Georgia Institute of Technology

Dr. Kenneth M. Will
School of Civil & Environmental Engineering
Georgia Institute of Technology

Dr. Erian A. Armanios
School of Aerospace Engineering
Georgia Institute of Technology

Dr. Donald W. White
School of Civil & Environmental Engineering
Georgia Institute of Technology

Date Approved: Mar. 04, 2008

ACKNOWLEDGEMENTS

I would like to thank to my advisor Dr. Rami M Haj-Ali for his academic guidance, encouragement, and valuable advice for my doctoral research at Georgia Tech. It was a great experience to work and collaborate with him for completing my Ph.D. dissertation. My appreciation also goes to my committee members for providing their insightful and valuable comments on my thesis: Dr. Donald White, Dr. Kenneth Will, Dr. Arash Yavari, and Dr. Erian Armanios.

I also would like to thank to my friends and office mates for sharing our time and experience: Sekwon Jung, Gwangseok Na, Joonho Choi, Heesun Kim, Shane Johnson, Bo-Siou Wei, Yoonduk Kim, Cagri Ozgur, and Dai Tran. My gratitude also goes to all of my friends in CEE at Georgia Tech. I would like to thank Sail Lee, Jinseok Jun, and their families for spending our time together.

Deepest thanks and love go to my family for their endless patience and support: father Jin-Hong Kim, mother Soon-Nam Lee, sister Yeun-Hee Kim, my wife Eun-Jung Shin, and my son Matthew Nam-Hyuk Kim. Their love was the most important source for me to overcome many obstacles faced for my four and half year journey at Georgia Tech. I believe that my family continues to give me their unconditional love that they have showed me. I dedicate this thesis to my family and lord.

.

TABLE OF CONTENTS

LIST OF TABLES

LIST OF FIGURES

SUMMARY

This study presents a new approach for nonlinear multi-scale constitutive models using artificial neural networks (ANNs). Three ANN classes are proposed to characterize the nonlinear multi-axial stress-strain behavior of metallic, polymeric, and fiber reinforced polymeric (FRP) materials, respectively. Load-displacement responses from nanoindentation of metallic and polymeric materials are used to train new generation of dimensionless ANN models with different micro-structural properties as additional variables to the load-deflection. The proposed ANN models are effective in inverse-problems set to back-calculate in-situ material parameters from given overall nanoindentation test data with/without time-dependent material behavior. Towards that goal, nanoindentation tests have been performed for silicon (Si) substrate with/without a copper (Cu) film. Nanoindentation creep test data, available in the literature for Polycarbonate substrate, are used in these inverse problems. The predicted properties from the ANN models can also be used to calibrate classical constitutive parameters. The third class of ANN models is used to generate the effective multi-axial stress-strain behavior of FRP composites under plane-stress conditions. The training data are obtained from coupon tests performed in this study using off-axis tension/compression and pure shear tests for pultruded FRP E-glass/polyester composite systems. It is shown that the trained nonlinear ANN model can be directly coupled with finite-element (FE) formulation as a material model at the Gaussian integration points of each layered-shell element. This FE-ANN modeling approach is applied to simulate an FRP plate with an open-hole and compared with experimental results. Micromechanical nonlinear ANN models with damage formulation are also formulated and trained using simulated FE modeling of the periodic microstructure. These new multi-scale ANN constitutive models are effective and can be extended by including more material variables to capture complex material behavior, such as softening due to micro-structural damage or failure.

CHAPTER 1: Literature Review

Full scale mechanical constitutive models are important for traditional and newly developed material systems in order to sustain larger loads and operate under severe environmental conditions. Material manufacturing technology has been tremendously advanced over the last decade in part due to the ability to simulate the mechanical behavior at sub-micron levels. Today, material and structural components can be designed with constituent properties captured at the different macro-meso-micro-nano scales. Therefore, materials can be "engineered" to become stronger, lighter, and more durable. On the other hand, the analysis and design of structures made of advanced materials has become more complicated because of nonlinear behaviors (e.g., plasticity and viscosity) that need to be addressed in order to achieve higher performance without failure. Recent innovative mathematical and analytical constitutive methods are collectively called multi-scale models that can utilize micro-to-nano variables needed to describe complex nonlinear and damage behaviors, e.g., microcrack formulations, dislocations, and slips in metals, and fiber breaking and matrix failure in composites. These multi-scale models may include some limitations due to their complexity in calibrating in-situ coefficients, applicability in narrow ranges of material response, or accuracy in predicting highly nonlinear material behaviors. Thus, there is a need for mechanical characterization and constitutive methods that can generate models able to predict full-scale complex behaviors. Artificial neural network (ANN) has been recently used to generate macro-and micro-scale constitutive material models. This study integrates and proposes new ANN macro and micro constitutive material models for several metallic and composite material systems.

Artificial neural network (ANN) models can advance and expand the accuracy and applicability of the traditional mathematical tools used to describe phenomenological constitutive models. In general, the latter are accurate mathematical models and can have relatively many

coefficients that need to be calibrated with experimental data. The coefficient or parameter calibration process needs to be carefully performed to acquire good accuracy in any material model. Classical constitutive models may be applied at a select range of variables. In order to expand their applicability to approximate new range of behavior, adding more coefficients or state variables may be needed. This modeling upgrade needs to perform re-calibration and verification processes, again. This requires many computational and experimental efforts. On the other hand, the ANN modeling approach is relatively easier and can have wider range of capability by adding neurons and adjusting connection weights among artificial neurons. This computational paradigm is borrowed from nature. It brings powerful applicability and can control accuracy of the ANN response. The ANN models can be trained based on experimental tests and/or mechanical simulation of micro-structures to generate a wide class of material constitutive models capable of predicting the mechanical response of the material in the given history of deformations. For example, once accurate ANN models have been trained, discrepancies and noise found in the given data can be eliminated. This has been the case for fiber reinforced polymeric (FRP) composites, where a full stress-strain variable field cannot be described by classical mathematical models to depict irregular mechanical behavior, e.g., pre- and post-damage along with highly nonlinear stress-strain responses in local directions. The proposed ANN (implicit) modeling is relatively easier and more powerful to be used in this case.

Another major advantage of ANN material modeling approach is that it can be efficiently used in solving inverse problems where in-situ material properties are needed. Due to the nature of ANNs (e.g., memory, fault and noise tolerance, generalization), ANN models can be directly constructed with variables more suited for inverse problems. This can be easily expressed by proper selection of the relations between input and output variables more than the classical approach. It is not easy to characterize the mechanical properties of nano-scaled materials using traditional experimental methods because these are easily influenced by different factors (e.g., small vibration caused by a hydraulic pump or an actuator) that were not significant in macro-scale testing. For

example, only limited material properties (e.g., elastic modulus and hardness) can be obtained from nanoindentation tests. Thus, many researchers have tried to use mathematical or analytical models with an FEA to characterize the material properties of thin films by matching their results with nanoindentation tests results. This mathematical approach is either limited in a specific material system (e.g., single-layered films) or inefficient because it requires much computational time to perform an FEA for every change in the FE model. The proposed ANN modeling approach can be used to generate nanoindentation models from test results (e.g., load-displacement responses). Different in-situ parameters can be added to this ANN model allowing it to capture the influence of the nano or micro-structure on the overall behaviors. Thus, an inverse problem can be later formulated using a trained ANN model. This can save huge computational effort in an inverse problem where much iteration is required. The efficiency of the ANN approach is incomparable to other mathematical approaches in solving an inverse problem (e.g., characterizing nonlinear material parameters and creep compliances from nanoindentation or nanoindentation creep tests).

The following sections present a needed background and a literature review of significant studies that have been published in the general areas of constitutive modeling with emphasis on nonlinear behavior. These models are used to generate material relations for traditional engineering materials (e.g., metal and concrete), as well as advanced composite materials (e.g., FRP composites and multi-layered films in nano-scale) using both mathematical and ANN approaches. The final section of this chapter addresses the motivations, objectives, and research approaches of this study.

1.1 Classical Constitutive Models for Isotropic Metallic Materials

Metals have been often considered as isotropic homogeneous materials for the simplification in analyzing and designing metal structures. Many researchers such as Hart (1976), Swearengen et al. (1976), and Wire et al. (1975) have proposed phenomenological constitutive models based on the

observation of inelastic deformation behaviors. Hart (1976) proposed incremental viscoplastic constitutive relations for the inelastic deformation of metals based on a phenomenological theory, where the current deformation state of the metal can be approximated using stress and state variables. Ghosh (1980) proposed a constitutive model that can represent different deformation behaviors caused by combinations of different strain hardening, strain rate, and temperature of the metals under monotonic or dynamic loading conditions. Standard experiments were performed, such as tensile and creep tests, to examine the prediction ability of the proposed model. Wilkins and Guinan (1973) proposed an empirical equation, which was derived from the cylindrical length decrease and axial strain rate, in order to determine the yield strength of metal cylinders. Steinberg et al. (1980) presented an empirical constitutive model for isotropic metallic materials. In their study, the shear modulus and the yield strength are functions of the plastic strain, pressure, and internal energy. Numerous nonlinear constitutive models have been generated over the last four decades with different simplification and sophistications. Several books have been the sole subject of inelastic constitutive formulations, e.g. Chen and Saleeb (1982), Chen et al. (1994), and Simo and Hughes (2000). However, this field continues to evolve because there is a need to accurately describe the complex behavior of new and existing engineering materials.

1.2 Anisotropic (Composite) Material Models for FRP Composites

Fiber reinforced plastic (FRP) composite materials are advantageous due to their light weight to strength ratio, corrosion resistance, and durability. Composite materials, especially laminated composites, are being increasingly used due to their easy manufacturing in accordance with their strength required. They can be designed by stacking or arranging laminates along with a specific direction. This leads a need to analyze and identify the material properties of the newly designed or manufactured composite materials. Thus, nonlinear constitutive models have been addressed for the better understanding of composite material behaviors. Petit and Waddoups (1969) proposed an

incremental approach to determine the stress-strain response for a symmetric laminated composite, which is composed of an orthotropic constituent lamina under the bi-axial membrane loading. The stress-strain responses of the constituent lamina were empirically obtained from tension, compression, and shear tests. The stress-strain responses of laminated composite were obtained from the lamina constitutive relationship. In order to analyze the stress-strain response of a laminated composite past ultimate response, they considered that the tangent stiffness of a lamina may have negative values when the stiffness reaches to the yield strength of the lamina. They compared their analysis results with experiments. Their proposed method can predict the overall laminate response very well. Hahn and Tsai (1973) used nonlinear terms in the complementary elastic energy density to derive a nonlinear elastic stress-strain relation for a composite lamina. The constitutive relationship was determined using a second-order polynomial energy density function, in addition to the fourth-order constant added to exhibit nonlinear shear response. Hahn (1973) extended this work to consider the nonlinear behavior of laminates and studied the effect of this nonlinearity reducing the buckling load. Jones and Nelson (1975) proposed a material model expressed in terms of the strain energy density to consider the nonlinear behavior under biaxial states of stresses. Pindera and Herakovich (1983) derived the nonlinear constitutive model using irreversible thermodynamics with internal variables under off-axis tensile load. Griffin et al. (1981) proposed an incremental plastic flow theory based on Hill's orthotropic yield criterion. They used a uniaxial Ramberg-Osgood stress-strain relationship to consider nonlinear hardening for laminated composites. Sun and Chen (1989) proposed a one-parameter orthotropic plasticity model for unidirectional composites. They derived the incremental plastic stress-strain relationship based on one-parameter and using a flow rule. In order to derive this relationship, they ignored the plastic deformation in the fiber direction.

Micromechanical models of heterogeneous materials have been extensively studied in order to characterize the effective material properties of homogenized effective anisotropic medium. Many researchers have proposed analytical and phenomenological micro-models. Paul (1960), Hashin

(1962), and Hill (1964) are among the first to propose analytically-based micro-mechanical models for composites. Hill (1964) proposed micro mechanical models using concentration factors to represent stresses and strains in both fiber and matrix in terms of average stress and strain. This model has been often compared with Voigt (1889) and Reuss (1929) models, referred to as upper and lower boundary models, respectively. Hashin and Rosen (1964) formulated a concentric cylinder assemblage (CCA) model. They assumed that the representative volume element (RVE) is cylindrical, and the size and shape of fibers and matrices are constant along with the longitudinal direction. Their model is considered to be more appropriate for transversely isotropic composite materials. Based on these classical micromechanical approaches, other micromechanical models have been proposed, e.g., Avery and Herakovich (1986), Knott and Herakovich (1988, 1991), and Hashin (1990).

The previous analytically-based micromechanical models are either less effective to generate nonlinear material behaviors or unable to produce the full multi-axial effective nonlinear material behavior. Another micromechanical models referred to as the method of cells (MOC) have been proposed by Aboudi (1991). The MOC is developed assuming a periodic medium with fibers having rectangular shape cross-sections surrounded by matrix sub-cells unlike the previously developed micromechanical models. Paley and Aboudi (1992) generalize this method to represent effective material properties using several sub-cells with full compatibility and traction continuity formulation. Their models can be used as 2D and 3D micromechanical models. Haj-Ali et al. (1993, 1996, 2001, and 2004) used new incremental formulations well-suited for global-local multi-scale analysis of composite materials. Haj-Ali and Kilic (2002, 2003) proposed nonlinear macro- and micro-mechanical models for thick-section FRP composites. Their models can generate accurate nonlinear structural behaviors by adding iterative correction scheme with formulation equivalent to the MOC. Their models were able to well capture the multi-axial responses. Haj-Ali and Muliana (2003, 2004, and 2006) have used their micro-models to generate the nonlinear mechanical and time-dependent

behavior of the FRP composite. This nonlinear micro-modeling approach is capable of generating the nonlinear and multi-axial effective stress-strain behavior. However, local effects, such as fiber-matrix interface stresses are not accurate.

1.3 Simulation and Testing of Nanoindentation

Nanoindentation

Material properties of thin film or coating having thickness in the micro to nano-meter scale could not be characterized using the standard mechanical testing that is used to determine properties of bulk materials (e.g., uniaxial, biaxial, torsion testing.) This is due to the geometric limitation of the materials (i.e., inability to grip the thin-film specimen.) For several decades, nanoindentation technique has been utilized to determine limited material properties such as elastic modulus and hardness of bulk or thin film materials. Oliver and Pharr (1992) are among the first to use the indentation technique with Berkovich indenter for characterizing mechanical behaviors of fused silica, soda-lime glass, and single crystals of aluminum, tungsten, quartz, and sapphire. The load-displacement responses during unloading stage were used to determine the elastic modulus and hardness of these materials. Bhattacharya and Nix (1991) generated a 2D FE model to simulate indentation with conical indenter. They investigated the effect on different indenter angles and different elastic-plastic material behaviors on the shapes of plastic zone under the contact area. The responses from the FE simulation are comparable to the ones obtained from the experimental tests. Sun et al. (1995) used a 2D FE simulation to investigate the effects of indenting a hard coating on a soft substrate and identify relationships between the ratio of the coating thickness to the indentation depth and the ratio of the coating's yield strength to the one of the substrate. They concluded that these relationships can be used to determine suitable indentation depths for various combinations of coating and substrate materials. Vlachos et al. (2001) used 3D FE simulations to study indentation on a hard film placed on a soft substrate, while Panich and Sun (2004) performed FE simulations of

indentation on a soft film with hard substrate. Choi et al. (2004) proposed an analytical solution to determine the effects of tip-blunting and pile-up during indentation on the contact area. The solution was derived from observing a relationship between contact areas and indention depths influenced by the elastic modulus, pile-up, and sink-in from indentation experiments and FE simulations.

Recently, nanoindentation technique has been used to investigate material behaviors in the micro-structural level, i.e., size-effect on the plastic deformation of the materials at the continuum level. Abu Al-Rub and Voyiadjis (2004, 2006) derived an analytical solution for the deformation-gradient-plasticity with measurable physical parameters in the micro-structural level to explain the size effect that can be observed at micro- to macro-scale. They suggest that their work can be used to identify length-scale parameters from indentation tests for both spherical and pyramidal indenters. Other related studies on the size effect on the plastic deformation of materials using nanoindentation tests and FE simulations can be found in Hwang et al. (2005), Qu et al. (2006), Wei et al. (2005), and Zhang et al. (2007). Indentation technique has also been applied to characterize plastic deformation of different advanced materials, e.g., nano silicon particles, shape memory alloys, etc. (Gerberich et al., 2005 and Pan et al., 2007).

Nanoindentation creep

For the past five years, micro- and nanoindentation tests have been used to characterize material properties with time-dependent behaviors. The studies are mainly investigated on bulk and thin film polymers. The following loading histories are commonly performed: ramp loading with various constant loading rates, creep loading where the load is held constant, and unloading with constant rates. Experimental studies have been performed to investigate the effect of loading rate, holding period, and indenter shape on the time-dependent material characterization. Lu et al. (2003) measured creep compliance on bulk polymethyl methacrylate (PMMA) and polycarbonate (PC) using indentation tests with Berkovich and spherical indenters. Creep functions based on Kelvin-Voigt

model were used. The calibrated materials parameters from the indentation tests agreed well with the ones obtained from conventional uniaxial tension and shear tests. Oyen (2005) performed creep tests with different combinations of loading ramp rates and peak load levels on glassy and rubbery polymeric materials. The Boltzmann integral model was used to generate displacement-time responses during the indentation testing with spherical indenter. The experimental data were used to calibrate the time-dependent modulus. Good agreement was found between the experimental and modeling results. Zhang et al. (2004) used the combination of Maxwell and Voigt elements to generate creep response by indenting polymeric thin film on a hard elastic substrate. They demonstrated that this model is capable of predicting time-dependent responses of film-substrate combinations (e.g., glassy polyurethane-polyester).

Analytical solutions have been proposed to characterize time-dependent material properties from experimental data. Maxwell and Kelvin mechanical analog models are often used to represent the time-dependent material functions. Feng and Ngan (2002), Oyen and Cook (2003), Fang and Chang (2004) have investigated the loading rate effects in characterizing the time-dependent modulus and hardness of materials. Sakai and Shimizu (2001) derived an analytical solution that includes effects of materials' viscosity and indenter shapes to examine the time-dependent indentation response. Yang et al. (2004) proposed a semi-empirical method to study nanoindentation creep behaviors for various amorphous polymers, i.e., PMMA, polycarbonate, polystyrene, polyester, and epoxy, using flat-ended tip indenter. The curve-fitting method is used to calibrate material properties. They demonstrated that calibrated material parameters could predict creep displacements under load levels that were not used in the calibration process. Den Toonder et al. (2005) used an FE simulation to characterize SiLK polymer film. A linear viscoelastic response is considered. The nanoindentation creep responses from the FE analyses are comparable to the ones from the experimental tests for relatively low load levels. The mismatches are shown at relatively high loads due to the assumption of linear viscoelasticity. Anand and Ames (2006) proposed a viscoelastic-

plastic material model for amorphous polymers. They integrated their model into FEA to simulate load-displacement responses during indentation and compared their results with experimental results. This model is built by combining generalized Kelvin-Voigt models (i.e., used as a sub-module) in series or parallel. In order to get better accuracy, the model needs many sub-modules, and corresponding parameters for each sub-module must be calibrated by experiments. This model can generate accurate results. However, it cannot be efficiently used in characterize time-dependent material properties from the nanoindentation creep responses due to the large number of modeling parameters.

1.4 Nonlinear ANN Constitutive Models for Engineering Material Systems

Over the last decade, nonlinear ANN constitutive modeling approaches have been applied in engineering material systems to approximate complex behaviors (e.g., nonlinear multi-axial material behaviors including damage or creep responses). Pidaparti and Palakal (1993) were among the first to use ANN to predict the uni-directional material behaviors of angle-ply laminates. They used the tension test data to train their ANN, the input components of which include off-axis angle, initial stress, and incremental stress. Sankarasubramanian and Rajasekaran (1996) used ANN to characterize the yield surface of reinforced concrete structures. The output variables of their ANN model were distances from the origin to compressive and tensile yield surfaces, while the input variable was mean normal stress. Their ANN was trained with experimental data for concrete beams and panels. Sidarta and Ghaboussi (1998a, 1998b), and Fu et al. (2007) used ANNs to express stress-strain behaviors of geo-materials, such as soil and sand under tri-axial loading condition. Ghaboussi et al. (1998) proposed an ANN modeling method using an “auto-progressive training” to generate the nonlinear stress-strain behavior of anisotropic materials using limited experimental data measured at the structural level. They used adaptive neural networks and applied their approach to generate a constitutive model for laminated graphite/epoxy plates. Haj-Ali et al. (2001) proposed ANN

micromechanical models to generate damaged material behaviors of fiber reinforced materials. They considered interfacial cracks between the fiber and matrix for the damage and used FE simulations to train their ANNs. However, their models were limited to monotonic behavior and for a specific metal-matrix composite system. Al-Haik et al. (2004) used ANN to generate the time-displacement responses for a woven composite fabricated with a carbon fiber and polymeric matrix. The input variables of their model included normalized stress, temperature, and time as inputs, while the output was the corresponding strain. Their model can generate reasonable creep responses compared to the experimental results. However, the ANN model was limited to a specific creep loading. Jung and Ghaboussi (2006) also used ANN to generate creep behaviors for isotropic materials such as concrete. The output variables of their ANN were current stress components, while the input variables were previous stress-strain components and current strain components. They trained their ANN with FEA results and integrated the trained ANN into the FEA for a pre-stressed concrete beam. They examined their FE-ANN results by comparing with time-strain responses obtained from a gage attached at the mid-span of the pre-stressed concrete beam.

The ANN approach has also been used to predict failure states (e.g., length, location, and size of delamination) or design an optimum composition of composite materials. Okafor et al. (1996) used ANN to predict the delamination length in laminated composite beams. They trained their ANN models with normalized natural frequencies of damaged composite beams generated from FE simulations. The training results were compared with the corresponding test data. Ootao et al. (1999) applied a hierarchical neural network to optimize the material composition for a functionally graded material with respect to thermal stress distribution in a hollow circular cylinder. Zhang et al. (2002) used ANN to correlate the effect of temperature on the dynamic mechanical properties (storage modulus and damping) for short fiber carbon composites with two polymeric matrices, PTFE and PEEK. Chen et al. (2003) proposed a fuzzy neural network approach to approximate constitutive relations of SiCp/Ly12, an aluminum composite material. They used the Gaussian function to

categorize the inputs (i.e., temperature, strain rate, electric field, and true strain) into three fuzzy sets as small, medium, and large in their model. They then trained their fuzzy-NN model to produce the corresponding outputs (i.e., grain size, volume fraction, and true stress) using experimental data. Their ANN model showed appropriate results, but could generate a maximum 10% relative error with experimental results. Chakraborty (2005) proposed an ANN delamination model in order to predict the shape, size, and location of delaminations in laminated specimens with an elliptical embedded delamination. They used the ten natural frequencies of the specimen (i.e., from the first to the tenth mode) as the input variables of their ANN, while the outputs were different delamination geometry and location. They examined their ANN by comparing with FEA results that were not used in the training process.

1.5 Nonlinear ANN Constitutive Parameters and Models from Nanoindentation Tests

The ANN approach can be effectively used to extract material properties (e.g., elastic modulus, creep compliance, and other nonlinear material parameters) from available nanoindentation test results (e.g., load-displacement responses). The trained ANN can directly/indirectly extract the best combination of material parameters that generate the closest response to the given data. Muliana et al. (2002) proposed ANN models to generate nanoindentation load-displacement curves for copper material. They used only the monotonic part of the nanoindentation response and trained their ANN models. Their ANN models can generate nanoindentation force-depth curve for wide ranges of nonlinear material parameters. Their ANNs can be used to directly back-calculate the nonlinear stress-strain parameters from given nanoindentation responses. Similarly, Huber et al. (2002) used ANNs to extract stress-strain behaviors of films and substrates from indirect indentation responses. Their ANN models can generate nonlinear material parameters from the selected hardness and stiffness calculated from the experimental data. However, their models were less accurate when the properties of the film are close to the ones of the substrate. Tho et al. (2004) used two successive

ANNs to characterize elasto-plastic material properties from indentation tests. Their ANNs included the curvature of the indentation load-depth curve and the area below the loading and unloading parts as their input variables. Tyulyukovskiy and Huber (2006) used ANNs to characterize time-dependent material behaviors for visco-plastic (metallic) materials from nanoindentation creep responses. The input variables of their ANNs were unloading depth, stiffness to hardness ratio, and applied loads, while the output variables were elastic modulus, hardening material parameters, and coefficients of the power-law equation between strain and stress rates. Their ANNs trained with FEA results generated overall good prediction results. However, their ANNs produced inaccurate time-deflection responses compared to FEA results that were not used in the training.

1.6 Motivation and Scope of Present Study

The overall objective of this study is to formulate a new class of multi-scale nonlinear constitutive models for metallic and FRP composite material systems using ANNs. Towards that goal, various ANN models are proposed as constitutive models with full or limited mechanical responses characterizing different material systems, such as FRP composites and thin metallic films. These newly generated ANN models are efficient and accurate for a wide range of deformation and material variables. The previous literature reviews have provided some motivation for the use of the proposed ANN constitutive models over phenomenological and traditional nonlinear material models. This section adds to the motivation and presents an overall scope of the study. Next, the motivation for this study is presented through a review and a critique of the limitation of current ANN constitutive models.

ANN as anisotropic composite constitutive models

Pidarparti and Palakal (1993) were the first to propose an ANN model to generate uni-directional stress-strain responses for angle-ply laminates. They generated their ANN models from

experimental data obtained from off-axis tests. The data consisted of uni-axial stress-strain curves/points for different off-axis angles. However, the ANN models are limited because they do not provide a complete plane-stress constitutive model that can be used in a realistic structural analysis. Therefore, there is a need for a complete and full-range of nonlinear ANN material model that covers the entire nonlinear stress-strain spectrum, including the full multi-axial tensile-compressive-shear stress-strain space. In order to consider damage behavior of fiber reinforced materials, Haj-Ali et al. (2001) proposed the use of ANN to generate nonlinear micromechanical ANN models. They considered the interfacial crack between the fiber and matrix as their damage variable. The crack angle was used as a damage parameter in their unit cell (UC) models for a uni-directional metal-matrix composite. Their ANN models were trained to generate plane stress-strain constitutive models along with their damage variable using 3D FE simulation results. Their study was the first to show that ANN can be used to generate micromechanical material models with damage. However, their ANN was limited to monotonic behavior and for a specific system of Boron-Aluminum metal matrix composite material. Moreover, damage evolution (crack growth) was not considered. Therefore, there is a need to extend this approach to a wider range of composite materials and to allow different damage modes with evolution.

ANN as nonlinear nanoindentation models

Muliana et al. (2002) were among the first to use ANN to generate ANN nanoindentation models for homogeneous substrate with and without hard films. They used the monotonic part of FE simulated indentation load-deflection curves. Their trained ANN models were compared with FE simulations or experimental results that were not part of the training data. Their ANN models were effective in predicting the indentation response for a pre-specified range of nonlinear material parameters and elastic stiffness. However, the load, deflection, and material variables used in these ANN models were not very wide and non-dimensionalized, thus these ANN models were limited

within specified ranges. Therefore, ANN models are needed with a wider range of mechanical responses and material parameters using dimensionless variables.

Huber et al. (2002) was also among the first to use ANN in nanoindentaiton plastic behavior. They proposed four different dimensionless ANN models, two of which were to predict the hardness and stiffness for two different material systems: substrate-only and film-substrate systems. The other two ANN models were proposed to back-calculate material parameters, such as strain-hardening and yield stress, for the above two systems. Their models were trained with dimensionless terms combined with material parameters and indirect indentation responses, i.e. the hardness and stiffness of films and substrates that were determined in FE simulations at different indentation depths. They showed that their models can generate the hardness and the stiffness and is capable of "inverse" analyses to extract in-situ parameters of film on substrate material systems. However, this modeling approach exhibited relatively larger errors when the material behaviors of the film and the substrates are similar. Their ANN models include, in part, deduced hardness and stiffness variables derived from FE simulations or experiments. Therefore, there is no "full-memory" of the load-deflection curve of the direct indentation data once the ANNs are trained, i.e. one need to solve an in-direct system of equations to track back the indentation response from which the material behavior was generated.

ANN as time-dependent constitutive material models

Only few studies have proposed to characterize the time-dependent material behavior from nanoindentation creep tests of metallic systems. Tyulyukovskiy and Huber (2006) used ANNs trained from simulated FE results to characterize viscoplastic material parameters from nanoindentation creep for metallic materials. They proposed three separate classes of ANN models with outputs: elastic modulus, coefficients of the power-law relation between strain and stress rates, and hardening material parameters of metallic materials, respectively. Both the first and third ANN

models include unloading depth, stiffness to hardness ratio, and applied loads at different depths as their inputs, while the second ANN includes 32 dimensionless parameters generated from the load-depth data as its input variables. Their ANN models were trained with dimensionless input and output variables combined with material parameters and FE simulation results (i.e., hardness and stiffness) generated for a specific pre-defined creep loading history. Their ANN prediction results were compared with FE simulation results that were not used in the training. Their three models showed overall good agreements with FE results. However, big relative error that ranges from 13 to 80% in the output of the third ANN and significant mismatches (maximum of 30%) in time-deflection curves generated from the second ANN were also found. Their ANN indentation creep models were limited to viscoplastic behaviors of metallic materials. Currently, there are no ANN studies dealing with indentation creep behavior of polymeric materials. Therefore, similar and more general ANN models need to be generated to characterize the creep behavior of polymeric materials.

In the current study, a new class of multi-scale nonlinear ANNs constitutive models is formulated. Investigations have been carried out to generate ANN constitutive models for different nonlinear material systems. The ANNs modeling approach is applied to metallic, polymeric, and FRP composite materials with micro-structural variables at the macro, micro, and nano scales. The first investigation presents ANN as constitutive models to characterize nonlinear material and time-dependent parameters with micro- and nano-scale constituents from static and time-dependent nanoindentation test results. The second investigation deals with ANN as constitutive models for FRP composites with multi-axial stress-strain at the macro and micro scales including nonlinearity and damage. The proposed ANN constitutive models were trained with simulated FEA or experimental results. Macro-scale tests for FRP composites have also been carried out to train ANNs for FRP composites from experimental tests, such as off-axis tension/compression and pure shear (Arcan) tests for FRP composites. Numerical and experimental verifications are also performed to

demonstrate the capability of the proposed multi-scale nonlinear ANN constitutive models to predict material parameters and stress-strain behavior for cases that were not part of the ANN training.

This manuscript is divided into 7 chapters. Excluding this chapter, they are organized as follows: Chapter 2 describes the ideas behind ANNs, their structure, and mathematical formulation including training and error minimization of traditional ANNs used in this study. The developed ANN software code is also reviewed in this chapter. Several numerical examples are generated to investigate the developed ANN software for different ANN structures and training methods. Chapter 3 presents ANN constitutive models to characterize important nonlinear material parameters at the micro-scale from only the monotonic part of the nanoindentation load-displacement response. The proposed ANN models include dimensionless input/output variables generated with nonlinear material parameters and simulated FEA results for various material properties. Different ANN models with different input and output variables are generated and trained to examine the effectiveness and the quality of the proposed ANN models. The later part of Chapter 3 includes experimental verifications and using ANN in "inverse" mechanical identification problems. Toward that goal, the trained dimensionless ANN models are used to generate in-situ nonlinear stress-strain responses from nanoindentation tests results performed on a silicon (Si) substrate with and without a nanocrystalline copper (Cu) film. The extracted in-situ material responses are compared to the existing experimental data from Bansal et al. (2004) and the prediction results are discussed.

In Chapter 4, artificial neural networks (ANNs) are used as time-dependent and creep models for polymeric materials. The proposed ANN models are generated to characterize in-situ time-dependent material parameters from nanoindentation creep responses (i.e., time-displacement behaviors). In order to fully characterize the creep behavior of polymeric materials, three different ANNs were generated with three different sets of input variables: applied load and logarithmic time; elastic modulus, Poisson's ratio, and logarithmic time; and elastic modulus, creep compliance

coefficients, and logarithmic time, respectively. On the other hand, their output is the same in the form of indentation displacement. The proposed three ANN models are complementary and were trained with the same simulated FE results and examined with simulated FEA results that were not used in the training. The third ANN model is practical and is used in an inverse problem to extract the in-situ viscoelastic compliance parameters and elastic modulus from creep experimental data performed on Polycarbonate coupons. The predicted creep compliance compares favorably with available data obtained from the literature.

In Chapter 5, different ANNs are used as plane-stress anisotropic constitutive models for FRP composites. The ANN constitutive models are used to relate the multi-axial plane-strain output variables to a given plane-stress input vector. Two types of ANNs were constructed. The first has the total strain as output while the second has only the inelastic part of the strain components. The ANNs are not trained with simulated FE models. Instead, they are trained with experimental data obtained from off-axis tension/compression test and pure shear (Arcan) tests conducted as part of this study. These experimental tests are limited and cannot produce complete multi-axial stress-strain paths for unidirectional coupons, such as tension-compression and compression-tension. Since the axial response is much stiffer than the transverse response, it is assumed that a tension-tension (axial-transverse) mode is symmetric to a compression-tension mode, and vice versa. The trained FRP nonlinear ANN constitutive model is integrated with an FEA for the general nonlinear analysis of composite structures. A notched composite plate is simulated to generate the spatially heterogeneous response sampled at each integration point of the FE mesh. The simulated FE-ANN structural results are compared with experimental results performed in this study for the thick-section FRP E-glass/Polyester plate.

Chapter 6 presents micromechanical ANN constitutive models to generate nonlinear effective stress-strain responses for unidirectional fiber reinforced composite materials with damage

formulation. These micromechanical ANN models include void damage within the matrix. Cylindrical void with different diameters was used in the FE simulations for the ANN training. Damage variable, fiber volume fraction (FVF), and elastic material properties were used as ANN inputs to predict effective stress responses. These ANN models can be used to simulate damage dissipation for a given load history. This ANN modeling approach and methodology to predict nonlinear and damage responses is addressed and discussed in Chapter 6. Finally, the summary of the study and future recommendations are presented in Chapter 7.

CHAPTER 2: Artificial Neural Networks

For several decades, artificial neural networks (ANNs) have been widely used in the various applications of engineering fields, e.g., prediction of undiscovered terrain from existing data, recognition of letters or words from handwriting, or prediction of near future weather. Applicable commercial fields of ANNs, such as letter recognition, monitor processing, and risk analysis systems, were studied and reported earlier in the DARPA (1988) Neural Network Study. In addition to commercial fields, ANNs has been efficiently applied in many fields (e.g., medical, economics, and engineering) especially as computer hardware has been advanced. Sophisticated ANN implementation (Toolbox) have been available in the MATLAB (2005) well-known mathematical software in the section "Neural Network Toolbox" with suggested applications in aerospace, automotive, banking, credit card and financial activity, defense, electronics, entertainment, industrial, insurance, manufacturing, medical, oil and gas, robotics, speech, securities, telecommunications, and transportation.

2.1 Artificial Neurons and Network Architectures

In general, computational and artificial neural networks (ANNs) are a field of science aimed at mimicking natural "learning" using mathematically based approximation. A single biological neuron is composed of three major parts: the cell body, the axon, and the dendrite. Figure 2.1 shows the schematic drawing of representative biological neurons and a simplified computational neuron. The head (i.e., the cell body) of a neuron is connected to the tail (i.e., the dendrite) of a neighboring neuron. These individual biological neurons are interconnected with the other neurons through hair-like dendrites. A group of these neurons can consist of layers of neurons, and a collection of layers can form nerve systems in the human body, e.g., brain tissue. Stimulus or signal communications

between neurons are continuously generated; it is delivered from one neuron to the others by firing an electrical signal generated through a chemical reaction. The other neurons receive the signal through the interfaces with the neighboring neurons, referred to as a synapse. This system is capable of learning, recalling, and generating output corresponding to external signals. If a system of neurons has a consistent and frequent external signal, its output signal will be consistent and thus memorized or stored in the system. On the other hand, if it is subjected to an insistent or rare signal, the memory for this type of information may vanish after receiving other signals or patterns. This biological neuron system can work collectively to handle more complicated learning to illustrate how the mathematical operations are used to mimic the major biological functionalities. The general computational neuron is shown in Figure 2.1b. Similar to biological neurons, a computational neuron has input, a neuron cell, and output. Each neuron is commonly connected with net-like internal weights in which complex behaviors or knowledge is embedded. The ANN classes can be distinguished by overall structure, neuron type, training data space, and learning rules among others.

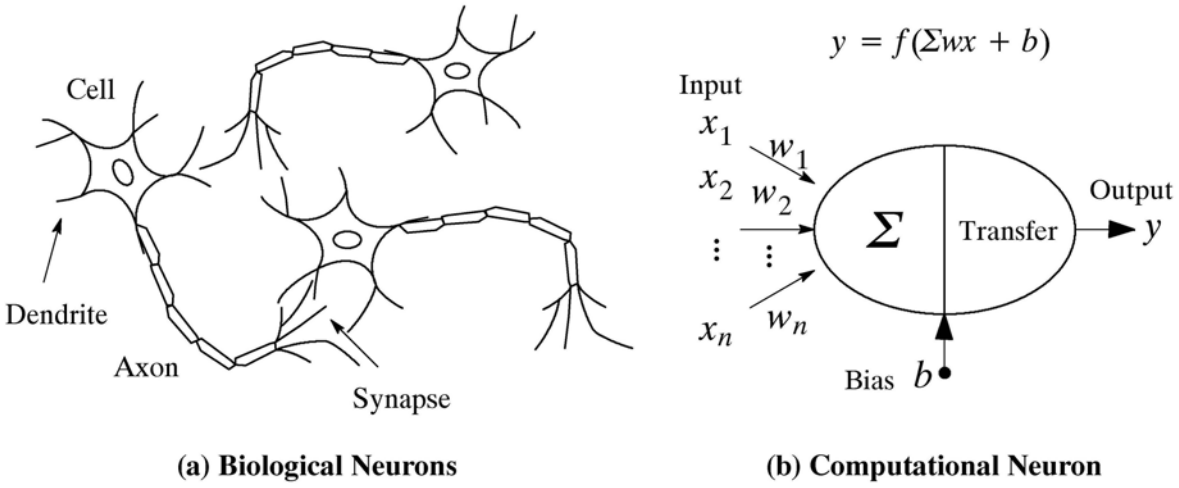

Figure 2.1 Schematic drawing of (a) biological neurons and (b) computational neuron. (Adapted from Lin and Lee, 1996)

Single Artificial Neurons with Scalar and Vector Inputs

Input variables of artificial neurons can be scalar or vector types with and without bias. In the single neuron without bias, the scalar input (x) is transmitted through the artificial neuron and multiplied by its neuron weight (w). The summed augment (wx) is then fired, and its output (y) is generated through the activation (transfer) function, expressed as $y = f(wx)$. In similar way, the single neuron with bias can be represented as $y = f(wx + b)$. The weight (w) and bias (b) can be adjusted in order to get accurate output. The main idea of building a collection of ANNs is to store and recall various behaviors embedded in the data by adjusting neuron weights during a repeated training process. More complex nonlinear integration functions can be used instead of a linear relationship such as quadratic function: $y = f(wx^2 + b)$ and spherical function: $y = c \times f(w - x)^2 + b$. However, the first homogeneously scaled input is more common in ANN models. Similar to the single-variable input neuron, artificial neurons with vector input components (i.e., x_i, $i = 1, 2, \cdots, n$) are formed by multiplying their weights (i.e., w_i, $i = 1, 2, \cdots, n$) to each input component, and only the summation (i.e., $\sum wx$) is transferred through the activation or transfer function. The neuron with the scalar input can be seen as a special case of the vector-input neuron. The structure of ANN without bias can be expressed as $y = f(\sum wx)$. Here, n is the number of input variables. The ANN with bias can be also represented as $y = f(\sum wx + b)$ as shown in Figure 2.1b.

Multi-Layered Assembly of Neural Networks

A group of artificial neurons can be collected and commonly referred to as a neural network (ANN). The artificial neural networks can be different numbers of layers with variable neurons in their layers. The structure of ANN is often determined by the characteristic of the input data and

behavior that needs to be approximated. In general, a single-layered ANN has been found suitable for simple patterns or behaviors, while multi-layered ANNs are used to approximate more complex nonlinear behaviors, e.g., Wasserman (1989) and Lin and Lee (1996). Multi-layered neural networks (NNs) are more powerful than the single-layered NN due to their nested and adjustable capability of internal signal mapping which can overcome signal complexity, such as non-smooth data with discontinuity or noise. For the latter, the nonlinear input data is processed by the ANN using different activation or transfer functions, e.g., sigmoid and linear functions for the first, second, and following hidden layers, respectively. In addition, the number or structure of the neurons can be adjusted to exhibit complex behaviors. Multi-layered NNs is more extensively used in many engineering applications than single-layered NNs. Figure 2.2 shows the schematic drawing of the general multi-layered NN. It has one general input, one output, and n hidden layers, respectively. Each layer can have a different number of neurons and activation functions such as sigmoid and linear functions. All neurons are interconnected to the neighbor neurons (i.e., neurons in the next layer) through their weights ($w_{mi}^{[n]}$). Here, n denotes the specific hidden layer; m is neuron number of layer$[n-1]$ while i denotes the neuron number of hidden layer$[n]$. In addition, bias vectors, $b_i^{[n]}$ can be added to each layer. All layers can be generally expressed using a vector function: $f^{[n]}(w^{[n]}x'^{(n-1)}+b^{[n]})$. Here $x^{[n-1]}$ is the input passed through the $[n-1]$ layer. As a result, the output of ANN without biases, with n layers can be expressed as nested vector transformations:

$$y = f^{[n]}(w^{[n]}x^{[n-1]}) = f^{[n]}(w^{[n]}\ f^{[n-1]}(w^{[n-1]}x^{[n-2]}))$$
$$= f^{[n]}(w^{[n]}f^{[n-1]}\ (w^{[n-1]}f^{[n-2]}\ (\cdots f^{[1]}(w^{[1]}x^{[1]})\cdots))) \quad (2.1)$$

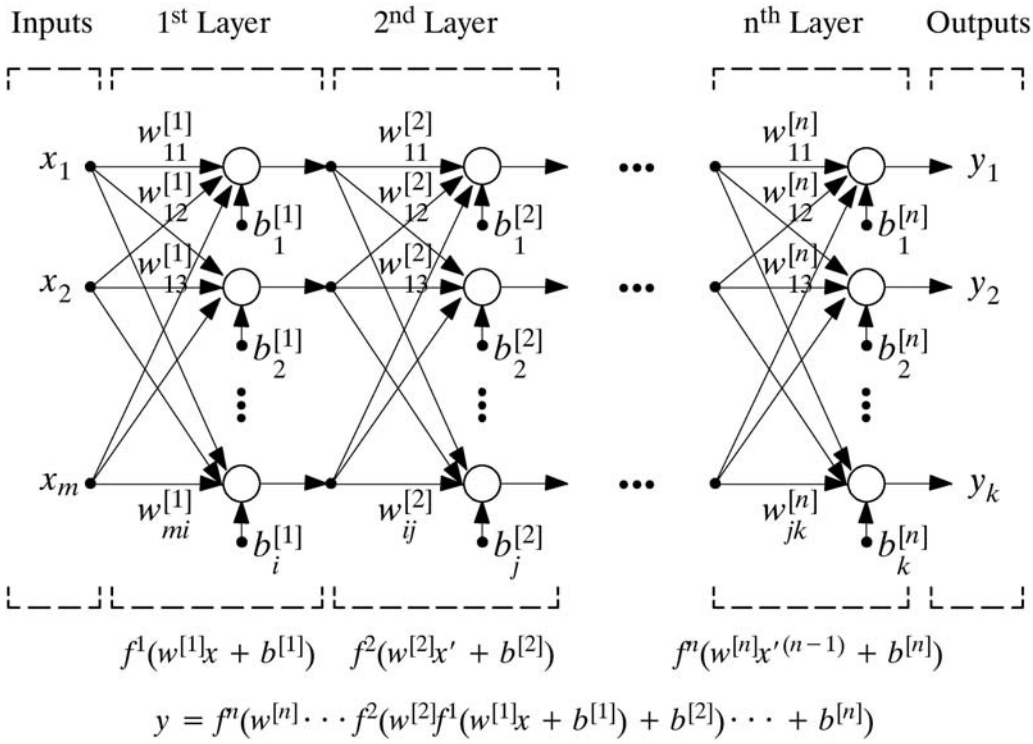

Figure 2.2 Schematic drawing of a feed-forward multi-layered Artificial Neural Networks (ANNs). (Adapted from Demuth et al., 2005)

Activation (Transfer) Function and Learning Rule

In order to acquire a stable, robust output from an ANN within a specific input-output span, an activation or transfer function is used. The integrated argument (i.e., accumulated multiplication of inputs and weights) is further processed through this activation or transfer function. The base function can be suited and selected according to the training data set. However, it is not possible to find a unique base of function in the general case. Figure 2.3 presents examples of common activation functions: (a) Step function; (b) hard limiter function; (c) ramp function; (d) unipolar sigmoid function; and (e) bipolar sigmoid function. The step and hard limiter functions are commonly used to make a classification decision. The ramp function has a linear relationship within a range of the input generating a continuous linear output from 0 to 1. The function produces either 0 or 1 for the other input ranges. This function is much more suitable for linear approximations.

Unipolar or bipolar sigmoid functions are commonly used when complex relations are required. Smoothness of the nonlinear functions can be adjusted by a parameter (λ).

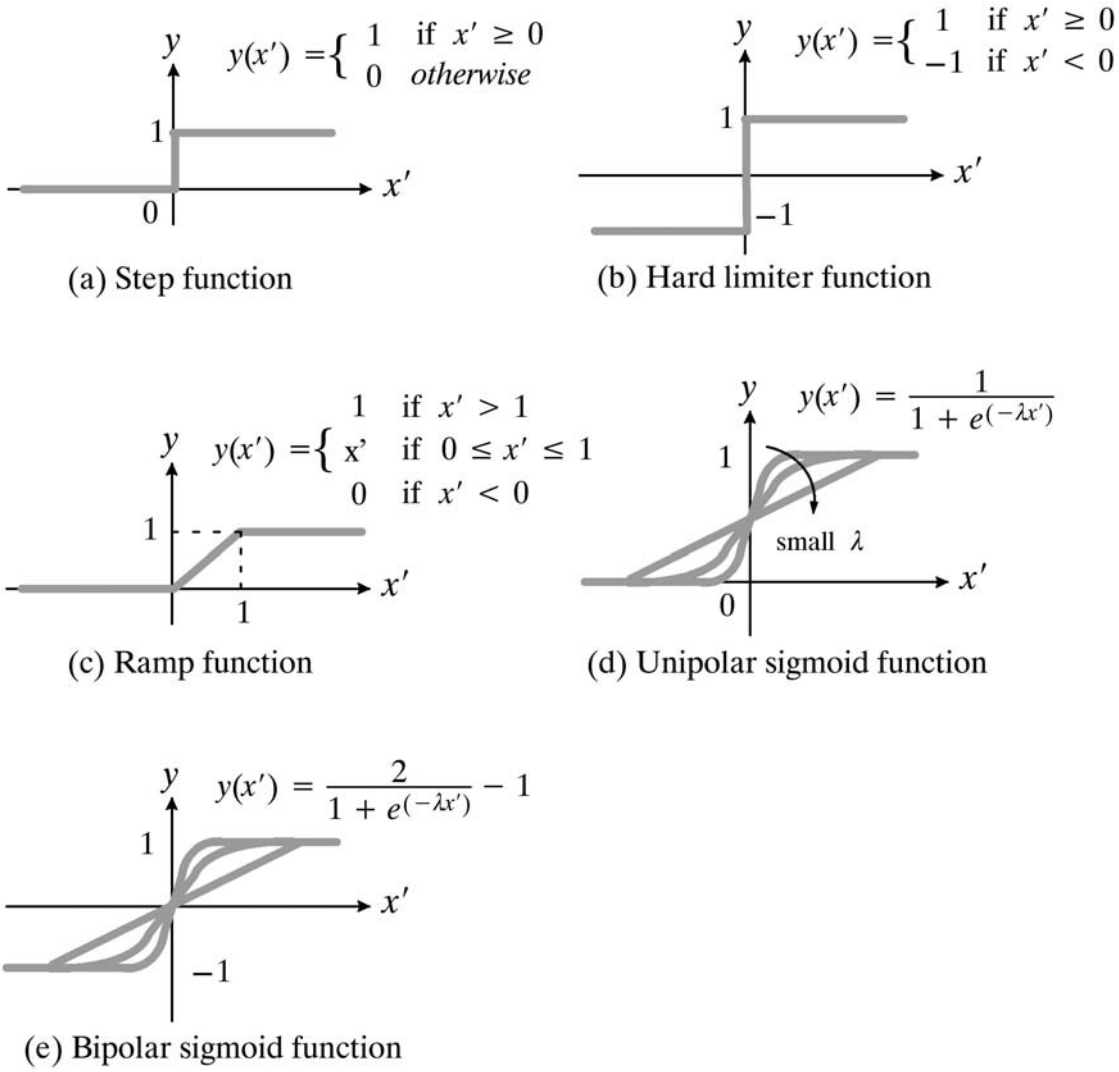

Figure 2.3 Examples of activation (transfer) functions. (Adapted from Lin and Lee, 1996)

The weights of the ANN are determined by the training (learning) process. Training can be achieved with a static or dynamic ANN structure. The former ANN includes adjusting the weight matrix while fixing the number of hidden layers and their number of neurons. The latter ANN structure evolves, and neurons are added to the hidden layers during the training. It is known that the

latter method can be effectively used to approximate more complicated relations where many local optimum points can exist by Ghaboussi and Sidarta (1998). This adjustable training can be divided into several stages with different learning rules such as supervised and unsupervised learning. Figure 2.4 shows the schematic drawings of these methods. Supervised learning requires a pair of training data, i.e., input and target data couple, as shown in Figure 2.4a. The provided output is referred to as target data. In this learning process, internal connections such as neuron weights and bias are adjusted based on the result of the comparison between target and output values in order for the ANN to generate characteristics close to the target behavior. This method is known as effective and commonly used as a learning (training) method. However, it has been argued that this type of learning algorithm is not close to the learning of biological neurons. In the supervised learning method, artificial neurons cannot be trained without a target value. However, biological neurons can be adjusted without this comparison with a target value, e.g., learning how to walk. Because of this requirement, unsupervised learning has been introduced. In contrast to the supervised learning, unsupervised learning requires only input data as training data, as shown in Figure 2.4b. This process uses the previously generated output data as new input data, and modifies the neuron weights until the ANN produces consistent output. When there is no comparison, this learning process can be used to arrange school classes or class hours.

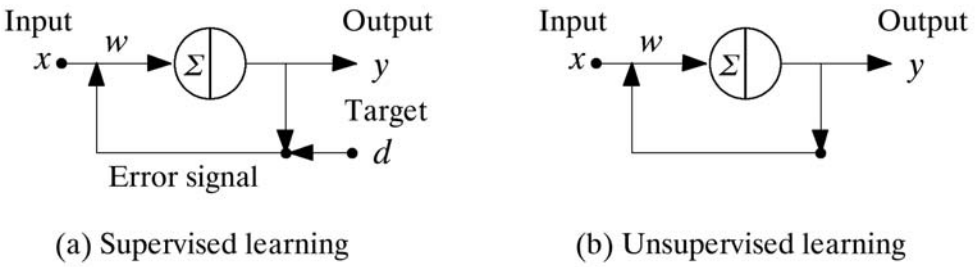

Figure 2.4 Schematic drawings of neurons used in supervised and unsupervised learning. (Adapted from Demuth et al., 2005)

ANN Structure and Neuron Connections

The capability of ANN to approximate complex data patterns is influenced by the neuron and its connection type. There are two neuron-connection types commonly used. One is feed-forward type, and the other is feed-backward. The feed-forward type NN literally forwards the integrated augment as its output never used as a part of input. However, the feed-backward type NN produces the integrated augment as output, and the output is also used as a part of new input. These connections are pre-determined by user for the required capability of ANNs. Various ANN models can be created by using different connections among neurons for their purposes. Figure 2.5 shows typical examples of neural network connections: (a) a feed-forward, single-layer neural network; (b) a feed-forward, multi-layer neural network; (c) a feed-backward, single neuron; and (d) a feed-backward, single-layer neural network.

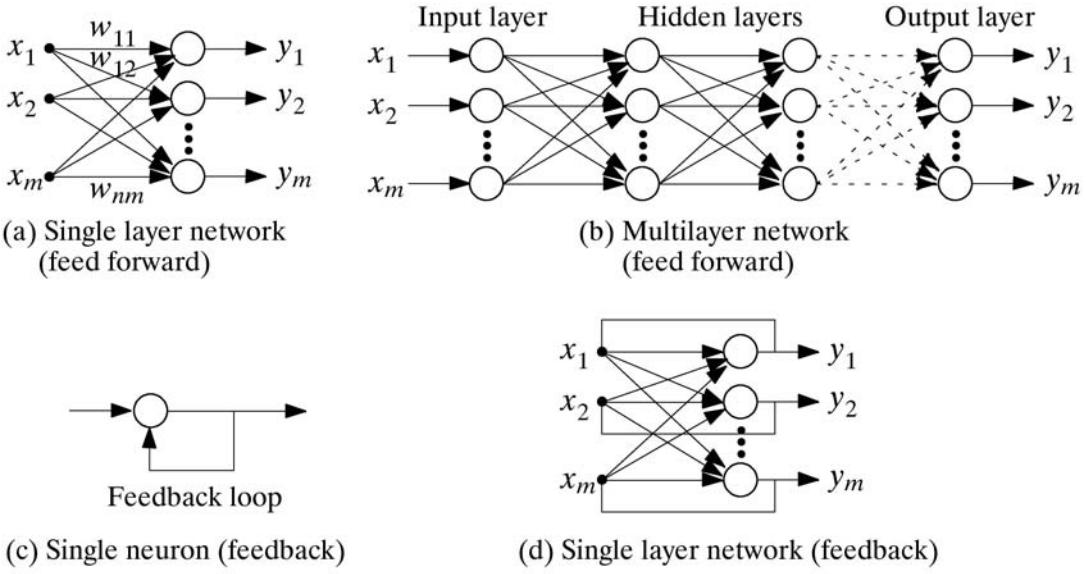

Figure 2.5 Example of feed-forward and feed-backward neural networks. (Adapted from Lin and Lee, 1996)

2.2 Proposed Artificial Neural Networks (ANNs) for Nonlinear Material Behavior

In the past decade, ANNs have been used to generate complex nonlinear material behaviors (e.g., plasticity, creep, and relaxation) or predict structural responses (e.g., delamination in FRP composite) due to their effectiveness in those problems. Many researchers have developed their ANN models by varying ANN structures (e.g., number of neurons, hidden layers, and input-output variables) suited for their engineering problems. In material modeling, a typical ANN structure has been commonly used in the form of one input layer, one or two hidden layers, and one output layer. Once the ANN structure is determined, the capability of the ANN constitutive models becomes mainly dependent on the quality and quantity of connection weights. In general, ANN models with larger number of neurons are capable of approximating more complex behaviors than the ones with the less number of neurons. However, in the case of using too large number of neurons, the trained ANN will be biased to the pattern of data used in the training and less capable in interpolating.

In this study, an in-house ANN code is developed using the FOTRAN language. The common structure of the ANNs composed of one input, feed-forward type two hidden layers, and one output layer is considered in the ANN code. This program includes a sigmoid function and three supervised learning rules as an activation function and learning rules, respectively. In addition, the generated ANNs can be trained with the adaptive training method in this program. For ANNs in engineering mechanics, the adaptive ANN has been used by several researchers (e.g., Gaboussi et al., 1998 and Haj-Ali et al., 2001). The advantage of this adaptive training method can effectively generate appropriate ANN models by changing ANN structures during the training process. If the ANN cannot generate appropriate values within the given training iteration number and training criteria, the ANN increases the capability of the ANNs by adding more neurons. Figure 2.6 describes its schematic flow. This can be explained by the following 6 steps. In the first step, all connection weights among the selected input and output variables are specified by users. If there are no

preferable or prior weights, random numbers between zero and one are provided as initial weights. In second step, all input-output training data is scaled within the ranges of the input/output variables of the selected activation function. From the third step, the ANN training starts to generate appropriate ANN models. The training continues to update and adjust ANN weights until the ANN can produce satisfactory outputs compared to target values. Its decision is made based on the comparison result between total error and given error tolerance. In this program, total error function is defined as the summation of all discrepancies between ANN outputs and target values (i.e., given as training output data). In the forth step, an if-statement is used to avoid the divergence of training. The program automatically stops the training, if the training iteration number is greater than maximum iteration number given by users. If the calculated error is greater than the tolerance and the iteration number less than given maximum number, the ANN goes to the fifth step, i.e., adaptive ANN training. Detail of this step can be explained by the following three sub-steps: 1) Increase new neurons in each middle layer; 2) adjust newly-added weights after freezing the weights previously adjusted; 3) adjust all weights after releasing the newly-added weights. Steps 3 through 5 are continued until the ANN produces satisfactory outputs.

1. Initialize all values and variables (e.g., using random values for initial weights)

2. Scale the training data set within the range of input and output values of activation functions
   (e.g., Input and output ranges of a typical unipolar sigmoid function are -1~1 and 0~1, respectively)

3. Start training (Adjust weight values to minimize the total error function)

$$Total\ error = \frac{1}{2}\Sigma\Sigma\|T_i - O_i\|$$

4. If the total error is less than the given tolerance
   or the training iteration number is greater than the maximum number, then GOTO 6

$$Training\ iteration \geq Iteration\ tolerance \quad or \quad Total\ error \leq Tolerance$$

5. If the total error is NOT less than the given tolerance,
   then ADD a new neuron in each middle layer in the following way:

   - Freeze the previous weights connected among the existing neurons,
     and adjust the weights linked to the newly-added neuron
   - Unfreeze all weights and GOTO 3

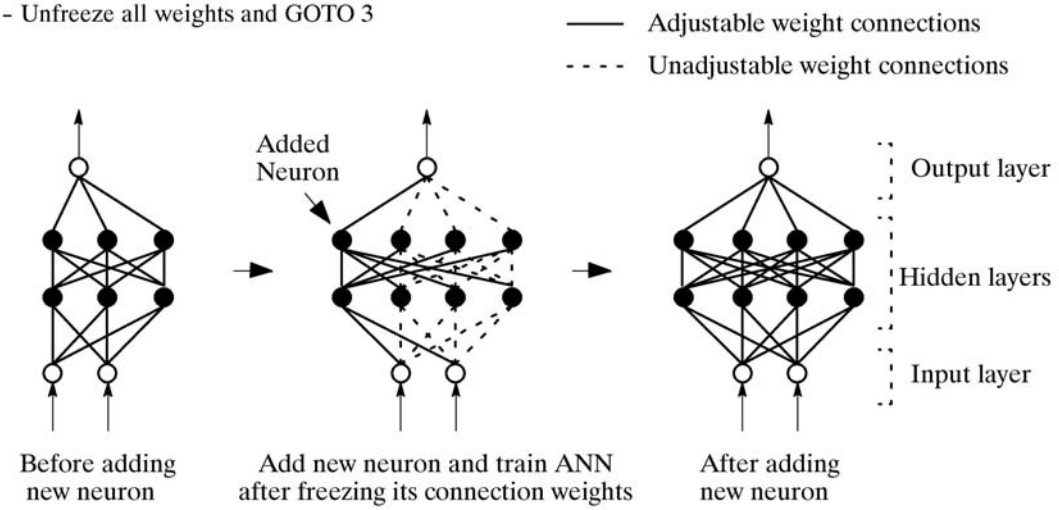

6. Stop training and generate ANN models

Figure 2.6 Schematic flow of the ANN code developed in this study

The ANN code developed in this study includes three different supervised learning rules, i.e., the steepest gradient descent method (SGM), the momentum method, and the conjugate gradient descent method (CGM). These are gradient-based methods commonly used to train ANNs. In order to calculate the gradients, total error function is also commonly used to as a basic relation. Figure 2.7 shows the schematic drawing of the three (back-propagation) learning rules. First, the steepest gradient descent method (SGM) uses the steepest gradient of the total error function with respect to the weights. This method updates the previous weight by adding the current weight increment calculated by multiplying a learning rate and the current steepest gradient. This method can quickly converge into an optimum point through training iterations. However, this method may require more iterations as the ANN output approaches closer to target values because current weights are updated based on the current steepest gradients.

The second is the moment method shown in Figure 2.7b. The moment method uses an additional term, referred to as a moment coefficient (α). This method can partially remember the previous training history by using the moment coefficient. This coefficient can be greater or equal to zero, but usually less than one. If a large coefficient value is used, the weight can be slowly converged because the weights are updated based on the previous gradients. On the other hand, a small coefficient can minimize the influence of the previous gradients. Therefore, this algorithm needs a parameter study to determine the appropriate moment coefficient value.

The third is the conjugate gradient descent method (CGM) that uses a conjugated gradient function to update ANN weights instead of using the steepest gradient function. The conjugate gradient function is formulated by adding the current weight increment calculated by SGM to the current conjugate gradient increment. The current conjugate gradient increment is calculated by multiplying the previous conjugate gradient to the relative magnitude between the current and

previous steepest gradients. This method needs more than two pairs of training data because of the relative magnitude calculated from the current and previous steepest gradients. This method is known as more efficient and effective than SGM to generate appropriate ANNs.

1. Use the gradient of the total error function, E(w), with respect to connection weights:

$$E = \frac{1}{2}\Sigma\Sigma\|T_i - O_i\|, \quad \Delta w = -\eta\frac{\partial E}{\partial w}$$

2. Update connection weights by adding the adjusted weight increment(Δw):

(a) Steepest gradient descent method (SGM)

1. Consider the additional term that partially remembers the previous training history. The corresponding weight increment can be formulated as follows:

$$\Delta w_i = -\eta\frac{\partial E}{\partial w_i} + \alpha\Delta w_{(i-1)}$$

Here, i: current training data set; i-1: previoue training data set; α: momentum coefficient $(0 \le \alpha < 1)$

(b) Momentum method

1. Use the steepest gradient as the first conjugate gradient descent (p_0):

$$p_0 = -g_0 = -\eta\frac{\partial E}{\partial w}$$

2. Calculate the current conjugate gradient(P_i) by adding the current weight increment calculated by SGM to the current conjugate gradient increment(p_{i-1}). Here, the current conjugate gradient increment can be calculated by multiplying the previous conjugate gradient(p_{i-1}) and its relative magnitude(β_i):

$$P_i = -\eta\frac{\partial E}{\partial w_i} + \Delta p_i \;; \quad \Delta p_i = \beta_i\, p_{i-1}$$

3. Update the previous weights by adding the current conjugate gradient.

$$w_i = w_{(i-1)} + P_i \qquad \beta_i = \frac{g_i^T\, g_i}{g_{i-1}^T\, g_{i-1}}$$

(c) Conjugate gradient descent method (CGM)

Figure 2.7 supervised learning rule (back propagation)

2.3 Numerical Examples

In order to investigate the developed ANN code, two numerical examples have been performed. The first is to examine the ANNs trained with the three different supervised learning rules. The second is to investigate ANNs trained with and without using the adaptive training method. Their training and prediction results are compared with each other for each example. In these two examples, two separate training data sets are used. One set is unipolar sigmoid function values, and the other set is the structural load-deflection responses of a truss structure.

In the first example, three sets of ANNs for three different back propagation rules (i.e., SGM, momentum method with the coefficient of 0.6, and CGM in Figure 2.7) were respectively generated to approximate the unipolar sigmoid function response. One individual ANN was generated for each ANN set of SGM and CGM, respectively. On the other hand, nine ANNs with different moment coefficients (i.e., from 0.1 to 0.9) were generated for the ANN set of the moment method to examine the influence of the moment coefficient on the prediction results. All ANNs were trained under the total error tolerance of 0.01% and fixed neuron number of 3 during the training. A total of 33 training data pairs were used. Their input and output was ranged from -5 to 5 and from 0 to 1, respectively. Figure 2.8a represents the original training data and ANN prediction results trained with three different learning rules. The trained ANNs can generate overall accurate sigmoid function responses compared to the training data. The maximum differences with the training data were less than 3.6% in SGM and 1% in both momentum method and CGM at their maximum or minimum input ranges. This may be caused by different sensitivity of the ANN trained with different learning rules. As a matter of the effectiveness of learning rules, training iteration numbers for the three different learning rules were compared. The training iteration numbers were 335 and 180 for CGM and momentum method, respectively. These values were relatively small compared to the one for SGM, i.e., 456. It

is interesting that the momentum method with the coefficient of 0.6 produced the smallest training iteration number.

The ANNs trained with different moment coefficients were also examined. They were trained under the same training condition (i.e., the total error tolerance of 0.01% and the fixed neuron number of 3). Their ANN prediction results were also the same as the one with the moment coefficient of 0.6 described in Figure 2.8a. However, the iteration number required to complete the training of the ANNs with different coefficients was different. Figure 2.8b shows the training iteration number required for the training of the ANNs with different moment coefficients. This figure describes that the coefficient of 0.6 was the most appropriate value to efficiently complete the ANN training among other moment coefficients used in this training. On the other hand, the coefficient of 0.9 generated the maximum iteration number (i.e., 24,461) among other cases. The momentum method seems to be totally dependent on the moment coefficient value and not to have a specific trend in this numerical investigation. It cannot be determined which moment coefficient value is appropriate for efficient training of ANNs without performing a parameter study. As a result, the robust and efficient CGM is used as a back propagation learning rule of the ANNs proposed in this study.

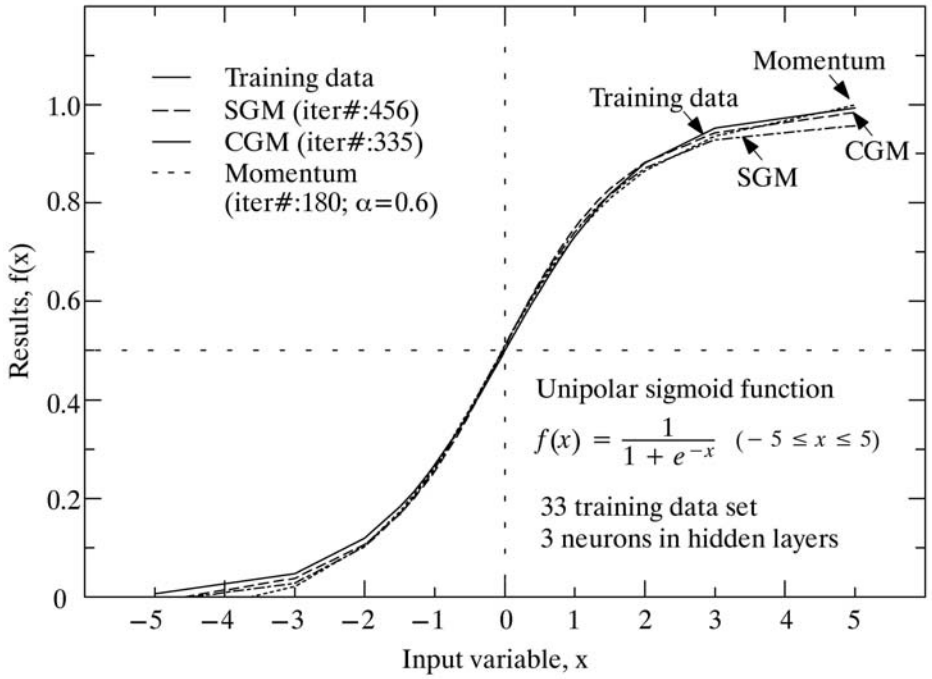

(a) Training data and ANN prediction results for three different learning rules

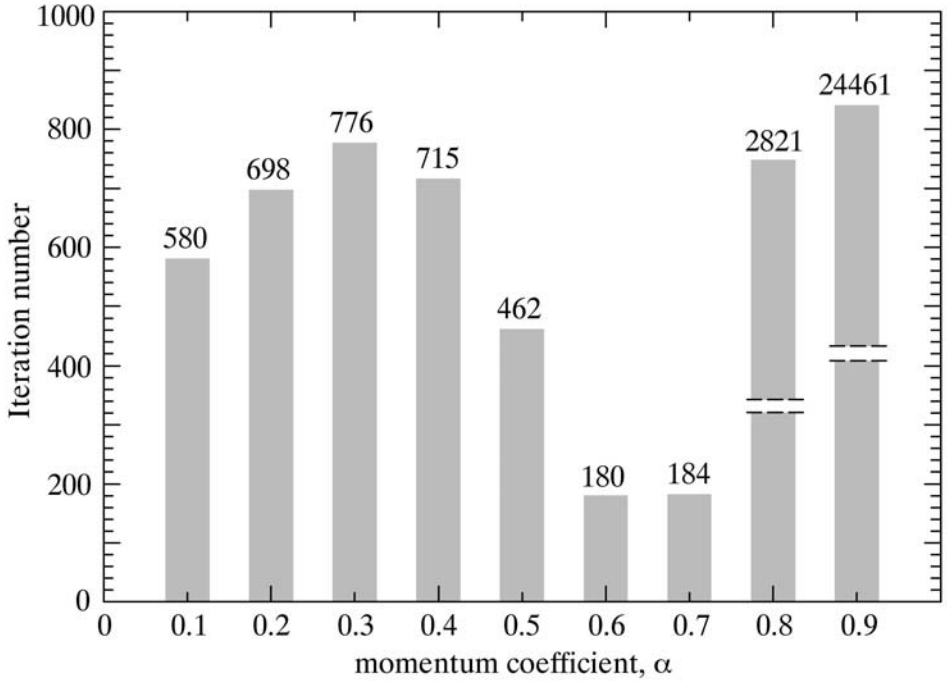

(b) Iteration number required to complete the training of ANNs with different moment coefficients, α

Figure 2.8 ANN training examples; (a) ANN training results for three different learning rules, i.e., the steepest gradient descent method (SGM), the momentum method, and the conjugate gradient method (CGM); (b) Iteration number required to complete the training of ANNs with different momentum coefficients, α

The second numerical example is for investigating ANNs with static and dynamic structure during the training process. Towards that goal, three investigations have been performed. Firstly, ANNs with different number of neurons are generated and trained without changing their neuron numbers during their training. Their prediction results (i.e., load-displacement responses) and iteration numbers required to complete their training are compared with each other. Secondly, the predictions of ANNs, trained under the same number of neurons but different error tolerance, are examined. Thirdly, another ANN is generated and allowed to increase its neuron numbers using the adaptive training method. Its prediction result is also compared with the training data.

In this examination, a simple truss example structure (Ghaboussi et al., 1998) was used. Figure 2.9a shows the truss structure and its geometry information. The truss is 1 bay and 5 story structure with diagonal bracing members through all the stories. In order to generate the structural response (i.e., force-displacement response), a lateral force (P) is applied at the connection joint of horizontal and vertical truss members of each floor. Both the horizontal and vertical truss members are 10 feet long. The cross sectional area of the vertical truss members is $12\,in^2$, while that of horizontal and bracing members is $4\,in^2$. In this numerical example, one-dimensional (1D) nonlinear material behavior is considered using the Ramberg-Osgood material model as follows:

$$\varepsilon = \frac{\sigma}{E} + \frac{2\beta\sigma_0}{3E}\left(\frac{\sigma}{\sigma_0}\right)^n \tag{2.2}$$

Material parameters and the lateral force used in the simulation are as follows: $E = 8.69\times10^3\ ksi\ (59.9GPa)$; $\beta = 1.25$; $\sigma_0 = 10.39\,ksi\ (71.6MPa)$; $n = 5$; and $P = 30kip\,(133.44kN)$.

Nonlinear material behavior is simulated using UMAT subroutine in the ABAQUS standard FE code. Figure 2.9b shows the simulated FEA result, i.e., applied lateral force (P) versus the corresponding displacement (U) at the right column of the fifth story of the truss structure.

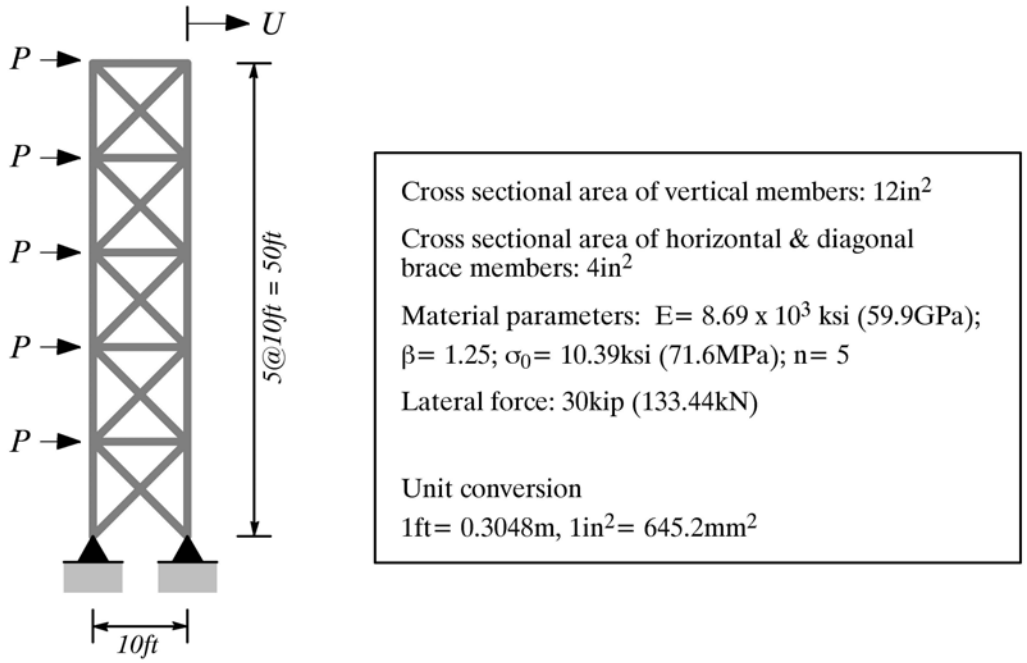

(a) Geometry & material information of the example truss structure

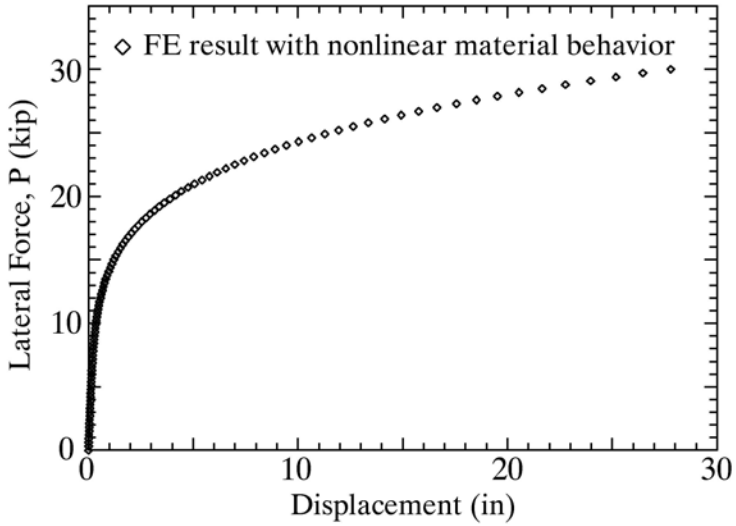

(b) Structural response (i.e., force−displacement data) generated from FEA

Figure 2.9 Example truss structure and the FEA result: (a) Geometry & material information of the example truss structure; and (b) structural response (i.e., force-displacement data) generated from FEA

As a training data set, fifty data pairs were collected from the generated load-displacement responses. One ANN with 3 neurons in the hidden layers was used for the preliminary test of the ANN to generate this response. The ANN includes one input (P) and one output (U). It was trained with large total error tolerance (i.e., 0.1). This large tolerance value was intentionally used to complete the training of ANNs with a small number of neurons. Otherwise, some ANN with a small number of neurons may not be completely trained. The training was completed with 17,388 iterations within the given error tolerance. Figure 2.10 shows the load-displacement responses generated from the training data and the trained ANN with 3 neurons. The training data (i.e., simulated FEA result) is described as a diamond symbol, while the ANN prediction is represented as a solid line. The trained ANN can generate an overall force-displacement response, but its result is oscillated because of the large value of error tolerance. Discrepancies between the training data and the prediction result can be eliminated by using smaller error tolerance or/and more neurons. This will be shown in the second investigation.

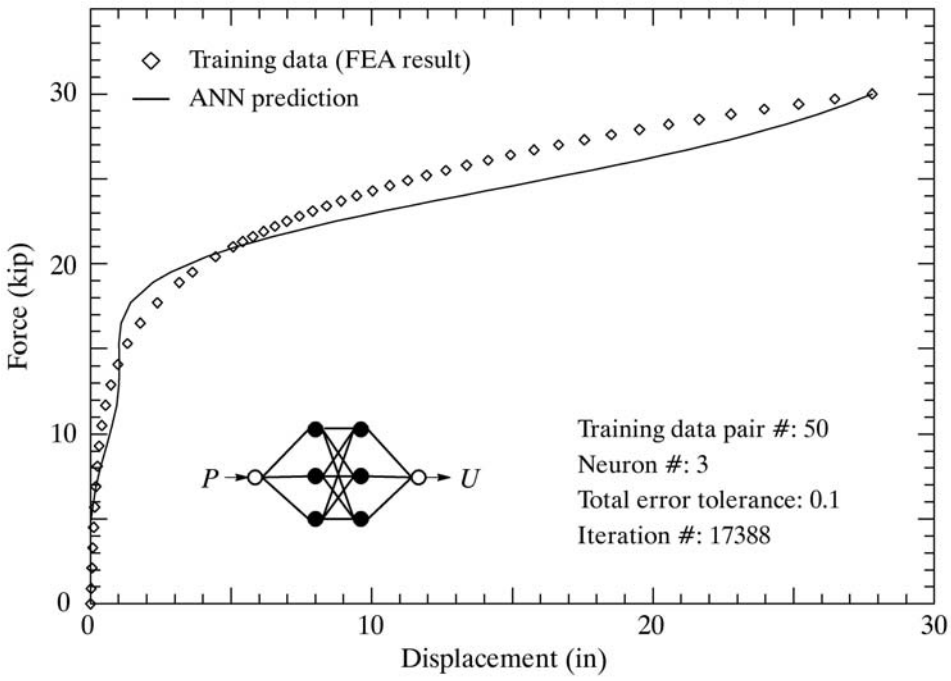

Figure 2.10 FEA and ANN results including 3 neurons in its hidden layers

In the first investigation, fifteen ANNs with different neuron numbers from 1 to 15 were generated to examine the influence of the neuron number on the prediction results. The ANNs were trained under the same error tolerance (i.e., 0.1) as previous one and with the fixed number of neurons. Their training results (i.e., force-displacement responses) were the same as one shown in Figure 2.10. However, iteration numbers required to complete the training of each ANN were different. Figure 2.11 shows the relation between the training iteration and neuron numbers of each ANN. For the purpose of explanation, the relation was divided into three regions (i.e., 1~5, 5~10, and 10~15) according to the neuron numbers used in the ANNs. In the first region, the ANN including 1 neuron was not completely trained for many training iterations, more than 100,000. Except for this case, the other ANNs in region 1 were completely trained with relatively higher iteration numbers (i.e., greater than 10,000). In addition, the relation between the training iteration and neuron number was oscillated. This may be caused by the different initial weights randomly specified. The ANNs in region 1 seems to be insufficient to generate the given structural behavior with their neurons. On the contrary, the ANNs in the second region were trained with relatively small iteration numbers (less than 5,000). The training iteration number decreased as the neuron number increased. Little increasing or decreasing in the training iteration number was found in the third region. This result showed that the ANNs were stably trained with the given number of neurons. The iteration numbers in this region may be the appropriate neuron number for training ANNs with the given error tolerance and training data. As a result, a parameter study needs to be performed to determine the appropriate neuron numbers for ANNs including fixed number of neurons in the training because it plays an important role for its efficiency and capability. The training iteration number generated in this investigation is also summarized in Table 2.1.

Table 2.1 Training iterations needed for each ANN size

ANN size (neuron s)	Iteration number
1[(a)]	**No converge**
2	11576
3	17388
4	13734
5	15424
6	4147
7	2081
8	1522
9	1023
10	1238
11	919
12	783
13	667
14	903
15	500

[(a)] NOTE: ANN with 1 neuron is not converged

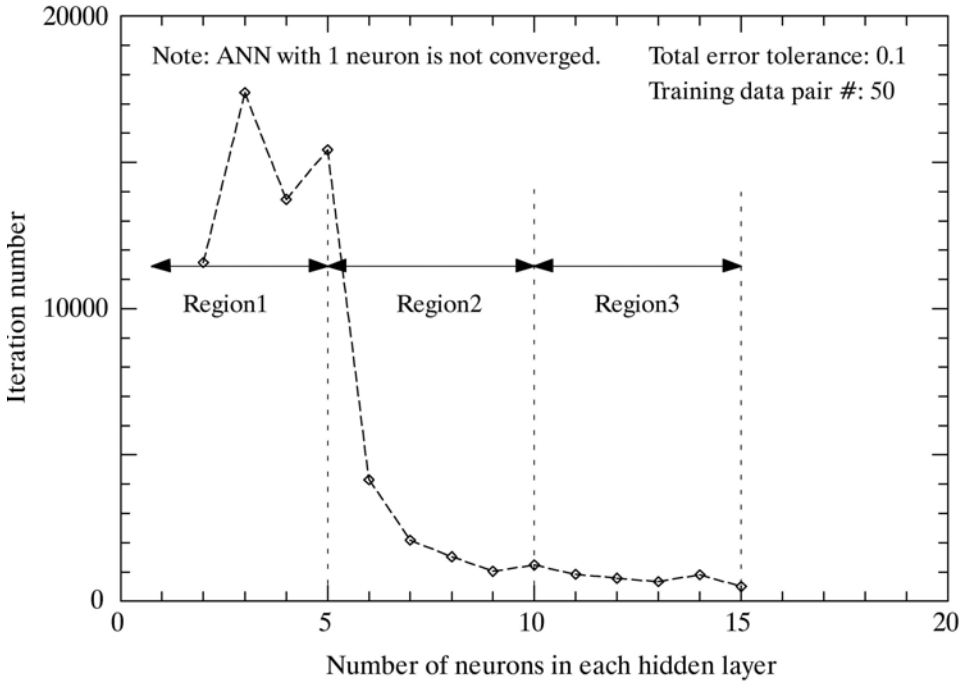

Figure 2.11 Iteration numbers required to complete the training of ANNs with different number of neurons from 1 to 15

In the second investigations, an ANN with 15 neurons was generated to examine the previous ANN result generated under the large error tolerance (i.e., 0.1). The ANN was trained with the smaller error tolerance (i.e., 0.001), and its result was compared to the preliminary-tested ANN with 3 neurons. Figure 2.12 shows force-displacement responses generated from the two trained ANNs and the training data. Each prediction result of the ANNs with 3 neurons and 15 neurons is depicted as a dashed and a solid line, respectively. The ANN trained under the smaller error tolerance can generate more accurate force-displacement response than the ANN previously trained under the large error tolerance. In addition, the training of the ANN including 15 neurons is completed with 12,815 iteration number, which is less than the iteration number (i.e., 17,388) required for the training of the ANN with 3 neurons. As a result, appropriate error tolerance and number of neurons need to be used to generate efficient and effective ANN models.

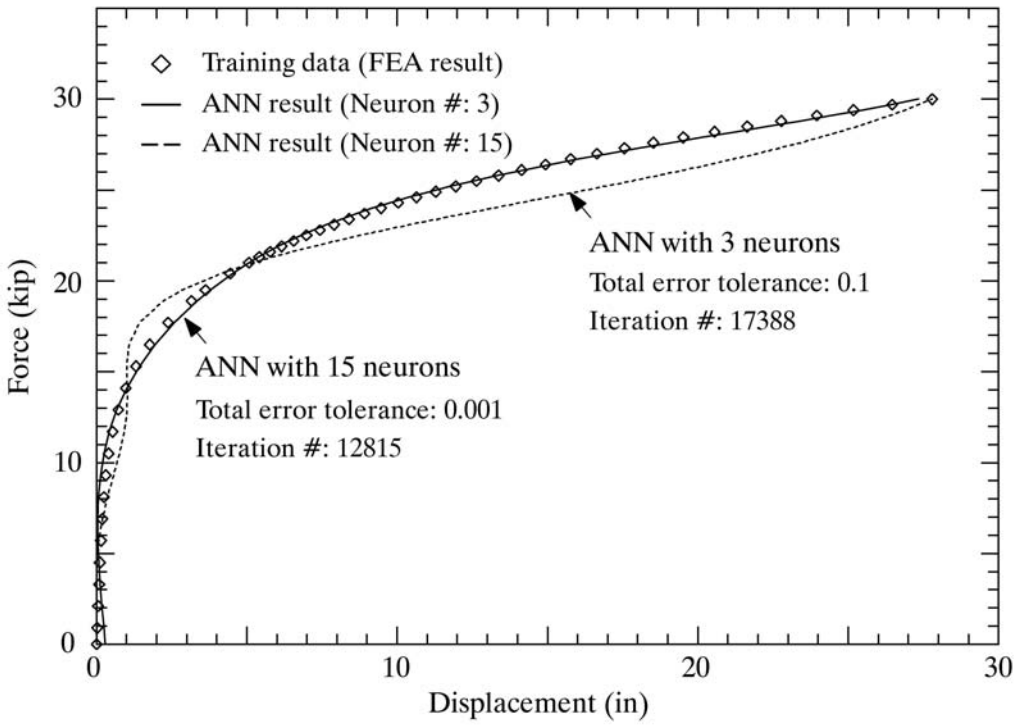

Figure 2.12 FEA and ANN results including 3 and 15 fixed neurons for different error tolerance

In the third investigation, another ANN was generated and trained using the adaptive training method. Unlike the previously trained ANNs, the ANN trained with the adaptive training method can add neurons in their hidden layers during training. If the ANN cannot produce a satisfactory result within given training iteration, it increases its capability by adding neurons. Through this adaptive training nature, appropriate ANN model can be efficiently generated without the parameter study for determining appropriate number of neurons. The ANN training started with 10 neurons but ended with 16 neurons. It took approximately 10 minutes using a personal computer (PC) with dual core CPU of 2.8Hz under multi-tasking environment. The error tolerance and iteration number used in this training were 0.001 and 5000, respectively. Figure 2.13 shows ANN prediction results and training data. The trained adaptive ANN generated accurate load-displacement response compared to the training data. The adaptive training method can efficiently generate appropriate ANN models without a parameter study to determine appropriate number of neurons. A typical convergence response of the adaptive training method with the iteration number of 1000 is also presented in Figure 2.14. This figure shows that the total error between ANN predictions and training data decreases as the training iteration number increases. Interestingly, the total error suddenly increases when a new neuron is added, and it oscillates but slowly converges when newly-added weights are adjusted. This may be because the adjustment of the newly-added weights is very sensitive to the total error function especially when the other existing weights are fixed. However, it converged in a stable manner when all weights are adjustable.

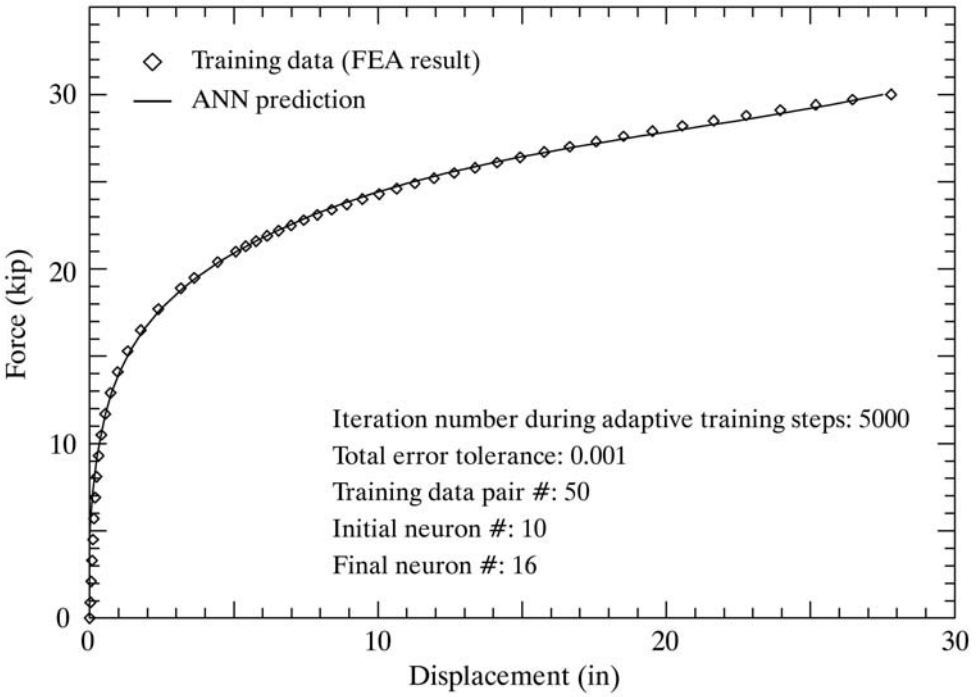

Figure 2.13 Training data (FEA result) and adaptive ANN training result

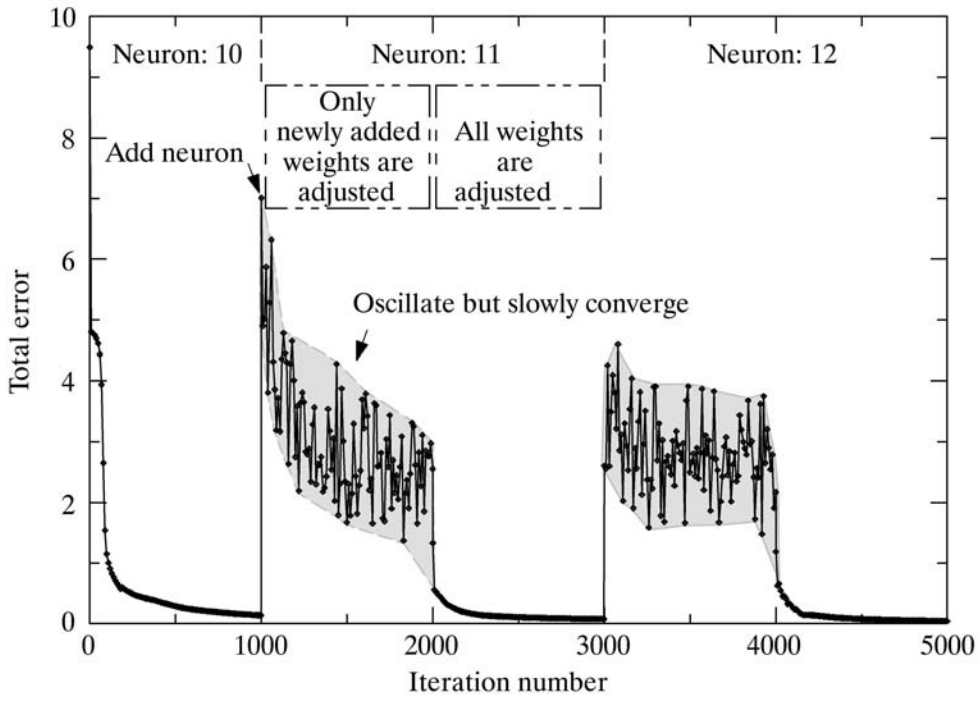

Figure 2.14 Typical convergence response of adaptive ANN training

CHAPTER 3: Nonlinear Isotropic ANN Models for Indentation Tests

The in-situ material properties of micro- and nano-scaled materials cannot be determined by conventional testing methods because they are easily affected by different factors that were not significant in macro-scale testing, such as small vibrations from an actuator, resolutions of the measuring equipment, and embedded residual stresses or defects during manufacturing. Nanoindentation has been extensively used to characterize the limited in-situ material properties such as elastic modulus and hardness of micro- and nano-scaled materials.

Nanoindentation has been shown to be promising technique for characterizing in-situ material parameters from the measured nanoindentation load-displacement response (Oliver and Pharr, 1922). However, nonlinear material parameters (e.g., hardening parameters and stress limits) cannot be directly generated by nanoindentation tests. Thus, many researchers have tried to use mathematical or analytical models to characterize the additional nonlinear material parameters from the nanoindentation load-displacement response. However, these models are either inefficient or limited in a specific material to be utilized as a practical method.

In this chapter, new ANN constitutive models are generated to characterize in-situ nonlinear material parameters only from the monotonic part of the nanoindentation load-displacement test results. The proposed ANN models can include different types of inputs and outputs (e.g., dimensionless input and output variables generated from nonlinear material parameters and simulated FEA results). In order to examine the capacity of the proposed ANN models, different ANN models are generated and trained with the simulated FEA results for various material properties. The ANN predictions are compared to the experiments and FE simulations that were not used in the training. The trained ANN including dimensionless input/output variables is used to back-calculate the in-situ

nonlinear material properties directly from the nanoindentation test results performed on a nanocrystalline copper film on a silicon substrate. The extracted nonlinear material behavior is also compared to the experimental data.

This chapter is divided into three major parts. The first part describes the 2D and 3D parametric FE models to generate training data of the proposed ANN models. In order to examine the developed FE models, sensitivity studies for different material properties of the film and substrate are performed for two different material systems (i.e., substrate with and without film). The second part deals with ANN modeling, training, and prediction verification. In this part, four different ANN models are generated for different input/output variables. The first two ANNs include dimensional input/output variables for different material properties, while the other two ANNs are generated with dimensionless input/output variables for two different material systems (i.e., substrate with and without film), respectively. The trained ANNs are investigated with simulated FEA results that were not used in the training process. The third part includes experimental verifications and using ANN in "inverse" material identification problems. Toward that goal, the trained dimensionless ANN models are used to generate in-situ nonlinear stress-strain responses from nanoindentation test results performed on a silicon (Si) substrate with and without a nanocrystalline copper (Cu) film. The extracted in-situ material response is compared to the existing experimental data from Bansal et al. (2004) and the prediction results are discussed.

3.1 Classical Indentation Tests

Classical indentation and nanoindentation have been generally used for determining hardness and elastic modulus from the load-displacement relationship of the tested material. Elastic and plastic deformations of the tested material can be shown generally in a small and localized region under the indenter tip. A typical depth of penetration can range from $100\,nm$ to $1\,\mu m$ depending on the type of

film material, force, and indenter tip shape (Vanlandinham et al., 2001). Nanoindentation technique employs high-resolution instrument to continuously control and monitor the mechanical responses as the indenter is driven into or withdrawn from the material system (Hay et al., 1999). Elastic modulus and hardness can be extracted from the load-displacement curve of the nanoindentation test using the analytical relations proposed by Oliver and Pharr (1992). For an axisymmetric indenter, the relations among the stiffness (S), the elastic modulus (E), and the projected area (A) can be described as shown in equations 3.1 and 3.2. The effect of the non rigid indenters on the indentation behavior can be accounted for by defining a reduced modulus (E_r) through equation 3.2.

$$S = \frac{dP}{dh} = \frac{2}{\sqrt{\pi}} E_r \sqrt{A} \tag{3.1}$$

$$\frac{1}{E_r} = \frac{(1-\nu^2)}{E} + \frac{(1-\nu_i{}^2)}{E_i} \tag{3.2}$$

Where, E and ν are the elastic modulus and the Poisson's ratio of the specimen, and E_i and ν_i are for the indenter.

The stiffness can be experimentally measured using the upper portion of unloading data, and the projected area can be obtained using an empirically fitted function described in equation 3.3. Thus, the reduced elastic modulus (E_r) can be derived using equation 3.1, and the hardness of materials can be determined using equation 3.5.

$$A = f(h_c) \tag{3.3}$$

$$h_c = h_{total} - \frac{\varepsilon P}{S} \tag{3.4}$$

Where, h_c is determined using the following equation that is derived from the elastic contact theory; h_{total} is the displacement of the indenter tip, and ε is a constant which depends on indenter geometry.

$$H = \frac{P}{A} \tag{3.5}$$

Figures 3.1 and 3.2 show a schematic representation of load-displacement response and that of a typical section through an indentation experiment, respectively.

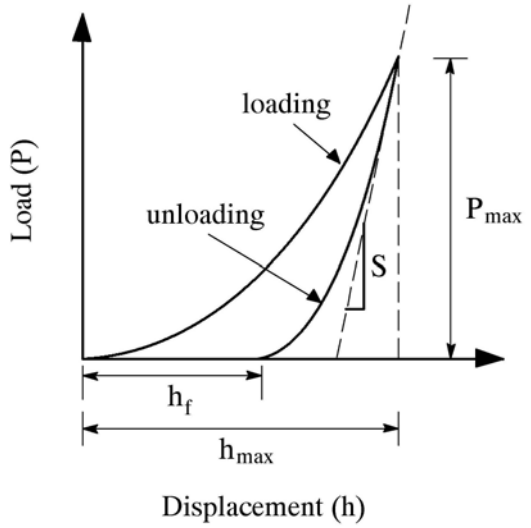

Figure 3.1 A schematic representation of load versus indenter displacement data for an indentation experiment. The quantities shown are P_{max} : the peak indentation load; h_{max} : the indenter displacement at peak load; h_f : the final depth of the contact impression after unloading; and S: the initial unloading stiffness (Adapted from Oliver and Pharr, 1992)

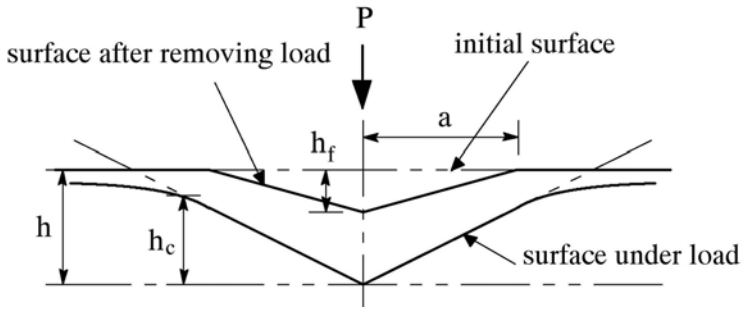

Figure 3.2 A schematic representation of a section through an indentation showing various quantities used in the analysis (Adapted from Oliver and Pharr, 1992)

3.2 Nanoindentation FE Models

Material Systems

In this chapter, two major material systems (i.e., substrate with and without film) have been used as shown in Figure 3.3. The first material system is a nonlinear and inelastic (e.g., metals). The second material system consists of a nonlinear film or coating on a substrate, which can be either a linear elastic substrate or a nonlinear and inelastic substrate, representing hard and soft substrates. Indentation tests and FE simulations are conducted for both material systems in order to generate the indentation response for training and verification. In order to examine the prediction capability of the proposed ANNs, both two material systems are used with a film of different linear/nonlinear stress-strain relations and Poisson's ratios. In this chapter, incremental plasticity coupled with one-dimensional (1D) Ramberg-Osgood stress-strain relationship is used to generate inelastic isotropic hardening behaviors as follows:

$$\frac{\varepsilon}{\varepsilon_0} = \left(\frac{\sigma}{\sigma_0}\right)^n \qquad \left\{\begin{array}{ll} \varepsilon < \varepsilon_0 & \sigma = E\varepsilon \\ \varepsilon \geq \varepsilon_0 & \sigma = \sigma_0 \left(\frac{\varepsilon}{\varepsilon_0}\right)^{\frac{1}{n}} \end{array}\right\} \tag{3.6}$$

Where the parameters used are E: the elastic modulus; n: the hardening parameter; ε_0: the strain limit; and σ_0: the stress limit.

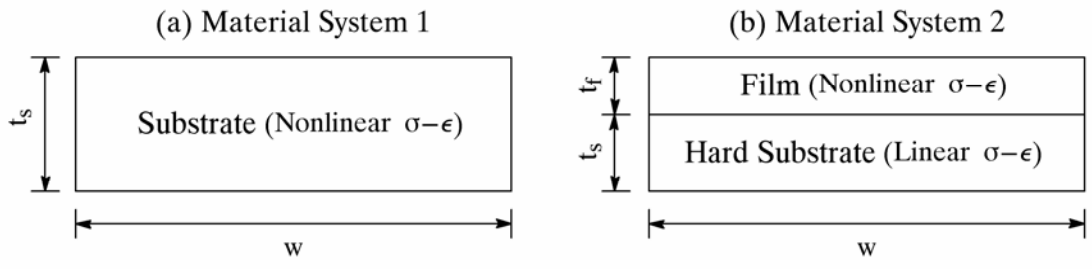

Figure 3.3 Structure of the material systems used in this chapter

This chapter presents 2D and 3D FE indentation models to develop the FE-ANN relationships and generate indentation responses (i.e., load-displacement behaviors). These FE models are used for the previously mentioned two material systems. ABAQUS, which is a general purpose implicit finite element code, has been extensively used in this chapter. The proper size of the meshes for the 2D and 3D FE models is determined through convergence studies. The loading process of the FE simulations is performed by penetrating the conical or the Berkovich indenter into a film or substrate in 2D and 3D models, respectively. The unloading process of the FE simulation is conducted by returning the applied indenter to its original position by controlling the indenter depth. The load corresponding to the applied displacement is calculated by summing the resistant force at the bottom nodes of the specimen that is equivalent to the indenter force. The FE simulations show force oscillations with increasing indentation, especially for materials with higher stress limits (or yield) and larger hardening parameters. This can be attributed to several factors, such as contact behavior of the indenter as it interacts with more elements with severe geometrical deformations. Other factors can compound this behavior, such as the size of FE meshes and the imposed strain increments. These FEA responses can be improved by using more refined FE meshes and smaller displacement increments, but it will require larger computational efforts. Therefore, the proper incriminations and the size of the meshes for the 2D and 3D FE models were determined in order to generate efficient FE models with minimum computational efforts.

Axisymmetric 2D FE model

Figure 3.4 shows the geometry of a typical 2D model used in this chapter. This model can have a film layer and a substrate, both of which consist of four-node axisymmetric elements with reduced integration points (CAX4R). A rigid surface is used to model the conical indenter. In this nanoindentation case, the film has a 4,000nm depth and a 200,000nm width, and the substrate has a 700,000nm depth. Perfect displacement continuity is imposed at the interface between the film and substrate. This model consists of 1,367 nodes and 1,247 elements are generated with biased non-

uniform elements with long rectangular shape especially near the tip area. This is done in order to minimize the strains in the element under the indenter. The minimum length of each element is 20nm. In this model, a conical-shape indenter is used with an angle of 70.3 degrees representing the same depth-to-area relation as the 3D Berkovich indenter. The radius of the conical indenter is 50nm. The indenter is constrained to move only in the thickness-direction (z) of the film layer. The nodes at the bottom of the substrate are constrained in the z and r-directions, while the nodes on the axisymmetric axis can move only in the z-direction. The indenter is constrained to move monotonically with increasing indenter depth (displacement control). The reaction load versus displacement of the indenter is taken as measures representing the material system response. Parametric FE simulations consisting of load versus indenter depth for different geometries and material parameters are used to train the different ANNs in this chapter.

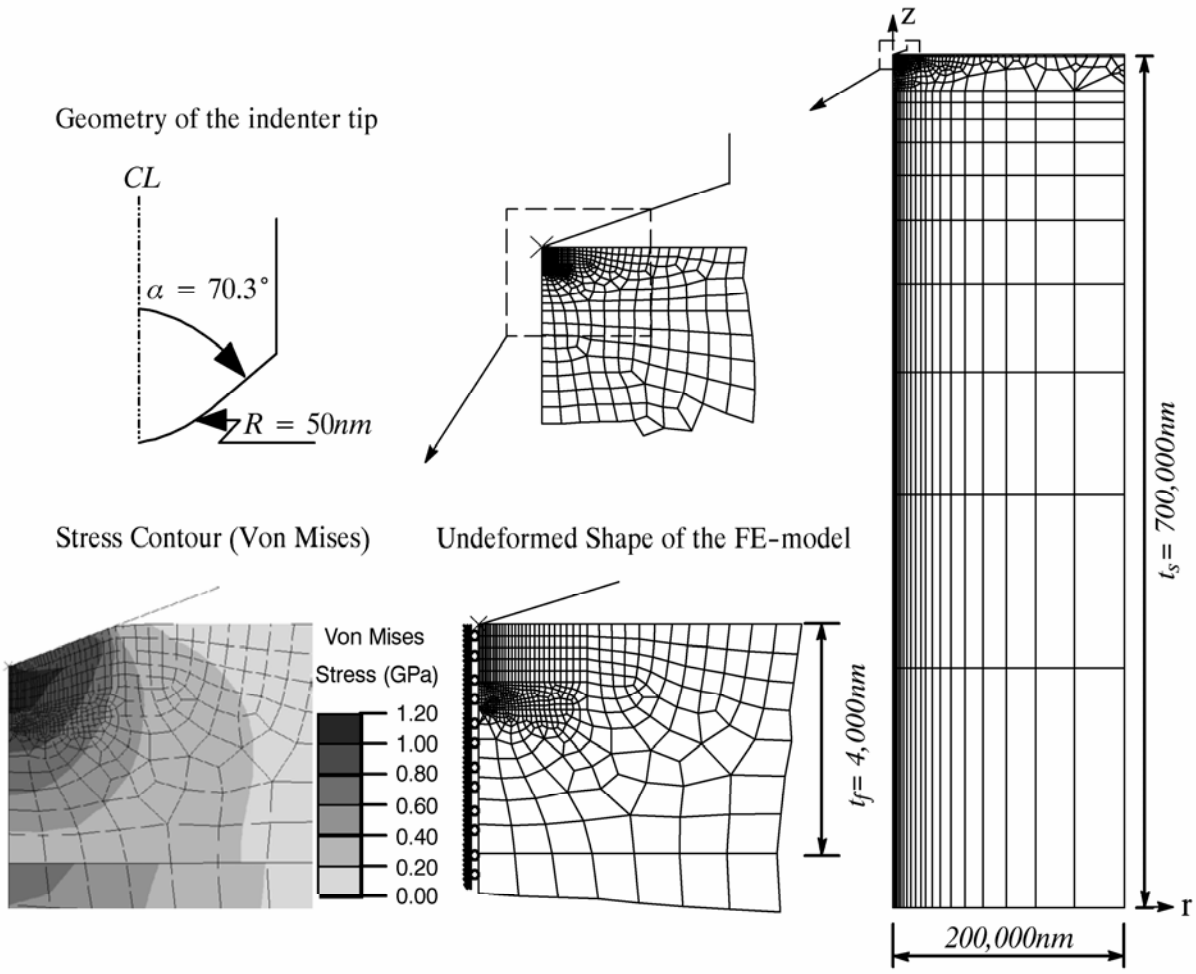

Figure 3.4 A representative two-dimensional indentation FE model for material system 2

Three-dimensional (3D) FE model

This chapter primarily uses 2D FE models for simulating the indentation tests due to their simplicity and computational efficiency combined with reasonable accuracy. Never-the-less, the 2D models cannot exactly represent the 3D nature of the indentation test (e.g., different 3D geometries of the indenter and 3D stress fields of the material under the indenter). Therefore, to compare the results from the 2D model, three dimensional FE simulations were also carried out. Figure 3.5 shows a typical 3D model used in this chapter. In order to save computational effort, a one-sixth symmetric model is used. The refined 3D model is composed of the Berkovich indenter, film, and substrate. The film and substrate are modeled with eight-node brick elements with reduced integration (C3D8R). However, six-node triangular-prism shape elements (C3D6) are used adjacent to the symmetric axis. The 3D model consists of 6,125 nodes and 5,371 elements. The minimum length of the elements at the tip area is 30nm. The size of the elements generally increases at a distance away from the tip area. The Berkovich indenter is explicitly modeled in the 3D FE model, and its surface is captured with a rigid shell surface (R3D4). The shape of the Berkovich indenter tip is considered spherical with a radius of 50nm, which is comparable to the indenter used in the experimental part of this chapter. A linear transition between the half spherical tip shape and the Berkovich pyramid shape is done over 80nm height. The nodes at the bottom of the substrate are fixed. The “1/6” symmetric surfaces are restrained from moving in their out-of-plane direction. The 3D FE simulations are performed for both loading and unloading processes in order to compare the 3D results with the test and 2D results.

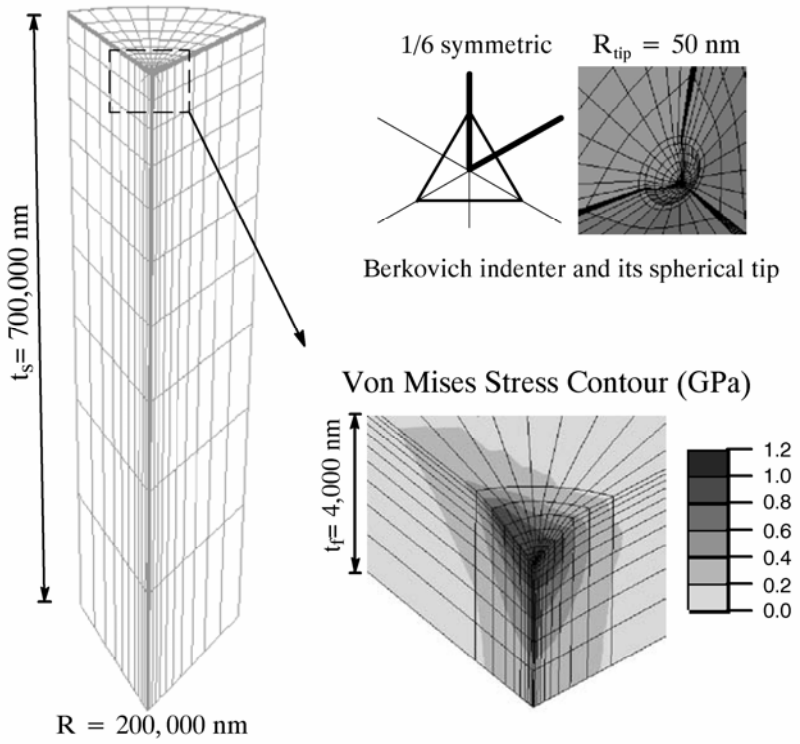

Figure 3.5 A representative 1/6 symmetric three-dimensional FE model for material system 2

Effect of the linear and nonlinear material behaviors of the film and substrate

The effect of the nonlinear material behavior on the indentation response is examined for a film-substrate material system. Both linear and nonlinear material behaviors of the copper film and the silicon substrate are used in this investigation. Figure 3.6 shows indentation simulation responses for four different material combinations (i.e., film-substrate modeled as linear-linear, linear-nonlinear, nonlinear-linear, and nonlinear-nonlinear; respectively). The FE indentation simulations are performed under the displacement control. The indenter is advanced to the 75% of the film's thickness, in order to induce a relatively large inelastic response. The simulation results in Figure 3.6 show that the linear-linear case presents the stiffest response, while the nonlinear-nonlinear case shows the softest response. The nonlinear effect of the substrate increases with high indentation depth, but it is not pronounced. Therefore, the substrate can be considered as linear for shallow or small indentations.

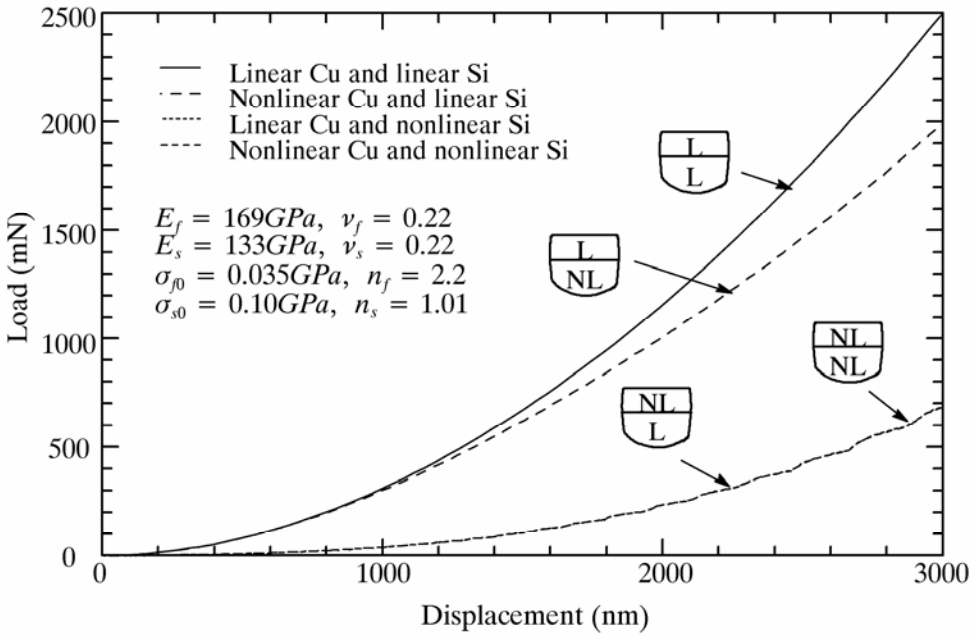

Figure 3.6 Effect of the linear and nonlinear material behaviors of the film and substrate

Sensitivity of the material properties of the film and substrate

Parametric FE simulations are conducted to examine the effect of the material properties (e.g., Young's modulus, stress limit, and hardening parameter) on the indentation response. The selected material system is a film on a linear substrate. Simulations are performed with a rigid conical indenter that is advanced up to 700 nm. This sensitivity study can be divided into three studies. In the first part, the effect of the elastic modulus of the substrate on the overall indentation response is investigated. Six different elastic moduli are used for the substrate (50, 100, 200, 333, 500, and 1,000GPa), while the material properties of the film layer are fixed (100GPa). Both the film and substrate materials are considered linear. As expected, Figure 3.7 shows that as the elastic modulus ratio (E_f / E_s) increases, the indentation force also increases for the same indentation depth. However, for a hard film on a softer substrate, the increase in indentation force is not evident beyond a critical stiffness ratio of the two. This means that beyond a critical hard film coat ratio, the overall

indentation response is not affected by the substrate. Thus, the effect of the substrate nonlinearity should be considered in the case of a hard film. In the second part, the effect of the stress limit of the film layer is examined with six different limit values (0.01, 0.03, 0.06, 0.10, 0.20, and 0.30GPa). All other material properties of the film and the substrate are fixed. Figure 3.8 shows that the overall indentation load increase as the stress limit increases. The third sensitivity study is performed with five different hardening parameters for the film layer (1.0, 1.1, 1.5, 2.0, and 3.0), while other material properties are fixed. Figure 3.9 shows that as the hardening parameter (n) of the film decreases, the indentation response increases.

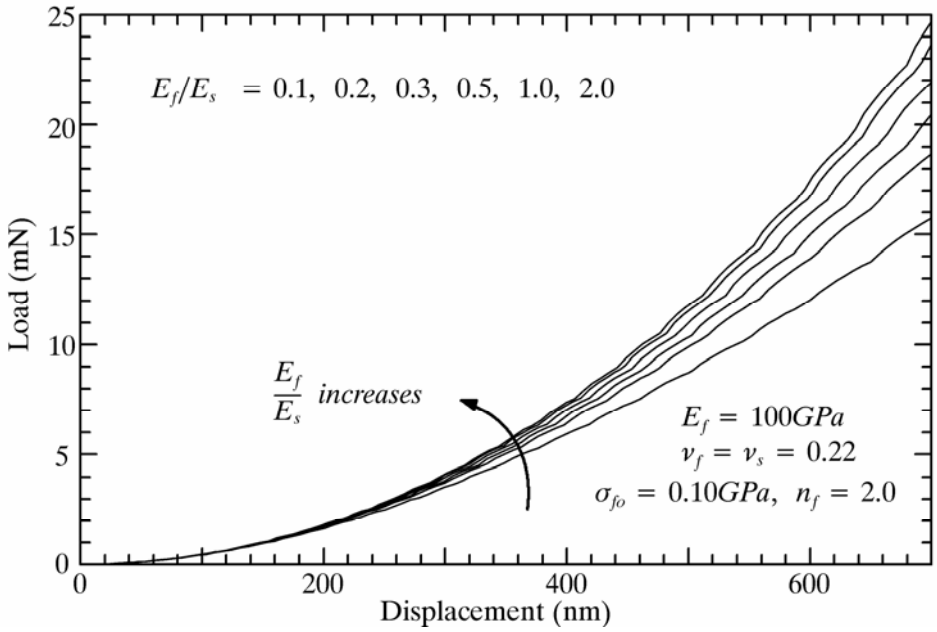

Figure 3.7 Sensitivity of the Young's modulus ratio (E_f / E_s)

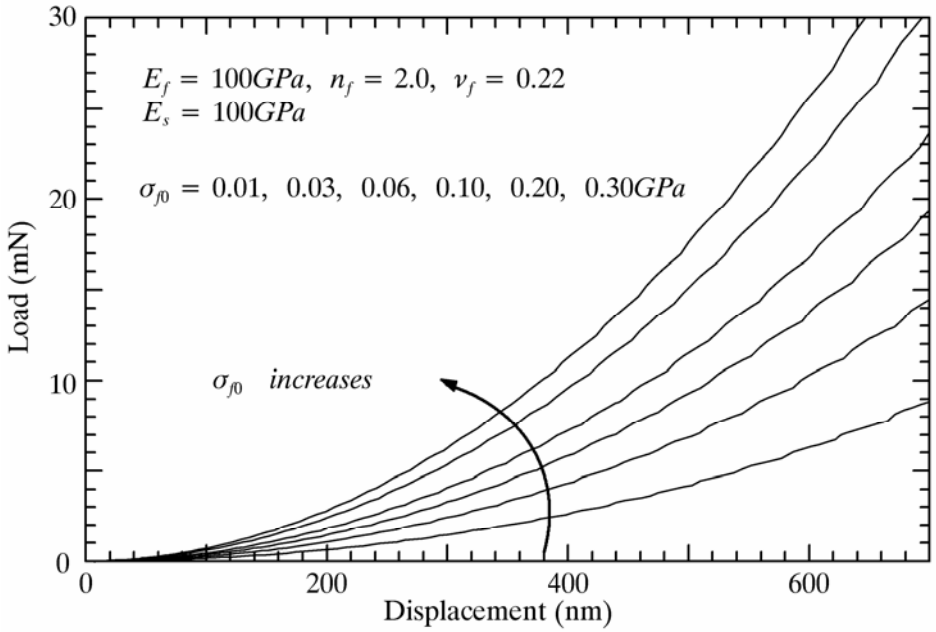

Figure 3.8 Sensitivity of the stress limit of the film

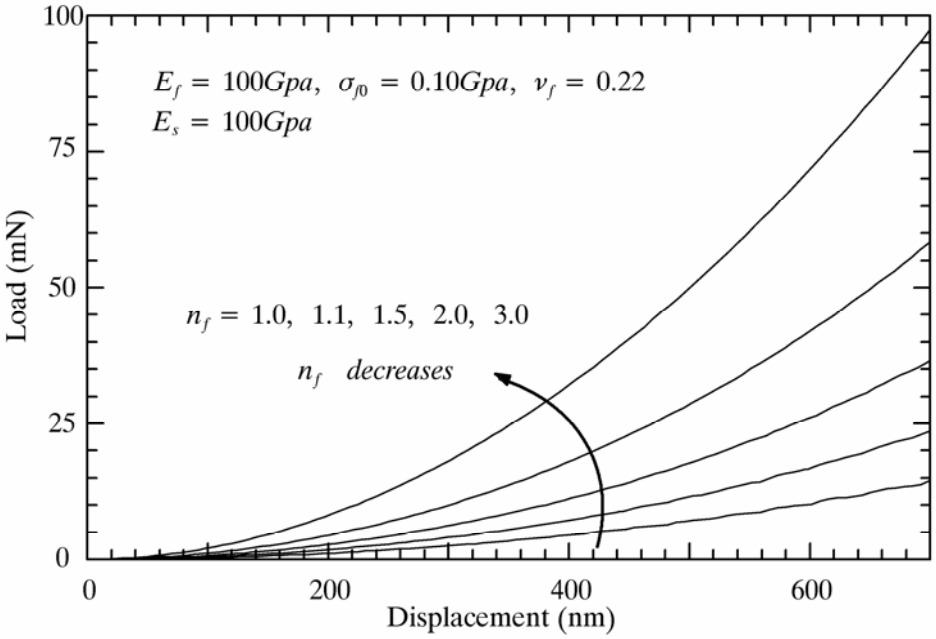

Figure 3.9 Sensitivity of the hardening parameter of the film

3.3 Proposed ANN Parametric Indentation Models

The general structure of the proposed ANN is described in Figure 3.10. It includes one input layer, one output layer, and two feed-forward type hidden layers. The middle two layers are constrained to have the same number of neurons. The input layer scales the physical variables to a common range (-0.9, 0.9), while the output range is taken as (0.2, 0.8). The latter range has the highest sensitivity of the sigmoid function used as the activation in each neuron. The number of neurons in the hidden layers simultaneously increases during the training process. Training usually starts with a small number of neurons and random weights that are constantly updated until they provided a satisfactory error in the output. In general, the training ends up with a larger number of neurons compared to that of initial neurons as shown in Figure 3.11. The weight connections among the layers are determined by minimizing the total error, and equation 3.7 shows the definition of the total error used in this chapter.

$$error = \frac{1}{2}\sum_{n}\left\|T_i - O_i\right\|^2 \tag{3.7}$$

Where T and O are input and output vectors in the training process, “n” is the number of training data set, and “i” is the number of nodes in the hidden layer.

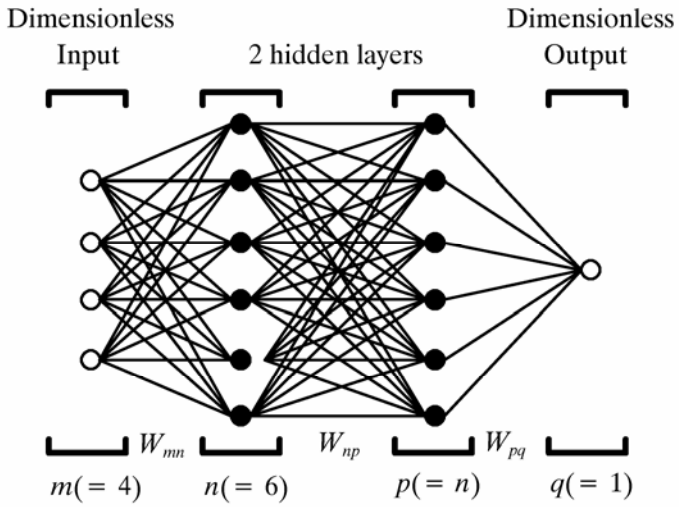

Figure 3.10 General structure of a feed-forward ANN used in this chapter two hidden layers, multiple inputs, and one output. The converged weights are represented in the matrices, Wmn, Wnp, and Wpq. Here m, n, p, q are the number of neurons in the input, first and second hidden, and output layer, respectively.

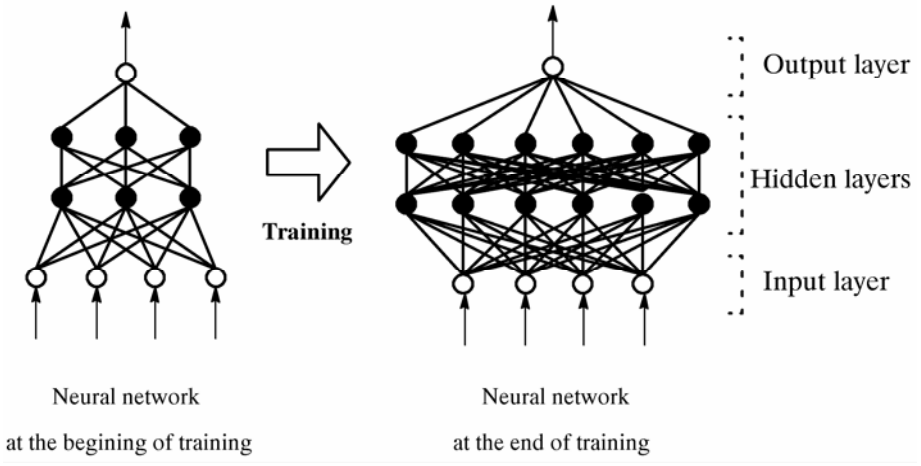

Figure 3.11 A schematic drawing of the evolution of ANN structure during training

Simplified ANN models for coated materials

In order to demonstrate the ANN modeling ability for the indentation response of two material systems, two simplified ANNs are generated. The first material system is a linear "hard" film (or coating) on a linear substrate. The second is a nonlinear film on a linear substrate. The first ANN consists of three input variables in the form of film's elastic stiffness, Poisson's ratio, and indentation depth (i.e., E_f, ν_f, and Δ). The output for this ANN is the corresponding force (F). Finite element simulations (Δ versus F) were generated for 25 different material systems, including combinations of five different Poisson's ratios with five elastic moduli. These combinations are:

$$\begin{aligned} E_f &= 100,\ 120,\ 140,\ 160,\ 180 \quad (GPa) \\ \nu_f &= 0.1,\ 0.2,\ 0.3,\ 0.4,\ 0.5 \end{aligned} \tag{3.8}$$

Where, the substrate properties are assumed constant ($E_s = 133GPa$, $\nu_s = 0.22$).

A total of 2,670 data sets are generated for this ANN training. The FE simulations are performed for the indentation depth of 500nm. The ANN training starts with five neurons in the hidden layers and ends up with 24 neurons (nodes). Figure 3.12 describes the prediction results generated from the trained ANN. The indentation load-displacement predicted by the ANN is plotted and compared with FE simulation results for different film's elastic stiffness and a fixed Poisson's ratio of 0.2. The results show a good prediction of the load-displacement indentation response for cases used in the training. In addition, the ANN response is compared favorably for a case (E_f = 150GPa) that was not used in the training. This illustrates the prediction ability of the ANN to extrapolate between different input variables. Figure 3.13 shows the ANN prediction and FE simulation results with changing Poisson's ratios when the elastic modulus is set to 100GPa. The ANN sensitivity for changing Poisson's ratios is demonstrated when compared with the FE simulation results for a wide range of Poisson's ratios. The last two figures describe the prediction ability of the first simplified ANN for a hard (linear) film and substrate system.

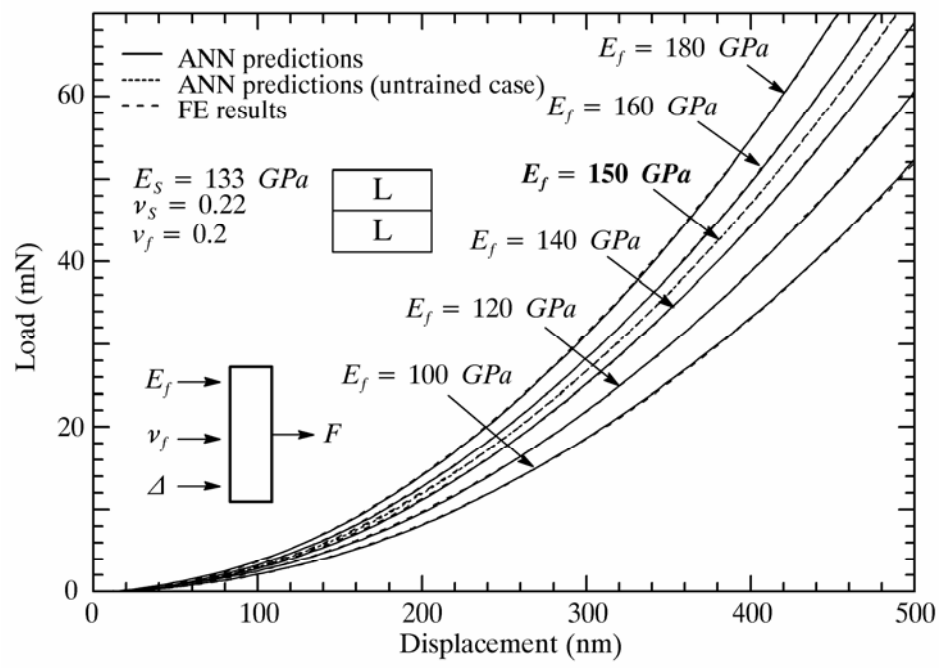

Figure 3.12 ANN predictions for the different Young's moduli of a linear film on a linear substrate

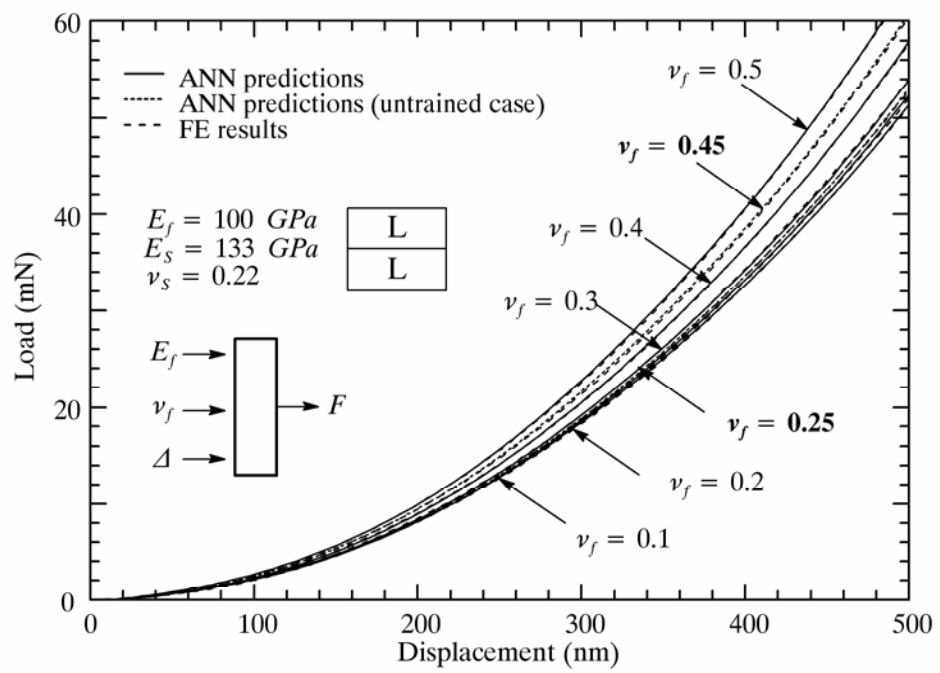

Figure 3.13 ANN predictions for the different Poisson's ratios of a linear film on a linear substrate

The second ANN is used to model the indentation response of a nonlinear film on a hard (linear) substrate. To that end the general ANN was constructed with input variables that consist of the two parameters of the film or coat (n, σ_0) in addition to the indentation depth (Δ) that ranges from zero to 700nm. The output of the second ANN included the indentation force (F). The FE simulations were performed to generate (F) versus (Δ) relations for 48 different nonlinear material properties of the film. Eight different hardening parameters and six different stress limits were used, while the other properties are fixed. The material properties used in the second ANN model are:

$$\begin{aligned} n &= \quad 1.0, \quad 1.1, \quad 1.2, \quad 1.3, \quad 1.5, \quad 1.8, \quad 2.0, \quad 3.0 \\ \sigma_0 &= \quad 0.02, \quad 0.025, \quad 0.03, \quad 0.04, \quad 0.05, \quad 0.06 \quad (GPa) \end{aligned} \tag{3.9}$$

Where, the other material properties are assumed to be constant ($E_s = 133GPa$, $\nu_s = 0.22$, and $\nu_f = 0.22$).

The 48 FE simulations resulted in a total of 5,750 training data sets that each consist of three inputs (n, σ_0, and Δ) and one output (F). Five initial neurons (nodes) are used in the adaptive training. The second ANN consists of 33 neurons in each hidden layer at the converged ANN after training completed. The ANN prediction results are compared with FE simulations for cases not used in the training process. An asterisk symbol is used to denote parameter cases that were not used in the training process. Figure 3.14 shows indentation responses generated from the FE simulations and trained ANN models. The curves are plotted for a fixed film stress limit of 0.03GPa and different hardening parameters. The indentation response predicted by the trained ANN shows good comparison with the FE simulations for hardening cases that were not used as part of the original training. However, for hardening parameters larger than n=2.0 the ANN prediction are less accurate, perhaps due to lower sensitivity (shallow curves) of the indentation response in this range. Figure 3.15 illustrates the ANN prediction results for different stress limits. Cases for FE simulations that are not part of the training were highlighted. Overall, good predictions are demonstrated.

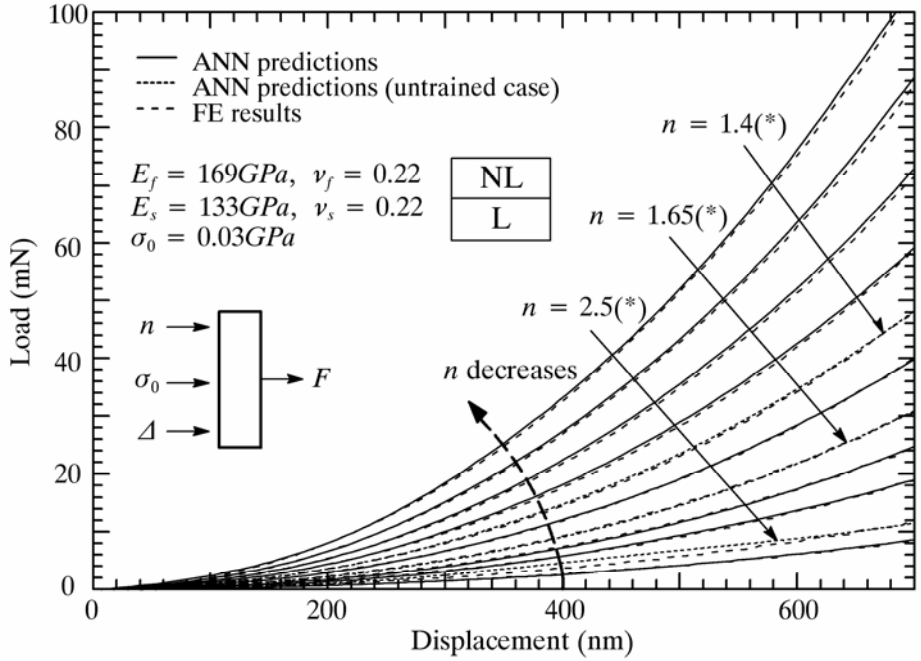

Figure 3.14 ANN predictions for different hardening parameters in a film on a hard substrate

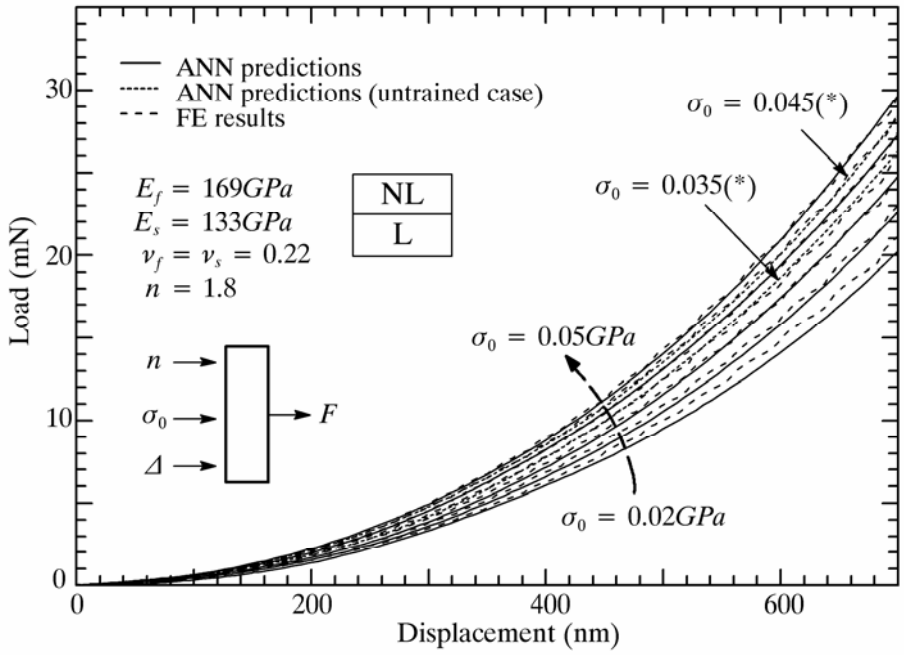

Figure 3.15 ANN predictions for different stress limits in a film on a hard substrate

Dimensionless FE-ANN model for a substrate without a film

In this chapter, two dimensionless ANNs are proposed for two different material systems (Figures 3.3a and 3.3b). The first is a substrate-only system (Figure 3.3a), while the second includes a nonlinear film or coating on a hard substrate (Figure 3.3b). The proposed ANNs have dimensionless input and output variables. The dimensionless inelastic responses for plasticity based models are known to be invariant for a whole indentation process, i.e. loading and unloading process, (Huber et al., 2002). The structure of the dimensionless ANNs extends the prediction capability of the ANN. In order to train these ANNs, a relatively small number of FE simulations are conducted up to 700nm indentation depth with different material properties of the film and substrate. The dimensionless ANN inputs and output are expressed as follows:

$$\overline{\Delta} = \frac{\Delta}{r_0},\ \overline{\sigma_0} = \frac{\sigma_0}{E_f},\ \overline{E} = \frac{E_f}{E_s},\ \overline{F} = \frac{F}{E_f {r_0}^2} \tag{3.10}$$

The 2D conical relation between the changing indenter radius and the projected indenter area, which matches the Berkovich indenter, is $A = 24.56\left(\frac{r}{\tan\alpha}\right)^2$. Here, r is the changing cone radius. In order to have a dimensionless ANN, a length scale is needed. In this chapter, we selected this length scale based on the value of r at a projected contact area of A=1 μm^2. This results in $r_0 = 563nm$.

The first dimensionless ANN model is proposed to predict the indentation response for the substrate-only system (Figure 3.3a). The corresponding general dimensionless ANN consists of input variables in the form of a hardening parameter, normalized stress limit, and the normalized indentation depth (n, $\overline{\sigma_0}$, and $\overline{\Delta}$). The output is the dimensionless indentation force ($\overline{F}$). In order to train the ANN, finite element simulations are performed with 56 different material properties, combined with eight different hardening parameters and seven different stress limits for the substrate.

All other material properties are fixed. The following are different hardening parameters and stress limits used in the first ANN training, and they were determined through FE parametric studies:

$$\begin{aligned} n &= \quad 1.0, \quad 1.15, \quad 1.3, \quad 1.5, \quad 1.8, \quad 2.2, \quad 3.0, \quad 5.0 \\ \overline{\sigma_0} &= \quad 4, \quad 8.5, \quad 18, \quad 40, \quad 85, \quad 180, \quad 400 \qquad (\times 10^{-5}) \end{aligned} \tag{3.11}$$

Where, the constant material properties are E= 100GPa and v=0.2.

Figure 3.16 shows FE simulation and ANN prediction results when the hardening parameter is five (n=5). This value was chosen as close to elastic-plastic material which yields a highly nonlinear indentation response. The ANN prediction ability was tested using stress limits that were not part of the training data. The four tested cases are for $\overline{\sigma_0} = 2.5\times10^{-4}$, 5.8×10^{-4}, 1.2×10^{-3}, and 2.5×10^{-3}. These curves are marked with asterisks in Fig. 14 and show good prediction ability by the ANN. Figure 3.17 shows the ANN prediction results for a fixed normalized stress limit ($\overline{\sigma_0} = 4\times10^{-4}$) and changing hardening parameters for cases used and not used in the training process. The prediction ability of the ANN is excellent for a relatively wide range of hardening parameters n=1.4, 1.65, 2.0, and 2.6.

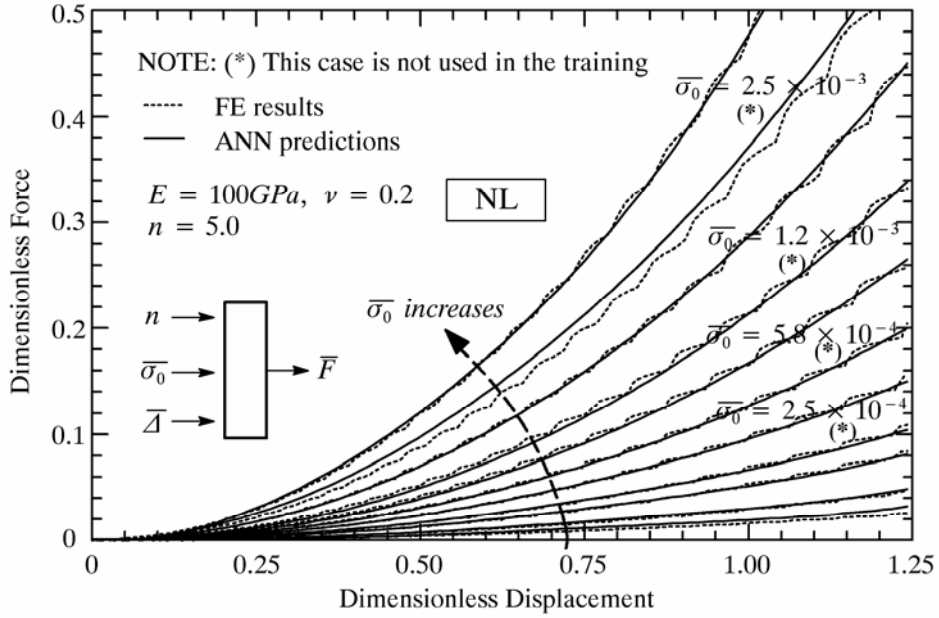

Figure 3.16 ANN predictions with different dimensionless stress limits

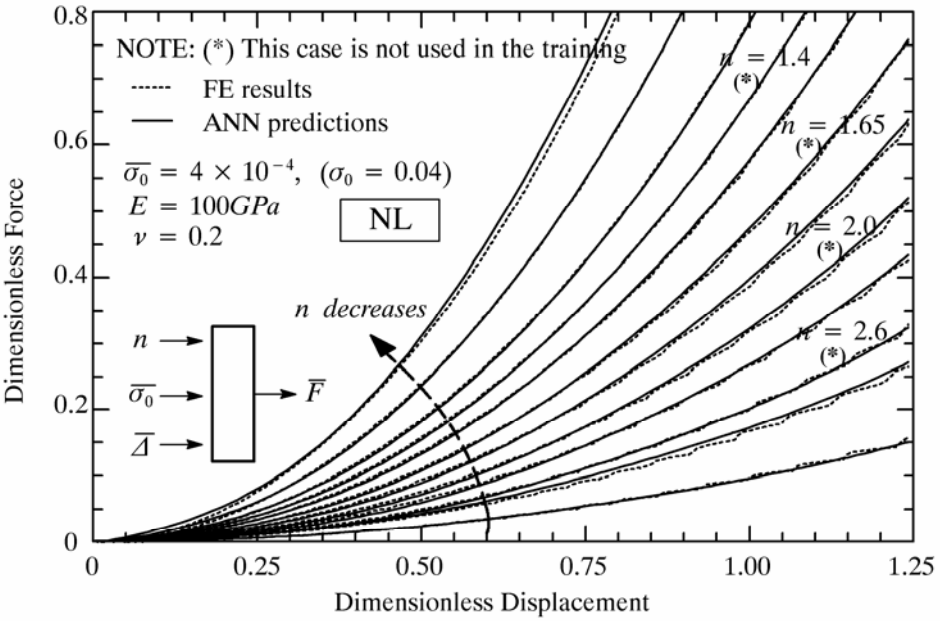

Figure 3.17 ANN predictions with different hardening parameters, n

Dimensionless FE-ANN model for a substrate with a film

The second dimensionless ANN is proposed for a film (coating) on a substrate (Figure 3.3b). Similar to the previous dimensionless ANN, the current ANN is composed of four dimensionless inputs (n, $\overline{\sigma_0}$, $\overline{E}$, and $\overline{\Delta}$) and one output $(\overline{F})$. The current ANN includes one more input variable: the elastic modulus ratio between the film and substrate $(\overline{E})$. This enables the ANN to consider the effect of different substrates on the overall indentation response. Adaptive training is used for this ANN. It starts with five neurons (nodes) but ends up with 36 neurons. The schematic drawing of this dimensionless ANN is shown in Figure 3.18. The inputs and output of the ANN are converted to dimensionless terms using equation 3.10. However, the thickness of the film layer (t_f) is used as a natural length scale instead of the radius (r_0) that was previously used in the substrate-only system. Finite element simulations are conducted with 280 different material properties including eight different hardening parameters, seven different stress limits of the film layer, and five different film-substrate elastic modulus ratios:

$$\begin{array}{lllllllll} n = & 1.0, & 1.15, & 1.3, & 1.5, & 1.8, & 2.2, & 3.0, & 5.0 \\ \overline{\sigma_0} = & 4, & 8.5, & 18, & 40, & 85, & 180, & 400 & (\times 10^{-5}) \\ \overline{E} = & 0.2, & 1.4, & 2.6, & 3.8, & 5.0 & & & \end{array} \qquad (3.12)$$

Where, the other material properties are fixed ($E_f = E_s$ = 100GPa, $\nu_f = \nu_s$ = 0.2), and the thickness of the film is assumed to be 4 μm.

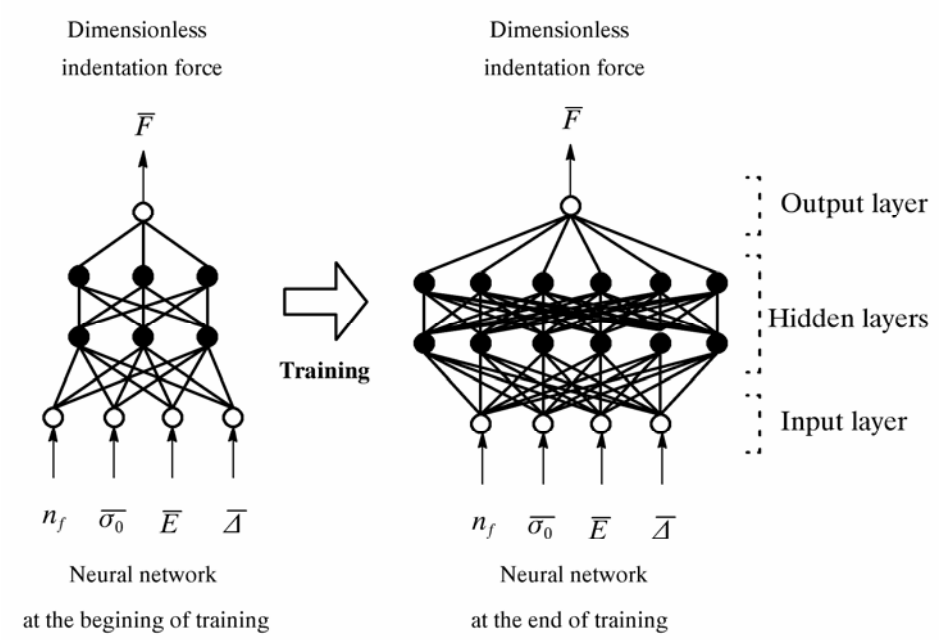

Figure 3.18 Schematic drawing of the dimensionless ANN trained to simulate indentation response of a film on a hard substrate system

Figure 3.19 shows indentation responses generated from the ANN and FE simulations with different stress limits, while all the other variables are fixed. The prediction results are compared with four additional FE simulations for different stress limits, not used in the training ($\overline{\sigma_0}$ =1.2×10^{-4}, 2.5×10^{-4}, 5.8×10^{-4}, and 1.2×10^{-3}). The trained ANN predicts the indentation responses for a relatively wide range of stress limits. Figure 3.20 also shows the ANN prediction and FE simulation results with different hardening parameters, while the other variables are kept constant. Indentation responses predicted by the ANN for four different hardening parameters (n= 1.4, 1.65, 2.0, and 2.6), which are not used in the training process, are also compared with FE simulation results. The prediction capability of the trained ANN is also effective for different hardening parameters as shown in Figure 3.20. Finally, Figure 3.21 shows the ANN prediction compared with FE simulation results for changing elastic modulus ratios after fixing the other variables. It also shows that the proposed ANN is effective when predicting the indentation for four different elastic modulus ratios

($\overline{E}$ = 0.8, 2.0, 3.2, and 4.4), which are not used in the training. The prediction capability of the dimensionless ANN is very effective for different material properties of the film on a substrate system. This enables the new ANN models to be used in solving different inverse problems and designing new material systems with different in-situ material properties.

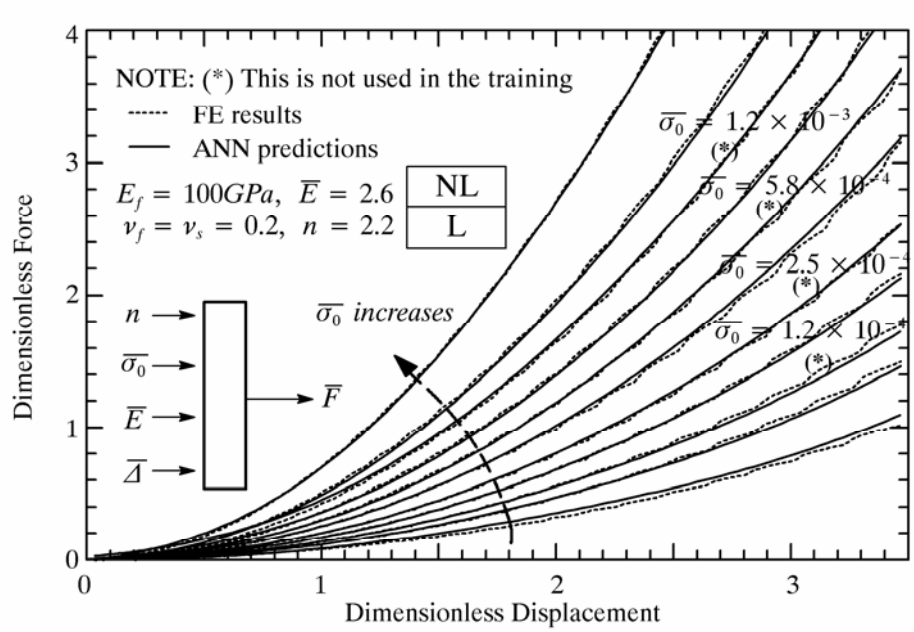

Figure 3.19 ANN predictions for indentation force-displacement of a film on a substrate with different film's stress limits

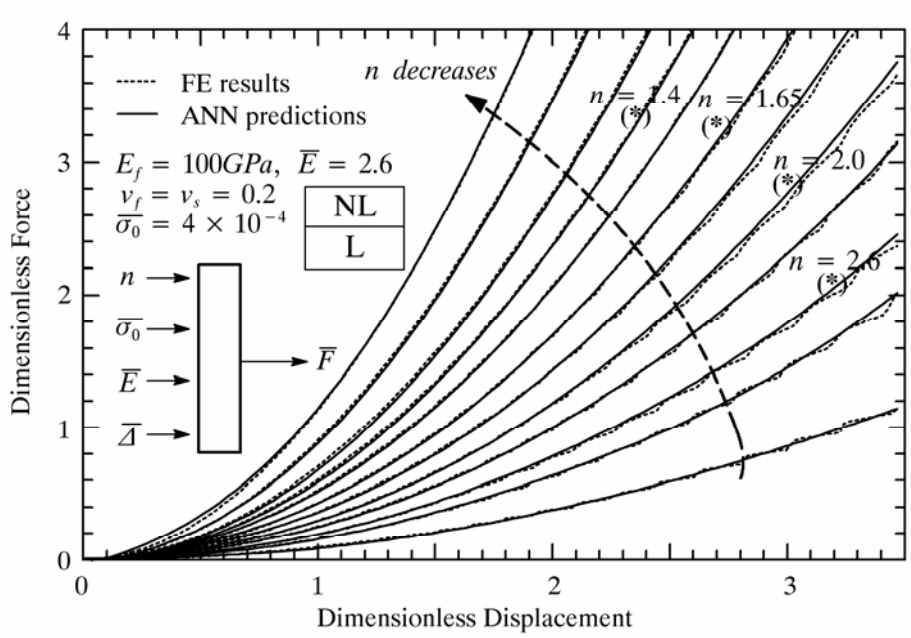

Figure 3.20 ANN predictions for indentation force-displacement of a film on a substrate with different film's hardening parameters

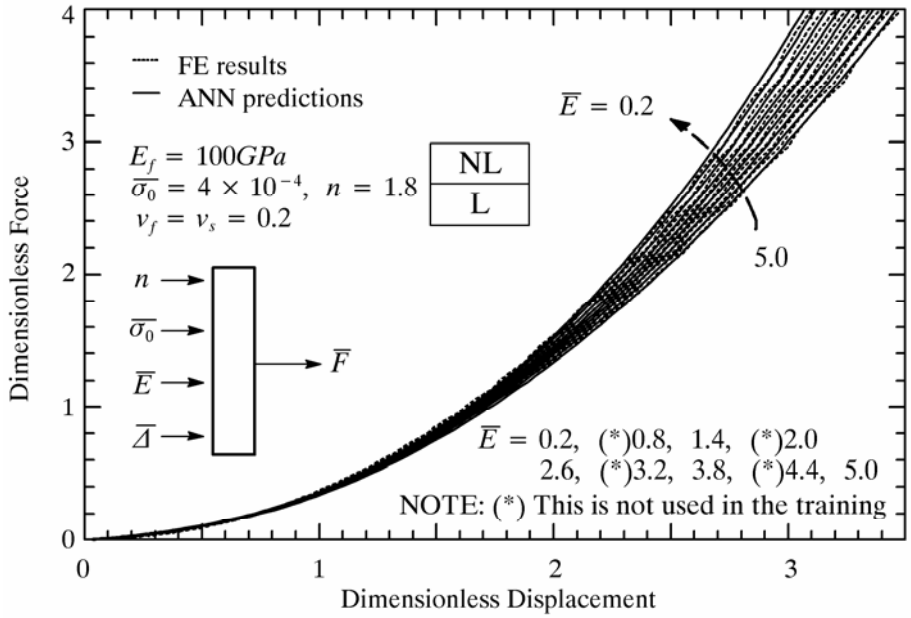

Figure 3.21 ANN predictions for indentation force-displacement of a film on a substrate for different elastic modulus ratios

3.4 Experimental Verifications

In this chapter, in order to verify the FE-ANN prediction results, indentation experiments were performed with the MTS Nano indenter XP system (MSE at the Georgia Institute of Technology) equipped with a diamond Berkovich, of which the radius is about 40-60nm. The experiments were conducted by pushing the indenter into the specimen with a nanometer scale depth, and its response, the load, can be obtained in the range of milli-Newton scale. From load-displacement behaviors obtained during the loading and unloading process of the indentation test, the effective elastic modulus and the hardness of the tested materials are calculated using a typical analysis method, which is suggested by Oliver and Pharr (1992).

Nanoindentation tests for a copper film and a silicon substrate

A nanocrystalline (nc) copper film and a silicon substrate were selected as testing materials. The grain size of the nc copper, measured using SEM after it had been etched using an H_2SO_4 solution, was found to be 67nm with a standard deviation of 21nm. A number of indentation tests were performed on each of the same specimen but the different position, at least 1mm apart to avoid any interactions among the indentation results. The specimens were prepared according to the following procedures. In this paper, residual stresses that arise from the high temperature and pressure are ignored:

- The copper films were diced with 10mm x 10mm and mounted on the silicon substrate.
- They were cured in a special chamber under the high temperature and pressure.
- They were polished using $0.3\,\mu m$ alumina to prepare a smooth and flat surface for indentation.

A total of 32 experiments were performed on the first (substrate-only) material system (Figure 3.3a). In the second film-substrate material system (Figure 3.3b), a total of 36 indentation tests were repeated. Two dimensionless ANNs previously trained were used to determine the in-situ material properties from the indentation experimental results. Figure 3.22 shows the 32 indentation responses of the silicon substrate-only material system. These are shown in the shaded area due to a large number of curves. Three curves in Figure 3.22 are the 2D and 3D FE simulation results along with the response from the trained dimensionless ANN. The FE simulation results show that both 2D and 3D FE models can effectively capture the loading and unloading parts of the test results. The experimental results confirm our FE models. In addition, the trained ANN with different parameters was used to fit the test results by matching the hardening value and stress limit to that used in both 2D and 3D FE simulations. This result shows that the trained ANN can be used to back-calculate in-situ material properties using only the loading part of the test results. The FE simulations show a slightly stiffer response compared to the test results for indentation depth greater than 250nm. However, they are still in the range of the deviation of the experimental results. Figure 3.23 shows the 36 indentation experimental responses of the film on the substrate system (Figure 3.3b). Again, finite element simulations were conducted to match the experiments using both 2D and 3D models. The previously trained dimensionless ANN was also used to compare with the experimental results. The 2D and 3D FE responses can equally capture the overall indentation responses. The trained ANN can effectively back-calculate the in-situ film hardening and its stress limit.

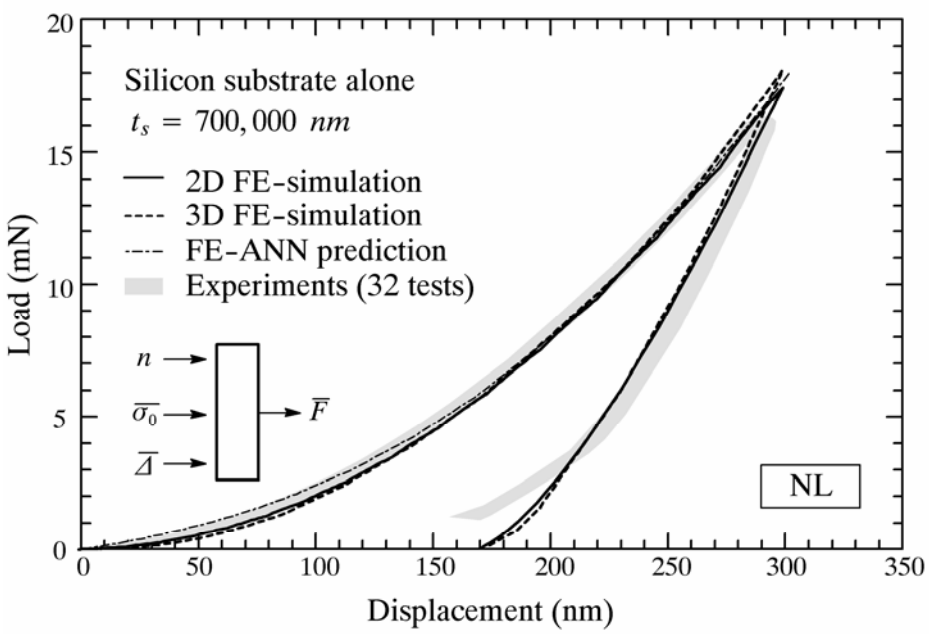

Figure 3.22 FE-ANN prediction, FE simulation, and experimental results for the silicon substrate

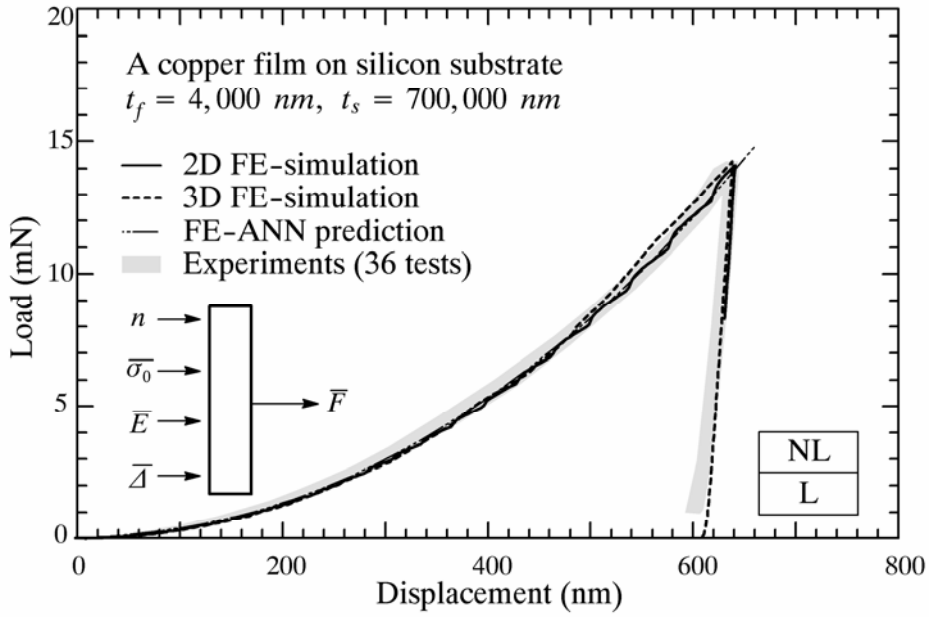

Figure 3.23 FE-ANN prediction, FE simulation, and experimental results for the nanocrystalline copper film on the silicon substrate

Table 3.1 presents the parameters that were back-calculated from the trained ANNs for the two systems by matching the ANN response to the experimental results. Here, the stress limits of the copper film, which was determined to be 0.035GPa corresponds to the yield stress of 0.11GPa from an off-set yield stress calculation method. It is interesting to note that the inverse problem results for the substrate-only system yield a hardening value of n=1.01, which is almost a linear stress-strain relation. This adds to the confidence for the inverse results from the trained ANN.

Table 3.1 Properties of the nanocrystalline copper film and the silicon substrate

	Young's modulus (GPa)	Poisson's ratio	Hardening parameter (n)	Stress limit (GPa)
Copper film	169	0.22	2.21 [(a)]	0.035 [(a)]
Silicon substrate	133	0.22	1.01 [(a)]	0.100 [(a)]

(a) Determined from the trained ANNs

Nanoindentation and tension tests for a Cu-ECAE material

The trained ANN models can be used in an inverse problem to back-calculate the uniaxial stress-strain parameters from the indentation tests. Toward that goal, material system identifications are performed for a copper film manufactured by an equal-channel angular extrusion (ECAE) process. The experimental results were obtained from reference (Bansal et al., 2005). The dimensionless ANN model trained for the substrate-only material system is used to back-calculate the material behavior (i.e., the stress-strain curve of the Cu-ECAE) from the given nanoindentation responses. Figure 3.24 shows the monotonic loading part of ANN prediction and nanoindentation experimental results for the Cu-ECAE. The experimental nanoindentation load-displacement curves are expressed as a shaded area due to the variation of the repeated tests terminated at different indentation depths ranging from 200nm to 400nm.

In order to back-calculate the in-situ stress-strain parameters, the proposed dimensionless ANN for the substrate-only system is used. A curve-fit is used to solve a computerized refined inverse problem by comparing the load-displacement curve generated from the ANN to the experimental result. A total of 10,000 comparison cases are examined with 100 different hardening parameters and 100 different dimensionless stress limits. These two parameters are equally distributed within their training ranges. The hardening parameter range is (1, 5), while the stress limit range is from 4×10^{-5} to 4×10^{-3}. Figure 3.24 shows several experiments that were performed using displacement control by Bansal et al. (2005). We have clustered these repeated tests into one shaded area (Including plotting the experimental curves) to illustrate the test variations in the repeated indentations. These differences are similar to many mechanical based materials testing, such as material variability, loading conditions, etc. The proposed ANN prediction compared to all the experimental responses was selected to match the upper bound response as shown by the solid line in Figure 3.24. This was done in order to best fit the uniaxial behavior.

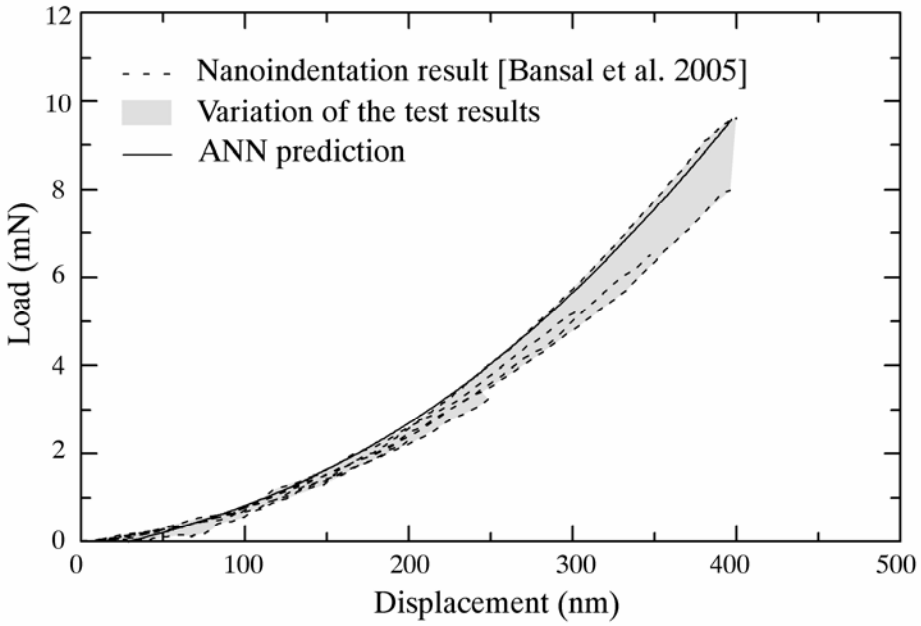

Figure 3.24 Nanoindentation load-displacement responses from the test and the ANN prediction for Cu-ECAE

Figure 3.25 shows the stress-strain curves obtained from the uniaxial tension test result performed on a dog-bone coupon by Bansal et al. (2004) for the Cu-ECAE material and from the proposed ANN back-calculation using the load-displacement curve described as a solid in Figure 3.24. The stress-strain curve identified using the proposed ANN is shown as a solid line. The stress limit and hardening parameter are determined as 400MPa and 2.74, respectively. The experimental stress-strain curve is shown as a dashed line, and its yield and ultimate stresses are 437MPa and 454MPa, respectively. It is interesting to note that in Figure 3.24 more variations in the experimental results are present at higher depths. This can be explained by the higher sensitivity of the plastic and nonlinear behavior on the variability of the spatial material nonlinear properties, i.e. from one indentation site to another. Perhaps this is a typical variability in indentations especially for relatively shallow depths (few hundreds of nanometers), where the response is in the range of continuum but the length-scale is small and local effects are more pronounced.

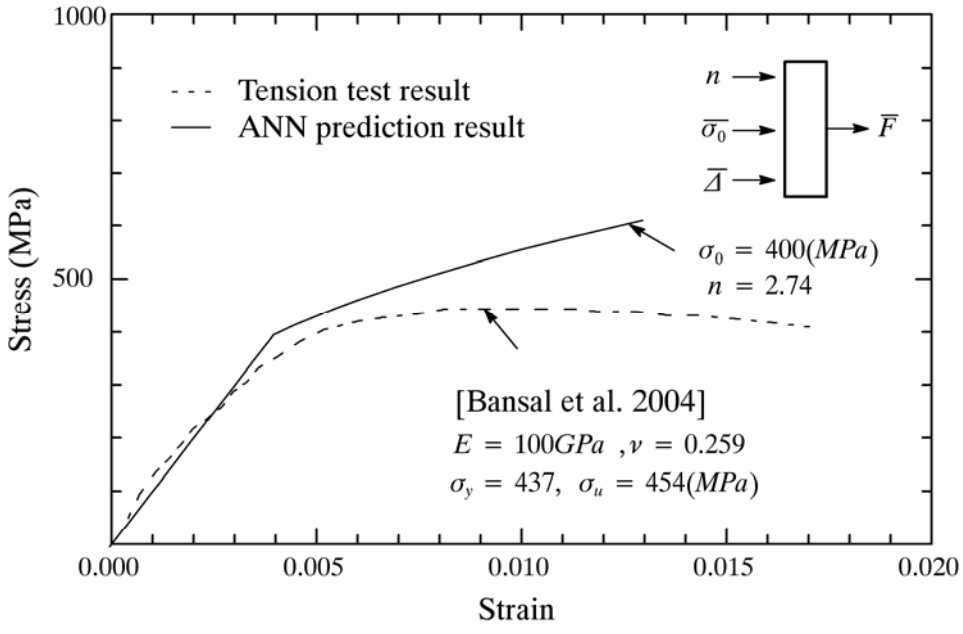

Figure 3.25 Stress-strain curves generated from the proposed ANN and the regular tension test for Cu-ECAE

The stress-strain curve obtained from the uniaxial tension test has the pronounced nonlinear behavior with a relatively small ultimate strain. Damage occurs with softening past the ultimate state. However, the predicted ANN stress-strain curve linearly increases up to the stress limit. Its slope starts to decrease past the experimental stress limit with hardening behavior. The difference in the predicted stress-strain response can be attributed to the Ramberg-Osgood model where it does not include softening and damage. The family of curves has always a positive slope beyond yield even for relatively larger hardening parameter, n. In addition, the limited range of indentation depth can be another reason. This relatively shallow indentation depth (i.e., hundreds nanometers as shown in Figure 3.25) may not be enough to characterize the full range of nonlinear stress-strain behavior in this case of inverse problem. Having said that, the predicted uniaxial stress-strain curve shows a reasonable response compared to the test results. This demonstrates the ability to use the trained dimensionless ANN model to back-calculate in-situ material behavior, such as accurate prediction of the yield point in this case while the hardening has been overestimated due to the use of Ramberg-Osgood in the FE simulations with no softening.

CHAPTER 4: Time-Dependent ANN Models for Indentation Creep Tests

For the past five years, researchers have investigated the time-effect on nanoindentation tests by considering indentation loading rate and viscosity of testing materials. Only limited number of researchers has tried to characterize the in-situ time-dependent material properties of micro- and nano-scaled materials from nanoindentation creep test result (i.e., time-displacement response) using analytical and mathematical models. However, these models are still inaccurate or inefficient to characterize in-situ time-dependent material behaviors from the experimental creep response.

This chapter presents ANN constitutive models to characterize the in-situ time-dependent material parameters from the nanoindentation creep response (i.e., time-displacement data) for micro- and nano-scaled polymeric materials. The proposed ANN models trained with nanoindentation creep FEA results can efficiently and effectively generate the creep behavior for various material properties. In order to investigate the capability of the proposed ANNs, three separate ANN models are generated with three different sets of input variables: applied load and logarithmic time; elastic modulus, Poisson's ratio, and logarithmic time; and elastic modulus, creep compliance coefficients, and logarithmic time, respectively. However, all their output is the same as indented displacement. Once the proposed ANN models are trained, their predicted results are compared to nanoindentation creep test or simulation results that were not used in the training. The trained third ANN model for different creep compliances is used to extract the elastic modulus and creep compliance parameters from creep experimental data performed on Polycarbonate coupons. The extracted creep compliance behavior is also compared to the reference data. This chapter is divided into 3 parts. The first part presents the nanoindentation FE model, creep FE simulation, and the verification with experimental creep results performed on Polyester and Polystyrene. The second part describes the proposed ANN constitutive models, and the third part deals with the characterization of the in-situ time-dependent

material properties from the experimental creep result using the proposed ANNs. Their results are also discussed.

4.1 Nanoindentation Creep Finite Element (FE) Simulations

Axisymmetric 2D FE model

This chapter presents an axisymmetric 2D FE model to perform nanoindentation creep simulation within the indentation depth ranging from 100 to 2000nm. It can be conducted using loading or displacement control on a polymeric infinite medium, which is referred to as substrate in this chapter, and the medium is considered elastic and linear viscoelastic like the typical characteristic of polymeric films. Figure 4.1 shows the geometry information of the FE model used in this chapter. The substrate is considered as a square with the enough length, so the boundary condition of the medium does not generate the localized affection on the simulation results. Each length of the FE models is determined as 20 μm, and it is composed of 2,300 axisymmetric four-node solid elements with reduced integration points, i.e. CAX4R. The FE model has the most refined meshes under the indenter tip, while it has coarser meshes away from the contact area of indenter tip. Both the refinement and the number of meshes are determined through convergence studies. The smallest size of the mesh is 20nm by 20nm. A conical indenter with an angle of 70.3 degree that provides the same projected area as Berkovich indenter is used.

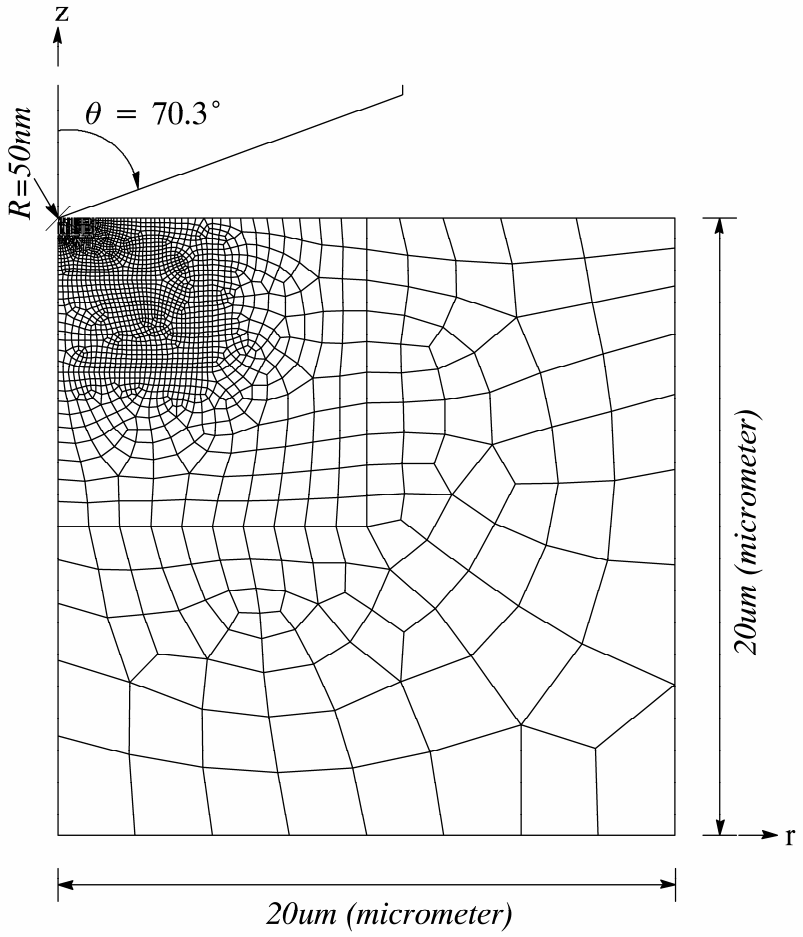

Figure 4.1 Axisymmetric 2D nanoindentation FE model

Nanoindentation creep FE simulation

All substrates are considered as polymeric materials in the nanoindentation creep FE simulation, and their typical material responses are elastic and viscoelastic. A general purpose implicit FE code, ABAQUS, is synchronized with linear viscoelasticity in order to conduct nanoindentation creep FE simulations. A simple power-law type constitutive model derived from the classic linear viscoelasticity is used as the normalized creep compliance for the time-dependent material behavior of the medium. Constitutive equations are expressed as follows:

$$s(t) = s_0(t) + \frac{1}{G_0}\int_0^{\infty} \frac{dG(\tau)}{d\tau} s_0(t-\tau)d\tau \tag{4.1}$$

$$p(t) = p_0(t) + \frac{1}{K_0}\int_0^{\infty} \frac{dK(\tau)}{d\tau} p_0(t-\tau)d\tau \tag{4.2}$$

Where $s(t)$ and $p(t)$ are the current deviatoric and hydrostatic stress vectors, respectively; $s_0(t)$ and $p_0(t)$ are the initial elastic deviatoric and hydrostatic stress vectors, respectively; G_0 is shear modulus; K_0 is bulk modulus; τ is retardation time.

Alternatively, the above equations can be reduced as one dimensional expression and described as following equation 4.3.

$$\varepsilon(t) = \int_0^t J(t-\tau)\frac{d\sigma(\tau)}{d\tau}d\tau \tag{4.3}$$

Where $J(t)$ is the creep compliance, expressed as $J(t) = J(0) + \Delta J(t)$; $\varepsilon(t)$ is the current strain; and $\frac{d\sigma(t)}{dt}$ is the loading rate. The $J(0)$ component of the creep compliance indicates elastic instantaneous material response, which can be determined as inverse of the material's elastic modulus (1/E). The $\Delta J(t)$ component is the time-dependent part, which is often expressed using simple power-law equation or Prony's series. The Prony's series representation is given as:

$$\Delta J(t) = \sum_{i=0}^{n} J_i[1 - \exp(\frac{t}{\tau_i})] \tag{4.4}$$

For linear viscoelastic isotropic materials, the creep compliance can be divided into deviatoric and hydrostatic parts, denoted by $J_s(t)$ and $J_k(t)$, respectively. They can be expressed in terms of the uniaxial creep compliance by assuming time-independent Poisson's ratio as:

$$J_s(t) = 2(1+\upsilon)J(t) \tag{4.5}$$

$$J_k(t) = 3(1-2\upsilon)J(t) \tag{4.6}$$

The deviatoric creep compliance in Equation 4.5 can be written in terms of normalized simple power law function:

$$j_s(t) = \frac{J(t)}{J_{s0}} = C \times t^n + 1 \tag{4.7}$$

Where, C and n are material parameters. Once the normalized deviatoric creep compliance has been determined, the normalized hydrostatic creep compliance can be calculated using the relationship as shown in equations 4.5 and 4.6.

Figure 4.2 shows the typical loading, creep, unloading, and relaxation parts of nanoindentation simulation results generated from the FE model developed in this study. Figures 4.2a and 4.2b show the mechanical and time-dependent responses of nanoindentation tests, respectively. Figure 4.2c shows the deformed FE meshes of the contact area according to the time variance (A: before indenting, t=0sec; B: after indenting, t=1sec; C: after creep deformation, t=2000sec; D: after unloading the applied load, t=2001sec; and E: relaxation deformation, t=4000sec). Its simulation results (i.e., deformed FE meshes corresponding to the applied load with time variance) are very understandable. These results demonstrated that the developed FE model can generate reliable nanoindentation simulation results along with the time variance. It is interesting to mention that the substrate still has its deformation even though the applied load has been removed and released during relaxation part. This may be caused by the insufficient relaxation time. If an infinite relaxation time is given, this deformation will be vanished due to its elastic behavior. In this study,

we are using only the creep part of whole FE simulations, i.e. from B to C. In Material parameters used in this demonstration are as follows: E=3691MPa, v=0.37, C=2, and n=0.3.

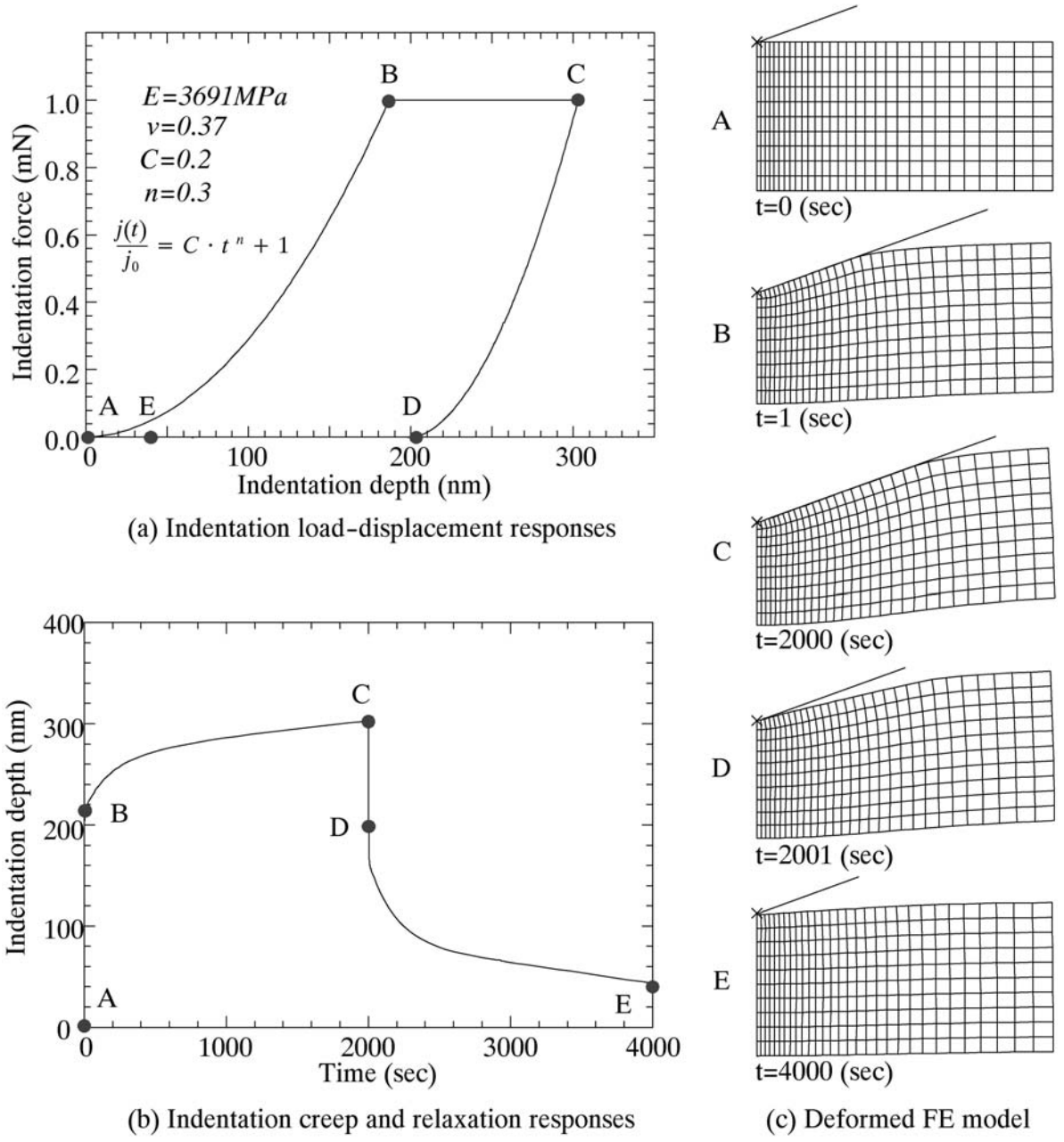

Figure 4.2 Indentation FE simulation results along with time variance: (a) Indentation load-displacement responses; (b) Indentation creep and relaxation responses; and (c) Deformed FE model

Experimental nanoindentation creep tests for Polyester and Polystyrene

In order to examine the capability of the developed FE model to generate appropriate nanoindentation creep responses, we compared our FE simulation results to experimental results performed on Polyester and Polystyrene substrates with the Berkovich indenter. They were obtained from reference (i.e, Yang et al., 2004). Figure 4.3 shows the experimental nanoindentation creep response and FE simulation results for Polystyrene. This FE simulation response was generated by visually fitting to the experimental response, so it may not be the best nanoindentation creep response that this FE model can generate. However, the generated FEA result shows a good agreement with the experimental data. Material parameters used in the FE simulation are E=2300MPa, v=0.35, C=0.6, and n=0.3. Similarly, another experimental result for Polyester was compared with the FE simulation as shown in Figure 4.4. Based on this comparison result, the FE model is used to generate appropriate nanoindentation creep responses for the ANN models proposed in this study.

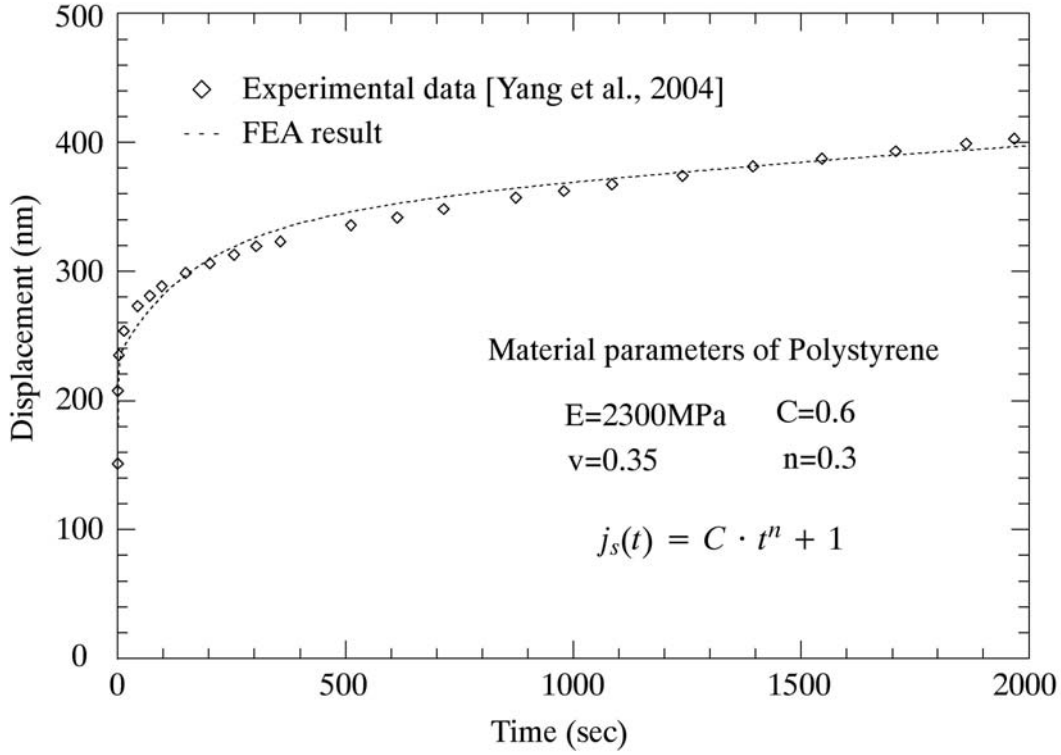

Figure 4.3 Experimental indentation creep test and FE simulation results for Polystyrene

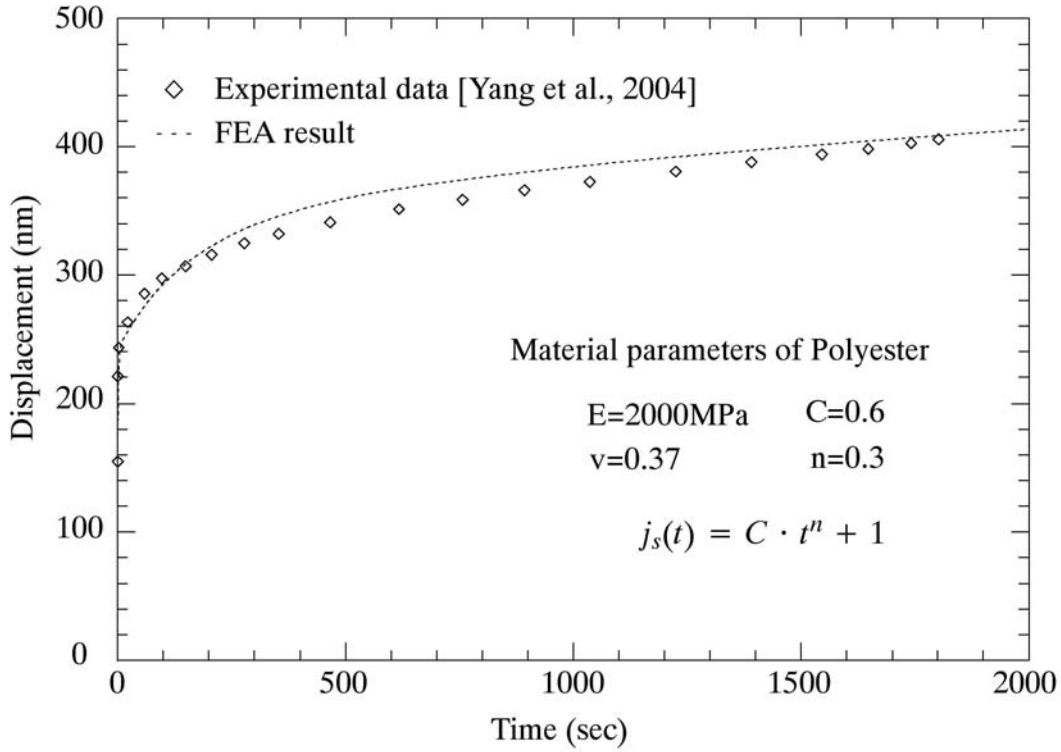

Figure 4.4 Experimental indentation creep test and FE simulation results for Polyester

4.2 Proposed ANN Models for FE Creep Nanoindentation of Polymers

In order to demonstrate and examine the proposed ANN approach to generate nanoindentation creep responses, three ANN models are developed for different indentation time, mechanical properties, and creep compliances as illustrated in Figure 4.5. The first ANN model includes a magnitude of the applied load and logarithmic holding time as its input variables and the corresponding creep displacement as an output variable. The second ANN model is composed of three inputs, which are modulus, Poisson's ratio, and logarithmic holding time, and one output, which is the corresponding creep displacement. Finally, the third ANN consists of modulus and creep compliance parameters as its input variables. In order to train the proposed ANN models, a large set of training data were generated from the developed FE model with different loads, substrate's mechanical properties, and creep compliances. The FE simulation includes only the creep part (B-C)

of nanoindentation creep simulations, which are shown in Figure 2. The starting point of the creep part (i.e., B) is generated by pushing the conical indenter into the substrate with a quasi-static ramp loading for duration of 1 second, and the creep response, from B to C, are generated by holding the applied load for 1999 seconds. The training data uses only the nanoindentation creep responses obtained from 1 to 2000 seconds, i.e., the creep part. Once the training process has been completed, the trained ANNs are examined by comparing the creep responses from the trained ANNs and the ones from the FE results that were not used during the training process.

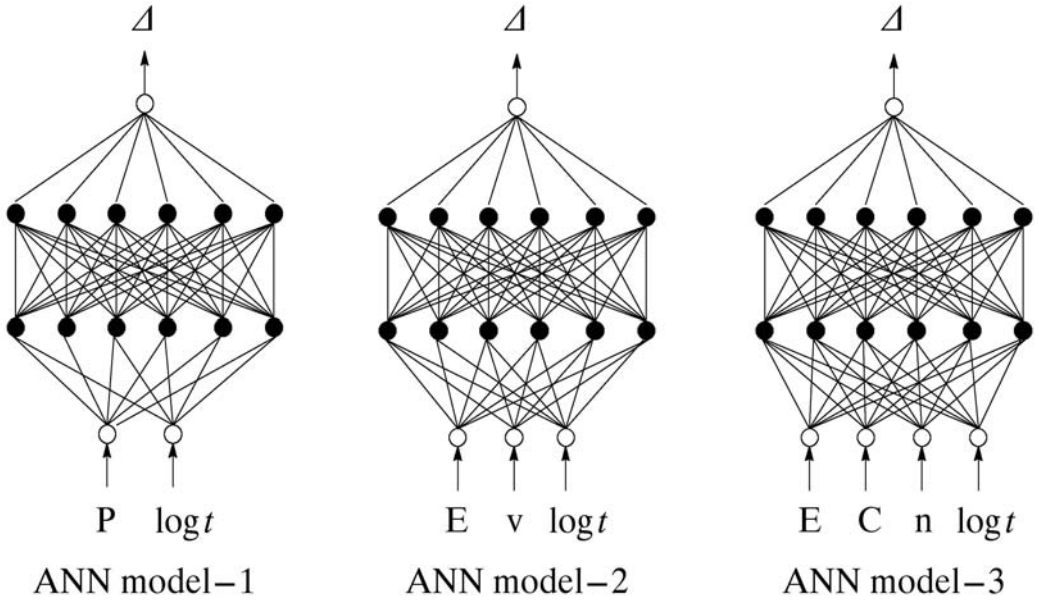

Figure 4.5 Proposed ANN models for different loading, material properties, and creep compliance

The first ANN model includes applied load and logarithmic holding time as input variables, while the corresponding displacement is the output variable. In order to train the first ANN model, a total of six different FE simulation results were generated for the following loads: 0.1, 0.5, 1.0, 2.0, 3.0, and 5.0mN. The material parameters used for these FE simulations were considered constant: E=3691 MPa, ν=0.35, C=0.2, and n=0.3. Once the training has been completed, nanoindentation creep responses for loads: 0.3, 1.5, and 4.0mN, generated from the trained ANN were compared to

the ones from the FE simulation. Figure 4.6 shows the FE and ANN responses, indicated by the solid and dashed lines, respectively. It can be seen that the trained ANN can generate creep responses for different loading cases. Slight deviations are observed between the FE and ANN responses when the applied load is relatively small, i.e., P=0.1, 0.3, and 0.5mN. This is because the trained ANN is less sensitive due to the relatively small loads compared to the other loads used in this training. However, this problem can be solved by adding more training cases (i.e., more than 520 data sets, used in the training of the first ANN model) or increasing the sensitivity of the variables by using more strict error tolerance, less than 0.1% used in this training. It was demonstrated that the trained ANN can generate nanoindentation creep response for various loads.

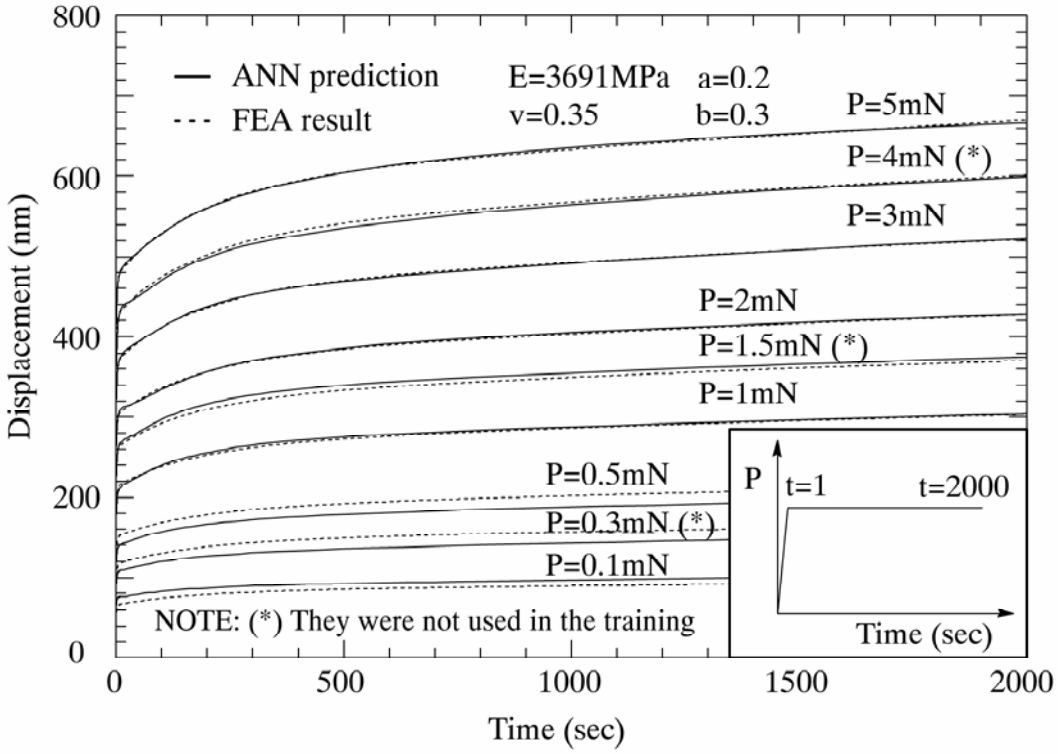

Figure 4.6 Indentation creep simulation responses generated from the FEA and ANN trained for different indentation loading (ANN model-1)

Another ANN model is proposed to demonstrate its capability in generating nanoindentation creep responses for different elastic material properties. For this purpose, elastic modulus, Poisson's ratio, and logarithmic holding time is chosen as input variables, while the corresponding displacement is considered as output variables. In order to generate the training data, a total of 20 FE simulations are conducted under five different elastic moduli: 1, 2, 3, 4, and 5GPa and four different Poisson's ratios: 0.1, 0.2, 0.3, and 0.4. The other two material parameters (C=0.2 and n=0.3) are held constant, as well as the applied load of 1mN. It is noted that the model deals with linear viscoelasticity, in which the load's magnitude will not affect the material responses. Figure 4.7 shows nanoindentation creep responses generated from the trained ANN and FE simulations for the various combinations of material parameters used in the training process. The trained ANN produces similar responses compared to the ones of the FE simulations. It is observed that nanoindentaiton creep responses decrease as Poisson's ratio and modulus increases. However, the variation rate of nanoindentation creep response is increasing as the Poisson's ratio is increasing. Furthermore, the trained ANN is used to generate responses for 12 different combinations of material parameters that are not used in the training process, i.e. four moduli: 1.5, 2.5, 3.5, and 4.5GPa and three Poisson's ratios: 0.15, 0.25, and 0.35. Figure 4.8 demonstrates that the trained ANN can generate appropriate nanoindentation creep responses for different combinations of material parameters, even though these parameters are not used in the training.

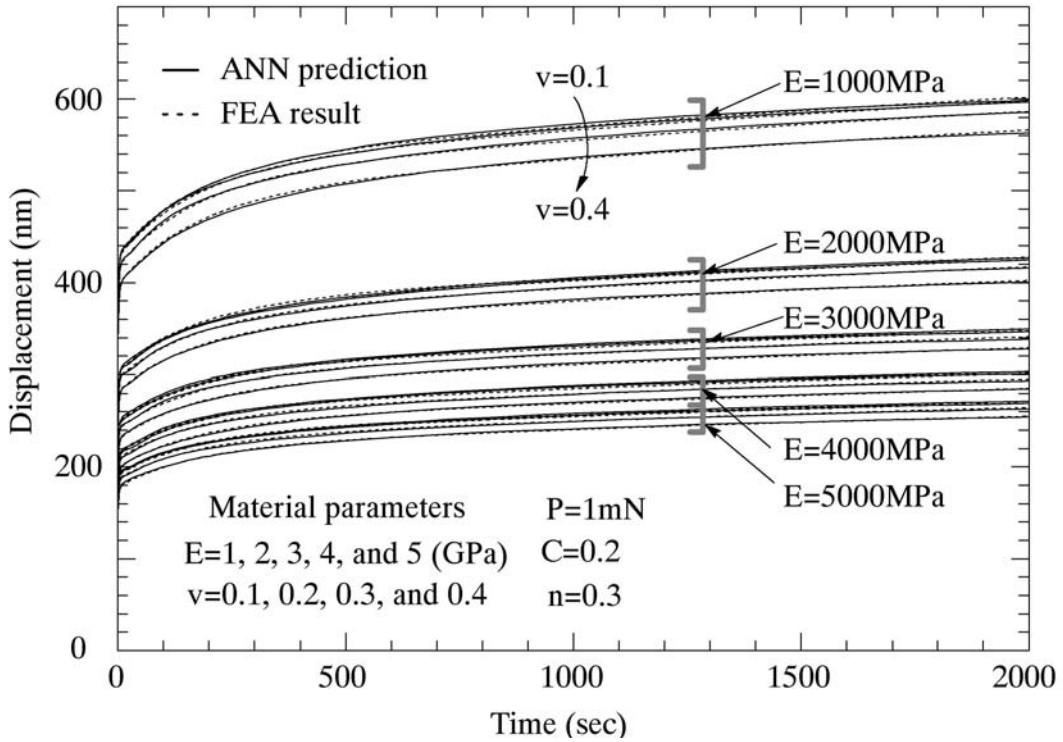

Figure 4.7 Indentation creep simulation responses generated from the FEA and ANN trained for different material properties (ANN model-1)

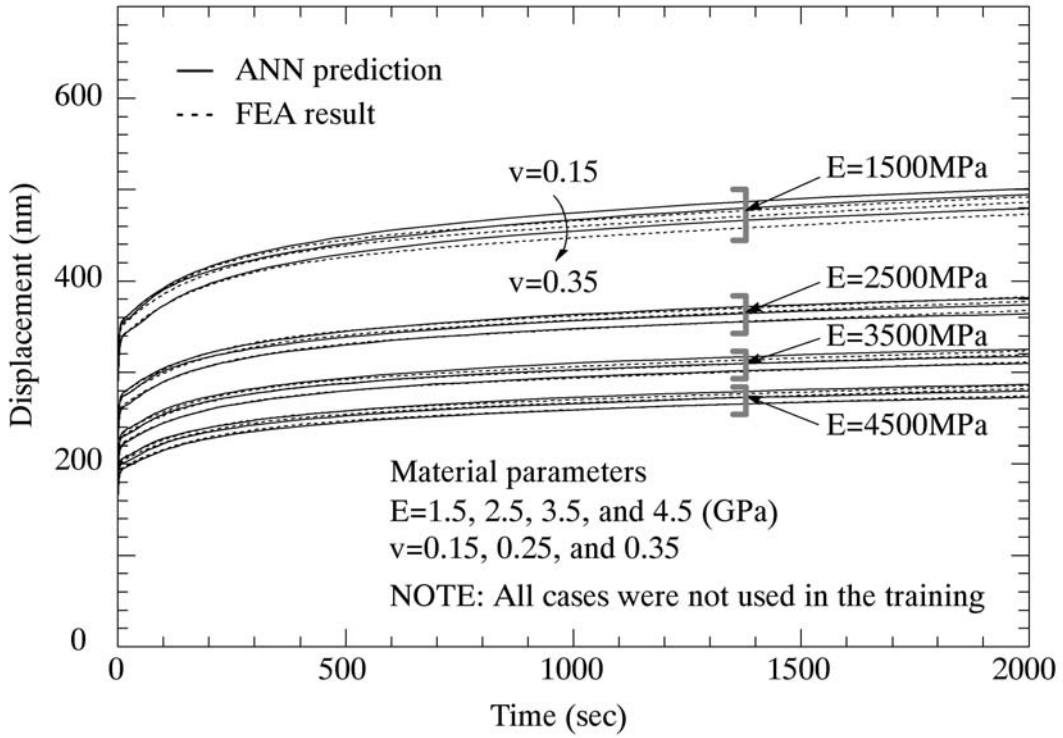

Figure 4.8 Indentation creep simulation responses generated from the FEA and ANN model-2 for different material properties that were not used in the training

The third and last ANN model is proposed to examine the prediction capability to generate creep responses for different mechanical and time-dependent materials. This ANN model has modulus(E), logarithmic time($\log t$), coefficient(a), and exponent(b) of the normalized creep compliance as its input variables, while the corresponding displacement(Δ) is its output. In order to train the proposed ANN, a total of one hundred FE simulations are conducted for four different moduli: 1, 1.5, 2, and 3GPa, five different creep compliance coefficients: 0.1, 0.2, 0.3, 0.4, and 0.5, and five different creep exponents: 0.1, 0.15, 0.2, 0.25, and 0.3. The results from the FE simulations were used to train the proposed ANN and examine the capability of the ANN. Figure 4.9 shows the nanoindentation creep responses generated from the FEA and trained ANN for different creep compliance coefficients: C=0.1, 0.2, 0.3, 0.4, and 0.5; and constant material parameters: E=1500MPa, v=0.35, and n=0.3. The FEA and ANN results are described as dashed and solid lines, respectively. Both results show higher displacement responses when the creep compliance coefficient, C, is small. Identical creep responses from the trained ANN and FE simulation are shown. The trained ANN is also examined by varying creep compliance exponents, n. Figure 4.10 shows the FEA and ANN results for different exponents n=0.1, 0.15, 0.2, 0.25, and 0.3. Smaller exponents generated higher displacement responses in both the FE and ANN simulation results. This examination demonstrates that the proposed ANN can generate appropriate nanoindentation creep responses for different time-dependent material properties.

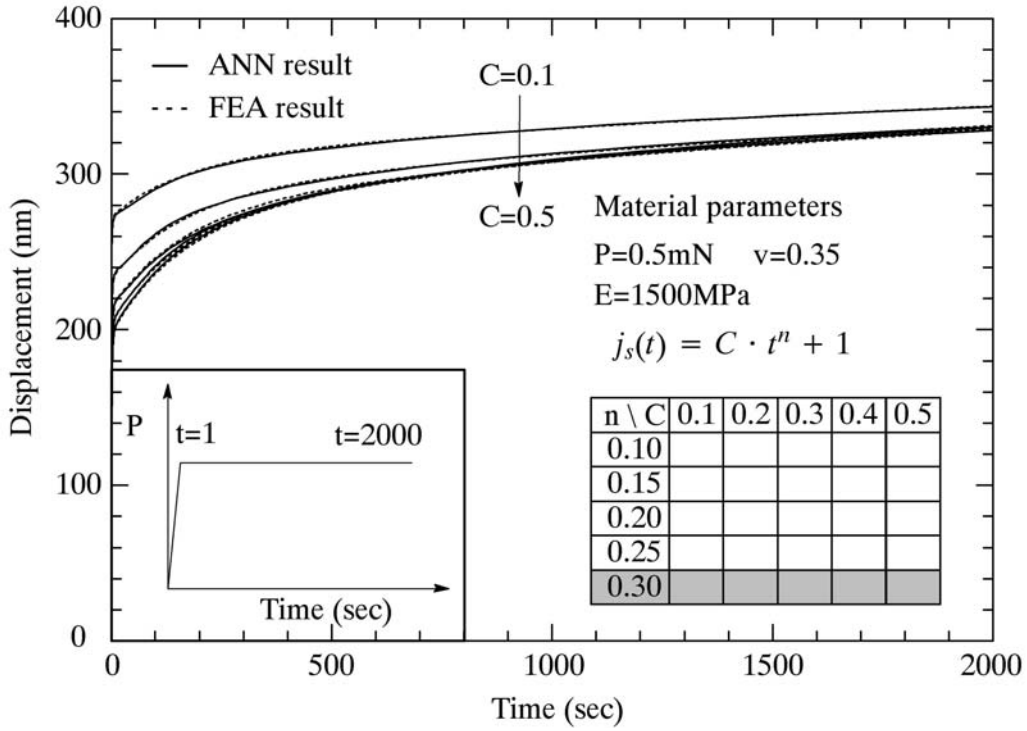

n \ C	0.1	0.2	0.3	0.4	0.5
0.10					
0.15					
0.20					
0.25					
0.30					

Figure 4.9 Indentation creep simulation responses generated from the trained ANN (i.e., ANN model-3) and FEA for different creep compliance coefficients, i.e. C=0.1, 0.2, 0.3, 0.4, and 0.5

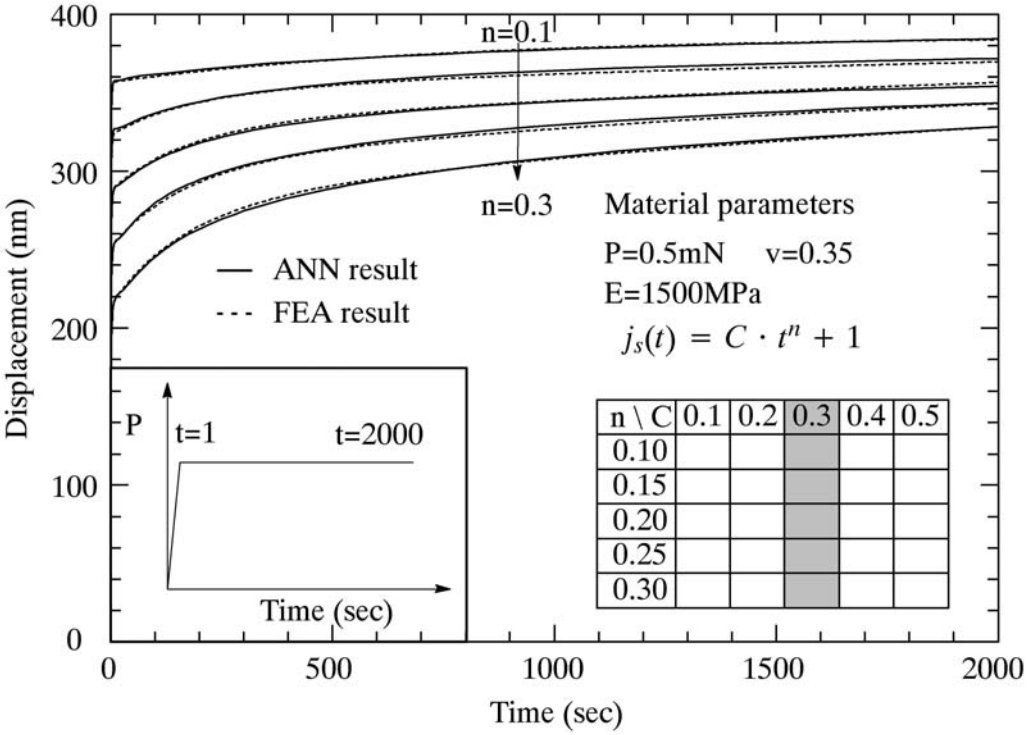

n \ C	0.1	0.2	0.3	0.4	0.5
0.10					
0.15					
0.20					
0.25					
0.30					

Figure 4.10 Indentation creep simulation responses generated from the trained ANN (i.e., ANN model-3) and FEA for different creep compliance exponents, i.e. n=0.1, 0.15, 0.2, 0.25, and 0.3

Based on previous parametric studies, the trained ANN is now performed for different creep compliances that were not used in the training process. A total of 16 cases with combinations of four of each creep compliance coefficient, C: 0.15, 0.25, 0.35, and 0.45 and exponent, n: 0.125, 0.175, 0.225, and 0.275 were generated. Figure 4.11 shows the ANN prediction and FE results with varying coefficient, C, while the exponent b is held constant as 0.225. Figure 4.12 also shows the ANN prediction and FE results for various exponents under a constant coefficient of 0.45. The ANN predictions show good agreement with the ones of the FE. Figure 4.13 shows the ANN prediction and FE results for different moduli, while all other material parameters are held constant. Material parameters that were not used in the training process were marked as asterisks (E=1.25, 1.75, and 2.5GPa). It was demonstrated that the trained ANN model-3 can generate accurate nanoindentation creep responses for different moduli and creep compliances.

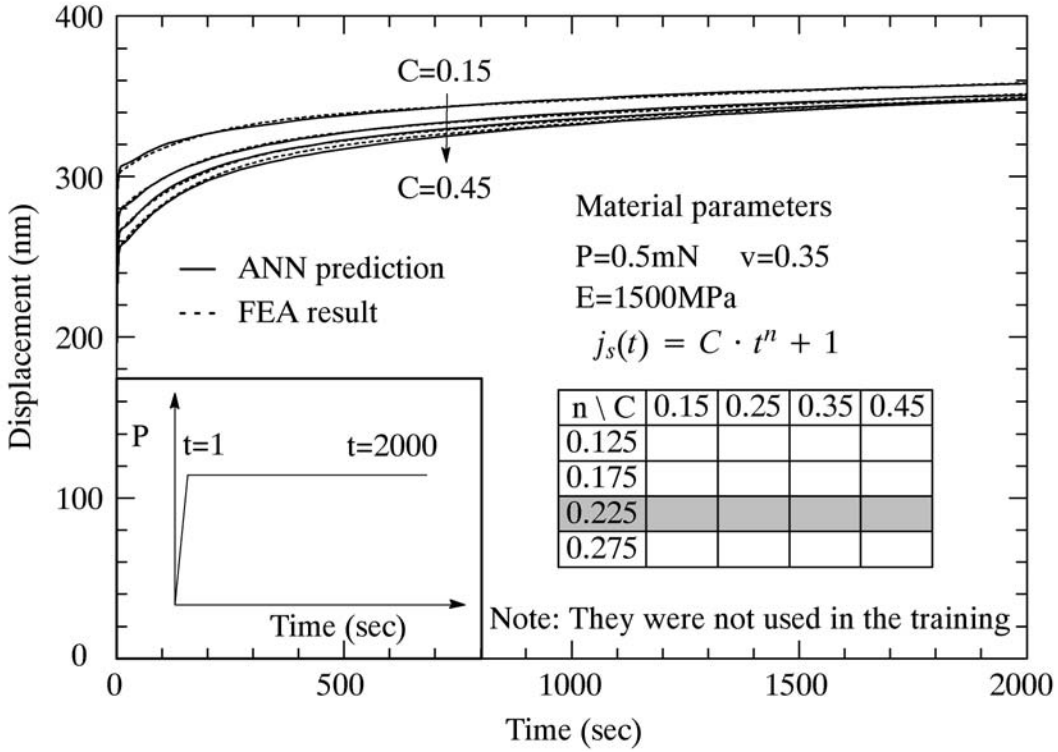

Figure 4.11 Indentation creep simulation responses generated from the FEA and predicted by trained ANN (i.e., ANN model-3) for different creep compliance coefficients (i.e., C=0.15, 0.25, 0.35, and 0.45) that were not used in the training process

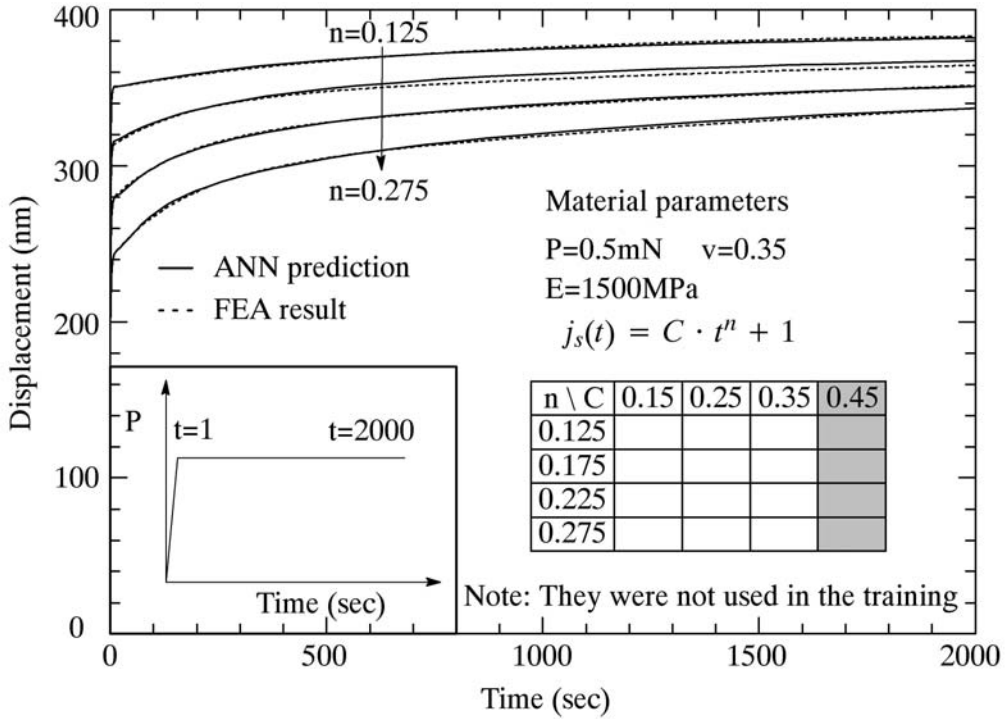

n \ C	0.15	0.25	0.35	0.45
0.125				
0.175				
0.225				
0.275				

Figure 4.12 Indentation creep simulation responses generated from the FEA and predicted by trained ANN (i.e., ANN model-3) for different creep compliance exponents (i.e., n=0.125, 0.175, 0.225, and 0.275) that were not used in the training process

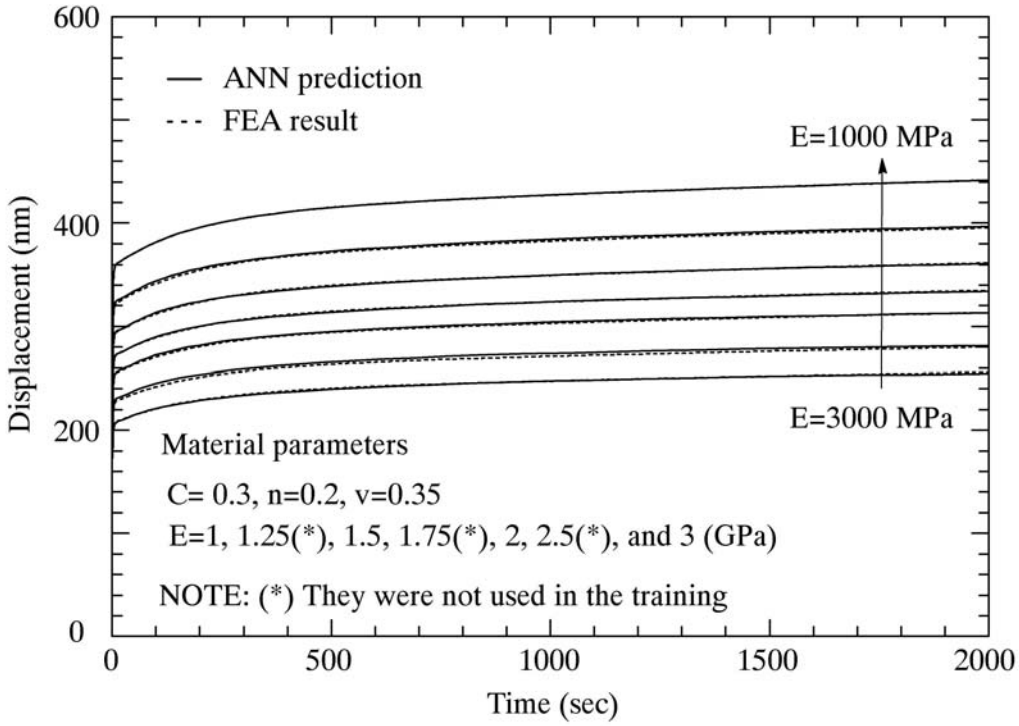

Figure 4.13 Indentation creep simulation responses generated from the FEA and trained ANN for different elastic moduli that were both used and not used in the training process

4.3 Experimental Verifications

The proposed ANNs can efficiently and effectively characterize the in-situ time-dependent material properties from the nanoindentation creep test result. This material characterization problem is often called as "inverse problem". In this part, the proposed ANN model is used to extract the in-situ elastic modulus and creep compliance parameters that can accurately generate nanoindentation creep responses. For this purpose, creep compliances of polycarbonate obtained from the nanoindentation creep tests (Yang et al., 2004) are used to characterize the material properties and verify the ANN predictions. The optimum solution within the feasible region is determined by comparing the ANN predictions for 80,000 different material cases (i.e., combined with different elastic moduli and creep compliance parameters evenly distributed in the training ranges) to the experimental nanoindentation creep results. A specific material case including elastic modulus, coefficient, and creep exponent of 1.5GPa, 0.14, and 0.3, respectively, provides the closest ANN predictions to the given experimental results. Figure 4.14 shows the comparisons of creep displacements obtained from the nanoindentation tests and the ANN simulations during the training process. The training process is complete when the creep response for 2000 second periods from the ANN matches the experimental data. The calibrated material parameters are used to determine the elastic modulus and creep compliance, $J(t)$, of Polycarbonate. The calibrated elastic modulus of Polycarbonate (i.e., 1.5GPa) is comparable to the one from the experimental tests, which is 1.52GPa, as reported by Yang et al. (2004). Figure 4.15 shows the normalized creep compliance responses obtained from Yang et al. (2004) and the proposed ANN model. We characterized the material modulus and creep compliance from the experimental nanoindentation creep response using the trained ANN with and without the known elastic modulus, i.e. 1.52GPa. The predicted creep compliance coefficient and exponent with the knowledge of the available modulus are 0.135 and 0.3, respectively. Without using the known elastic modulus, the proposed ANN produced a creep compliance coefficient of 0.14 and an elastic modulus of 1.5GPa. The solid line describes the ANN

characterization result without prior information of the elastic modulus of 1.52GPa, while the dashed line shows the ANN characterization using the known elastic modulus. Both ANN characterization results show similar and accurate creep compliances compared to the experimental data. This shows the effectiveness of the proposed ANN in characterizing material properties.

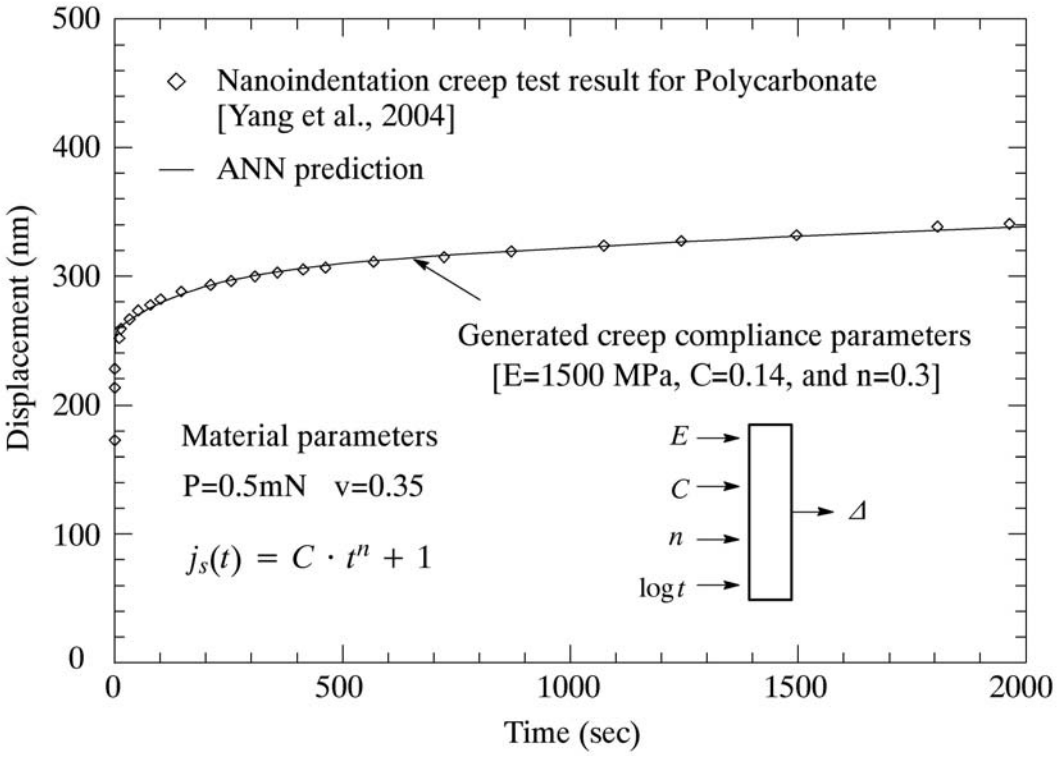

Figure 4.14 Experimental nanoindentation creep test, nanoindentation creep responses predicted from the proposed ANN, and its characterization results for a Polycarbonate medium

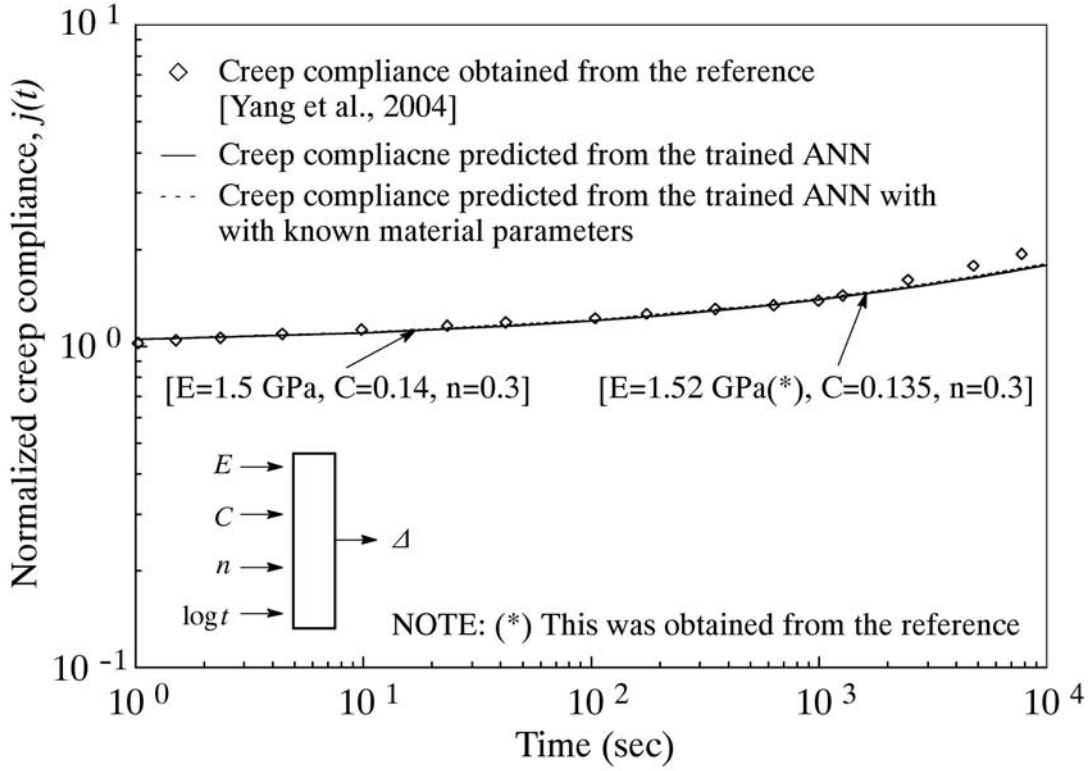

Figure 4.15 Normalized creep compliance extracted from the nanoindentation creep test using the proposed ANN and creep compliance data obtained from the reference for a Polycarbonate medium

CHAPTER 5: Nonlinear Multi-Axial ANN Models for FRP Composites

Many researchers have proposed theoretical, empirical, and analytical models to generate the complex nonlinear material behaviors of various composites at macro- and micro-scales. These models can generate effective material responses at the macro-scale. However, they are ineffective or inaccurate to generate full-field nonlinear material behaviors of fiber-reinforced composite materials. Therefore, there is a need of more accurate and general constitutive models that can generate full-scale complex behaviors as composite materials are increasingly used.

This chapter presents new ANN constitutive models to generate nonlinear and multi-axial stress-strain behaviors of fiber-reinforce composite materials. The proposed ANN models are trained with experimental data instead of simulated FEA results. The ability of the trained ANN models to predict material response is examined directly and through FEA of a notched composite plate. The integration result of FE-ANN is also examined with coupon testing of thick-section pultruded fiber-reinforced polymeric (FRP) E-glass/polyester material. This chapter is divided into two major parts. The first part presents the modeling and training of the proposed ANN constitutive models for FRP composites, while the second part deals with the integration of the trained ANN models with FE software for the nonlinear analysis of composite structures and the experimental verification. In the first part, four different ANN models with two different output types (i.e., vector and scalar outputs) and two different forms of training data (i.e., total and inelastic parts of training data) are generated. The proposed ANN models are trained with experimental data obtained from off-axis tension/compression and pure shear (Arcan) tests results. These tests with unidirectional coupons cannot produce tension-compression (axial-transverse) and compression-tension stress or strain paths. Thus, in order to complete multi-axial stress-strain paths, it is assumed that a tension-tension mode is symmetric to a compression-tension mode, and vice versa. In the second part, the trained ANN

models are integrated with FE software as a user-defined material module for a notched composite plate. The simulated FE-ANN result (i.e., normalized load-displacement response) is compared with coupon testing results measured by an extensometer attached at testing coupon of thick-section pultruded FRP E-glass/polyester material. Their results are discussed

5.1 Proposed ANN Constitutive Models

The proposed ANN material models are illustrated in Figure 5.1. It describes a state of plane stress for a layer or effective state in multiple orthotropic layers. The objective of the trained ANN is to generate multi-axial stress-strain relations. This can be achieved in several ways by using different ANN structures, e.g. type of input and outputs, incremental, or total variables. In this chapter, a general four-layer feed-forward ANN structure is used. The four layers consist of one input layer, two feed-forward hidden layers, and one output layer. Figure 5.2 shows a schematic drawing of different ANN structures generated in this chapter. Four different ANNs are generated for different ANN structures and different training data types, i.e. total and inelastic strains. They all have different output variables, while they have the same input, i.e. three in-plane stress components. These ANNs are classified based on their scalar or vector outputs and using total or inelastic strains.

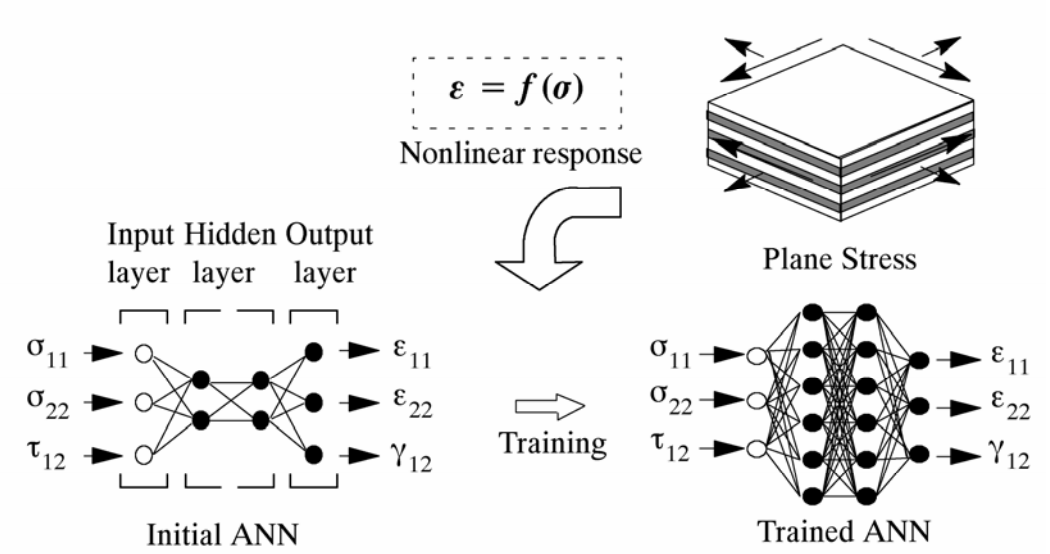

Figure 5.1 Schematic drawing of a typical feed-forward 4-layer ANN structure for plane stress non-linear material models

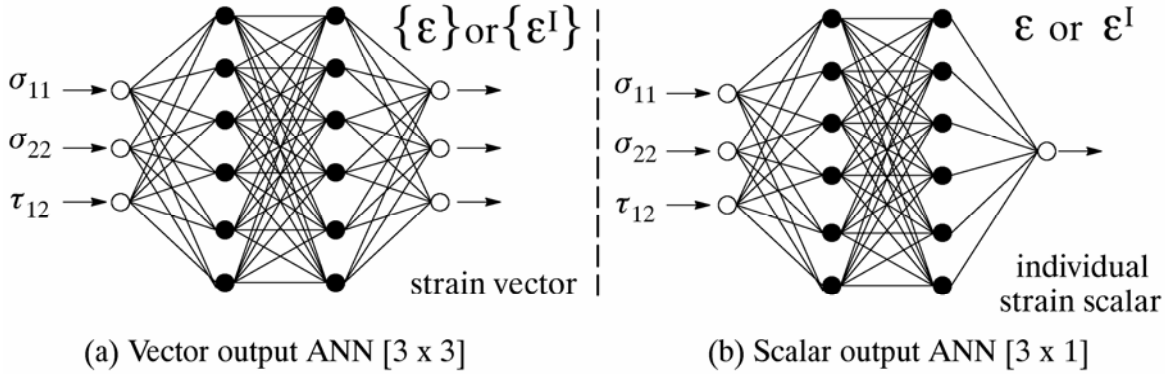

Figure 5.2 Schematic drawing of two ANN general models using total and/or inelastic strain. The second approach in (b) is to generate ANNs for each individual output variable

The training process of these ANNs can be carried out using a relatively large set of input and output data. The ANN structure is initially composed of a small number of neurons in the two hidden layers, but the training process ends up with relatively large number of neurons. The training algorithm developed in this chapter allows adding neurons in the hidden layers at specified intervals until the trained ANNs can produce satisfactory results. Figure 5.2 also illustrates the adaptive nature

during the ANN training. The developed software relies on the conjugate gradient method to minimize the total error and find the internal connection weights, e.g. Wasserman (1989). Four different combination of ANN models used in this chapter are as shown in Table 5.2.

5.2 Material System of Pultruded FRP Composites

Figure 5.3 shows a typical cross section of fiber-reinforced polymeric (FRP) composites. The pultruded FRP composites usually have relatively low fiber volume fraction (FVF) and thick sections (e.g., from 0.25 to 1in). Thick-section composites can be composed of different layers by repeated through the thickness, e.g., unidirectional roving and continuous filament mat (CFM) layers. They usually exhibit highly nonlinear material behaviors (e.g., nonlinear multi-axial stress-strain responses) because of low FVF, large thickness, and multi-different layers. In addition, the nonlinearity can be enhanced by other factors introduced during manufacturing, e.g., void, fiber breaking, and matrix failure.

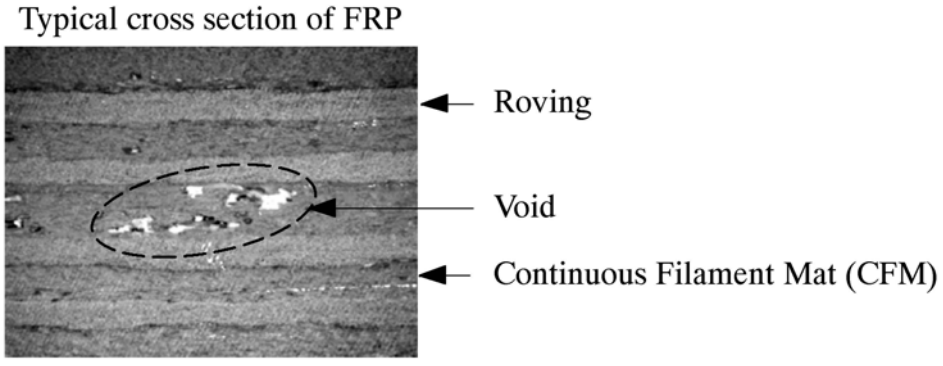

Figure 5.3 Typical cross section of pultruded FRP composites.

5.3 Experimental Training Data of the Proposed ANN Models

Training data for the proposed ANNs were collected from off-axis compression and tension tests performed with coupons cut from a monolithic composite plate manufactured by pultrusion process as shown in Figure 5.4. Haj-Ali and Kilic (2002) used similar tests to calibrate micro-mechanical models for this material. In addition to the off-axis tests, limited axial-shear stress-strain relations were generated using a modified Arcan testing fixture developed by El-Hajjar and Haj-Ali (2004). All in-plane stress-strain data sets of (σ_{11}, σ_{22}, τ_{12}) were collected up to ultimate failure state using rosette strain gages (0°, 45°, and 90° strain directions) installed at the center of each coupon and aligned with the loading axis. The stress and strain test data is usually in the global coupon system. The test data is transformed in the local material system (along with the pultrusion direction) using two separate in-plane stress and strain transformations. The local transformed stress and strain vectors are coupled for different loading levels to train the proposed ANN models that can generate and span all continuous paths of multi-axial stress-strain behaviors. The inelastic strain data needed for two of the ANNs was generated by subtracting the linear strain parts calculated using the orthotropic compliances of the material from the measured total strains. The compliance properties used in the later calculations for the inelastic strains were reported by El-Hajjar and Haj-Ali (2004) and shown in Table 5.1. The overall FVF averaged for the entire section is 0.34.

Table 5.1 Material properties of FRP composites

Unit	E11	E22	G12	v12
MPa (ksi)	18810 (2730)	11300 (1640)	3583 (520)	0.285

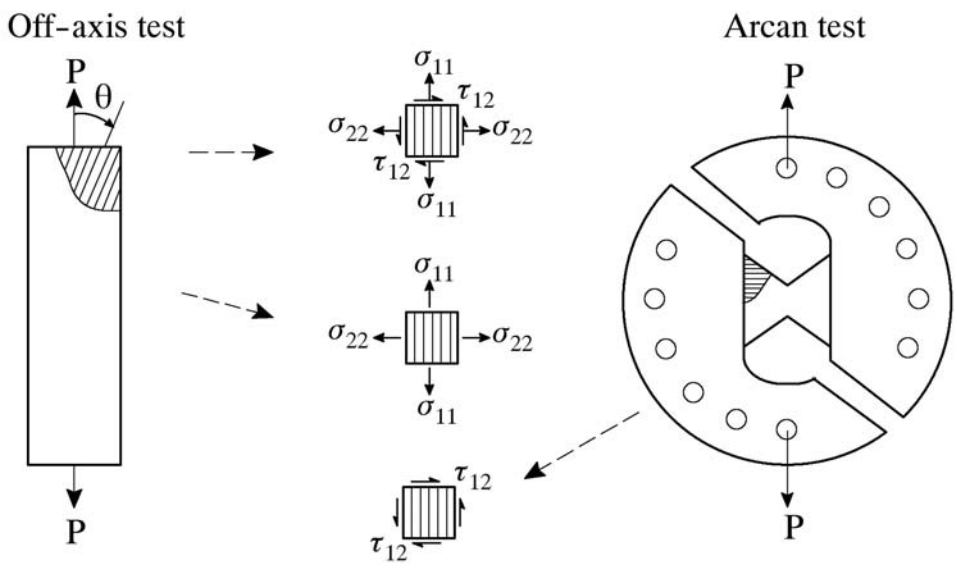

Figure 5.4 Off-axis and Arcan bi-axial coupon tests performed to generate multi-axial stress-strain data needed for the ANN training

Figure 5.5 shows the plane formed by the axial and transverse stress paths. The lines drawn in the different quadrants illustrate the experimental applied stress path and at what point it reached its ultimate failure filled circle. These stresses are all in the local material direction. The off-axis tension and compression tests produced tension-tension and compression-compression uniaxial and transverse stresses in addition to shear. The modified Arcan test, El-Hajjar and Haj-Ali (2004), was used in this chapter for pure shear mode. No tests were performed for the mixed tension-compression and compression-tension cases. These cannot be generated from the off-axis tests and may need a special multi-axial testing apparatus, which was not available. This testing limitation is overcome by using the fact that the axial stiffness is larger than the transverse. We can assume that the total strain in the tension-tension case is the same in magnitude to that of the compression tension case. This assumption can also be applied by equating the strain magnitudes of the compression-compression cases to the tension-compression strains as illustrated in Figure 5.5. Figures 5.6 and 5.7 show the axial and transverse stress paths combined with the pure shear case obtained from the modified Arcan test.

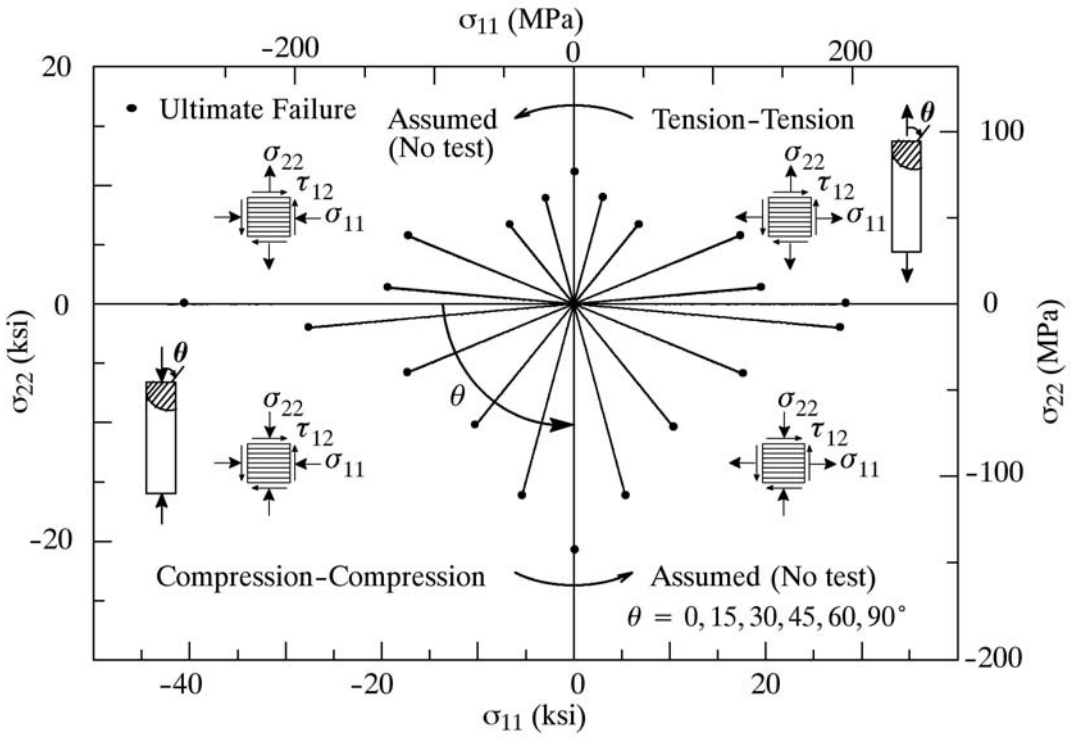

Figure 5.5 Axial and transverse stress paths (σ_{11} and σ_{22})

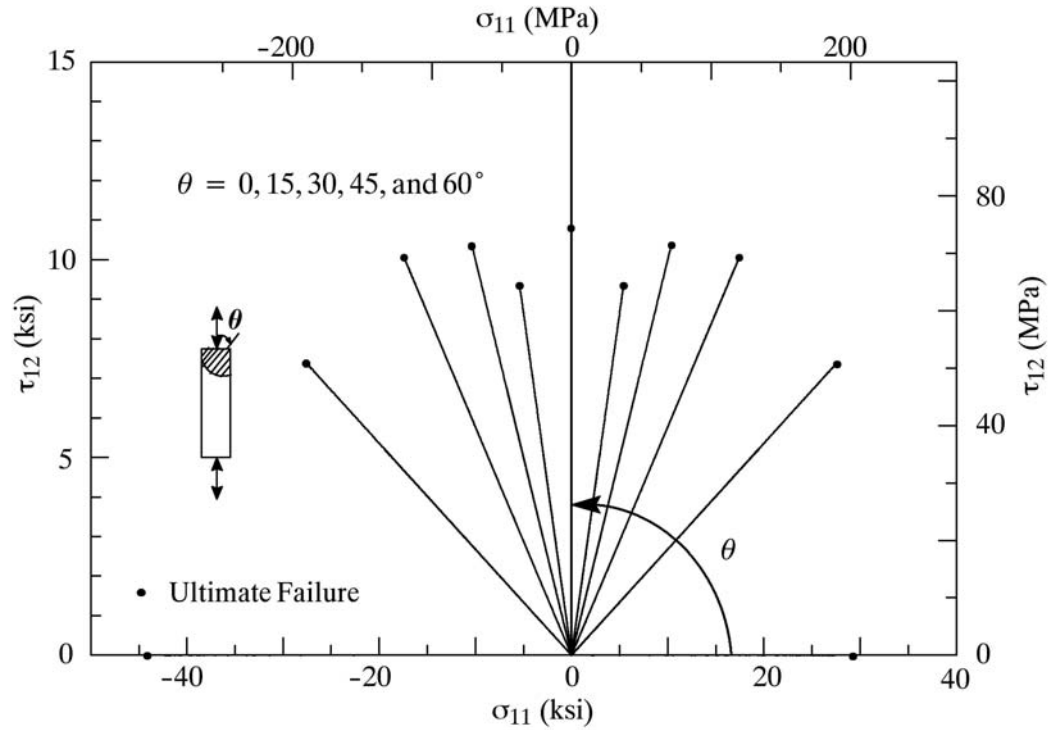

Figure 5.6 Axial and shear stress paths (σ_{11} and τ_{12}) from off-axis tests; (The pure shear case was obtained from the modified Arcan test.)

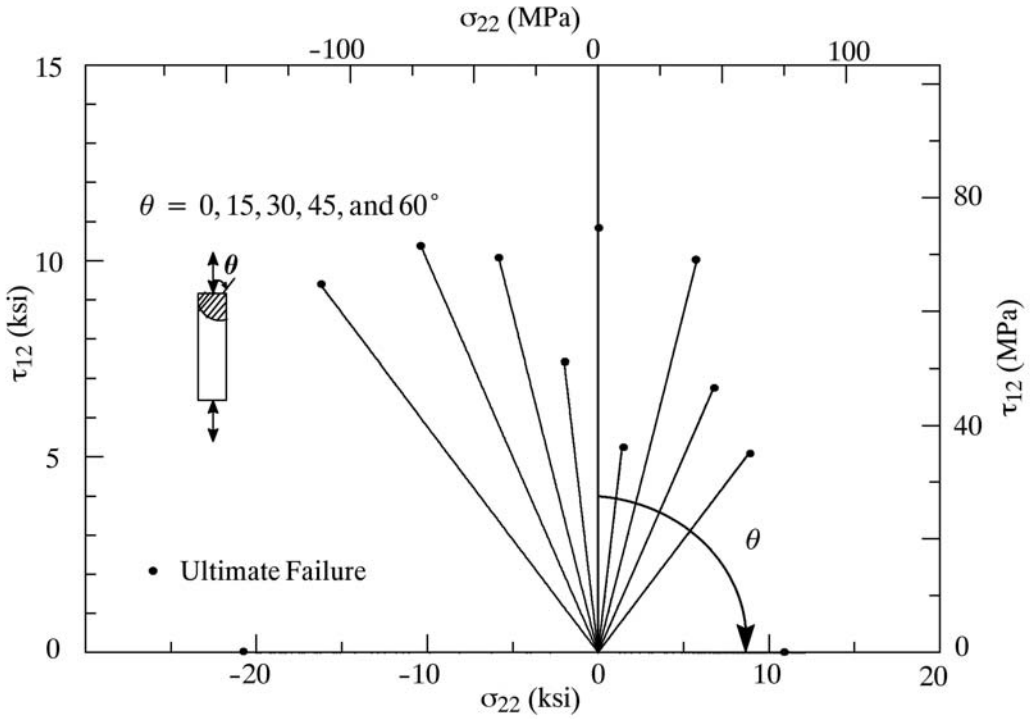

Figure 5.7 Transverse and shear stress paths (σ_{22} and τ_{12}) from off-axis tests (The pure shear case was obtained from the modified Arcan test.)

5.4 Training Results

Training was conducted for a total of eight ANNs. Two ANNs were trained for the vector-type ANN cases, while the other six ANNs were trained for scalar-type ANN cases (i.e., cases 3 and 4). Figures 5.8 and 5.9 show the calculated total error (i.e., cost function) during training process for eight ANN models. All ANN models had ten neurons initially in their two hidden layers. However, their neurons were added if the error does not decrease below a specific tolerance after a relatively large number of training cycles, i.e. epoch. These figures show a relatively small error for the ANNs and a stable convergence as the ANNs grow in size. In the cases of scalar-type ANNs, cases 3 and 4, the total error is comparatively smaller than that of vector-type ANNs, cases 1 and 2. This is expected since the ANNs are less constrained in the cases 3 and 4, and a one function with three variables was trained. The size and type of the ANNs generated in this chapter are summarized in Table 5.2. The range of final ANN is roughly around 26 neurons for the data set used (20,000 vectors) and for a similar specified global training error criterion (0.5%). These ANN models were trained for 3 to 5 days using SGI Origin 200 UNIX server.

Table 5.2 Training cases for different ANN structures

	ANN output	Hidden layer number	Initial neuron Number	Final neuron Number
Case 1	vector / total	2	10	29
Case 2	vector / inelastic	2	10	25
Case 3	scalar / total	2	(10, 10, 10)	(26, 25, 27)
Case 4	scalar / inelastic	2	(10, 10, 10)	(24, 23, 25)

*Note that there are three ANNs for the single variable output in cases 3 and 4.

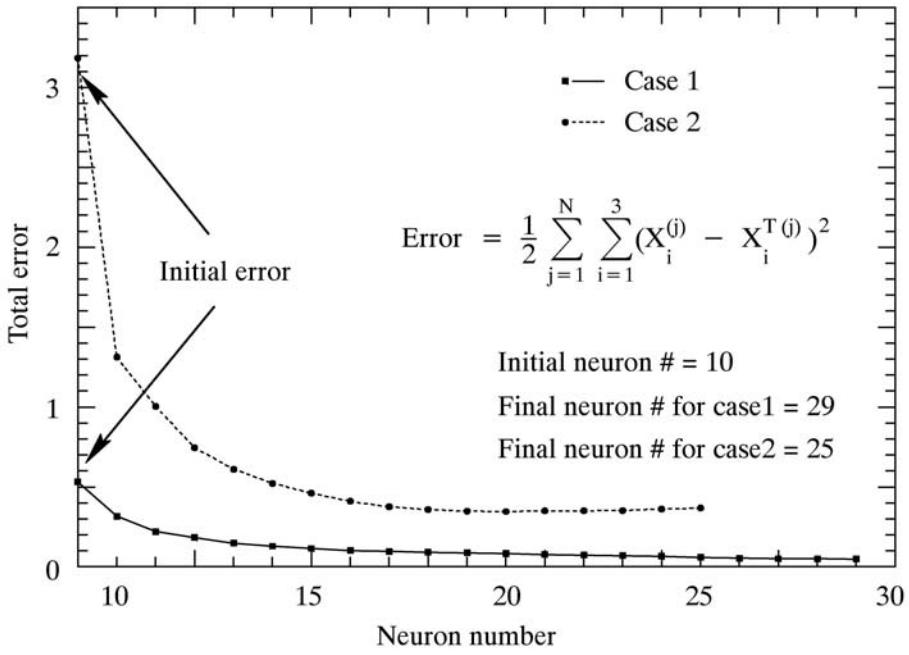

Figure 5.8 Training error and convergence of ANN models 1 and 2

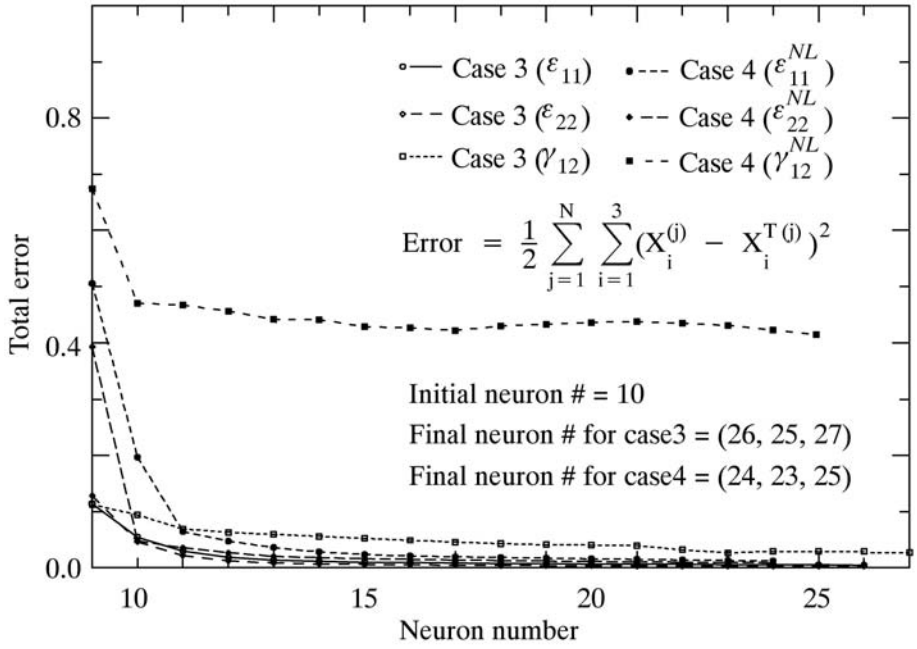

Figure 5.9 Training error and convergence of ANN models 3 and 4

Next, the trained ANN models are used to generate multi-axial stress-strain behaviors and are compared with available experimental results. Figure 5.10 shows the transverse tension stress-strain behaviors obtained from the trained ANNs and test results from the different off-axis coupons (i.e., $\theta = 30^\circ, 45^\circ, 60^\circ, and\ 90^\circ$) in their local material direction. The overall responses represented by the trained ANNs are very close to the experimental responses for most of the cases except for an off-axis angle of 30 degree, where the error is the largest (see more discussion at the end of this section). In this case, the ANN response is directly compared against the same data that was used for training and we are examining the ability of the trained ANN to extrapolate the training data. The term "ANN prediction" is used in this paper to describe the ANN response against the effective global material behavior or as a complete multi-axial nonlinear constitute model able to predict all in-plane strain components when given the in-plane stress components. The 30 degree case, in Figure 5.10, has the largest error compared to all other trained stress-strain paths. The transverse stress-strain responses generated from the single-variable output ANNs (cases 3 and 4) are very close to the experimental results as that of the vector output structural ANNs (i.e., cases 1 and 2). However, it is not clear which ANN can produce the best response as the output of all of them agrees well with the experimental observations. Using the transformation of the local material (ANN) stresses and strains, the global nominal stress-strain responses are generated for each off-axis case. Figure 5.11 shows the nominal off-axis tension responses expanded with the experimental results. The positive horizontal axis is used to plot the global axial strain, while the negative part is used for the transverse strain. The axial stress in the global direction is plotted against both the axial and transverse (Poisson's effect) strains. The overall transformed ANN responses are much closer to the experimental results once they are described in the global material direction. It is interesting that the proposed ANNs can generate much closer response to the experiment for the axial strain (ε_{11}) case than for the transverse strain (ε_{22}) case. In addition, the worst prediction case (i.e., local stress-strain behaviors at an off-axis angle of 30 degree) also produces a good agreement with experiments once they are converted

into the global responses. Figure 5.12 also shows the off-axis compression responses predicted by the trained ANNs and experiments. Similar to the tension responses, the global axial stress is plotted against both axial and transverse strain. In the compression case, the proposed ANNs can generate much closer responses to experiments than the tension case. As a result, it is demonstrated that the trained ANNs can generate good overall responses for all experimental cases. Good agreement with experimental data has been observed relatively more in the global responses. This can be explained by the reduced sensitivity when the stresses and strains are transferred to the global coupon-level stress-strain states. For example, this may explain why while the error is relatively larger for the local 30 degree case (see Figure 5.10), the combined off-axis response for this case shows good comparison in the global direction. That is, the transverse stress component (normal to the fiber) in this direction is smaller compared to the axial stress component and as such, its error is less pronounced.

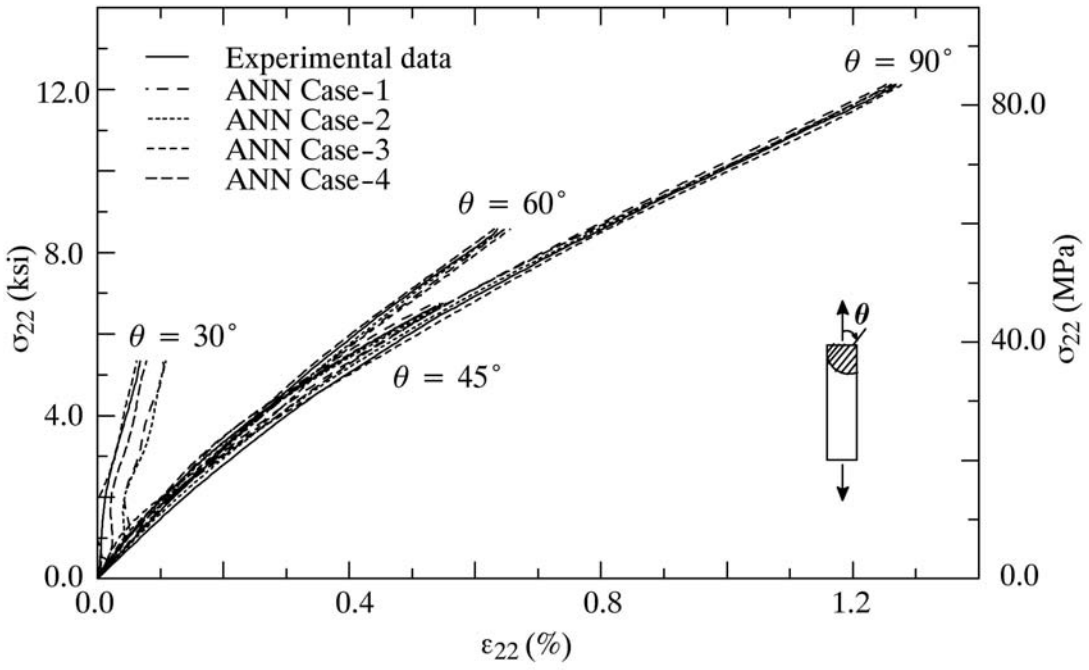

Figure 5.10 ANN representation of transverse stress-strain in the local material direction after training

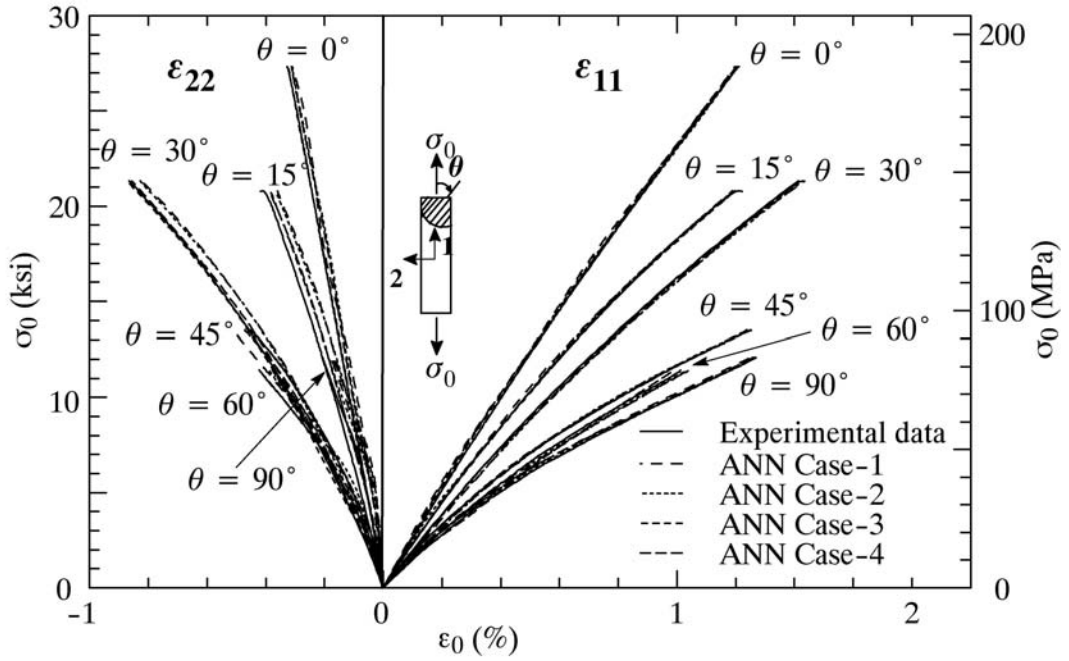

Figure 5.11 Global tension stresses versus direct and poisson's strains calculated from the local response of the trained ANNs

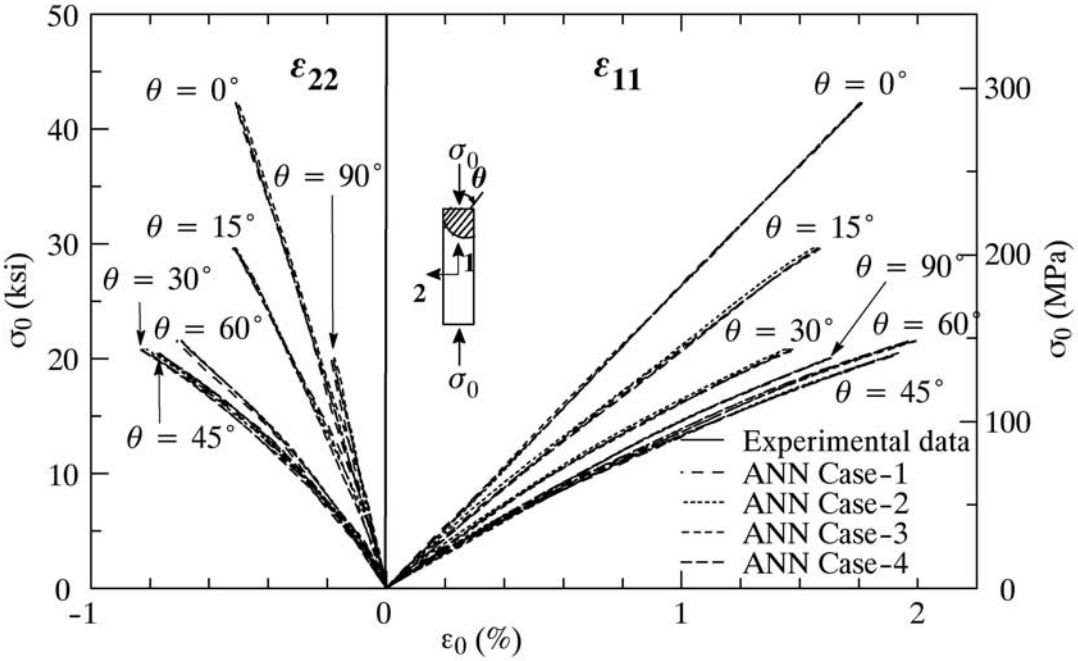

Figure 5.12 Global compression stresses versus direct and poisson's strains calculated from the local response of the trained ANNs

5.5 Nonlinear FEA Coupled with ANN Constitutive Models

The trained nonlinear ANN constitutive models should be suitable for integration as nonlinear models at the Gaussian material points in a general purpose FE code. Otherwise, the generated ANN models are not complete as they provide for a limited and partial approximation in parts of the response spectrum. The trained ANNs are implemented as user-defined nonlinear material models within the FEA software. The ABAQUS general purpose FEA code is coupled with the trained ANN material module for FRP composites. The nonlinear constitutive environment in displacement-based FE typically requires the user material to determine the current stress state given the strain increment and the previous history including strain, stress, time, and other state variables. Classical inelastic mechanics models are formulated using stress variables. This was the approach taken in this chapter with the input to the ANN. However, since the FE environment directly supplies the displacement gradients (strains), it makes sense to generate ANNs that have strain as an input (with/without history) and stresses as output. This type of ANN has the potential of dramatically reducing the computational (iterative) effort that is required at the material level and dramatically increasing the computational efficiency. However, it should be mentioned that the uniqueness of the computed stress state must be accounted for computationally or by the structure of the ANN itself. The strain and stress-based input ANNs were coupled with the FE code, and verification of their performance was needed. Towards that goal, a notched composite plate with an open hole was tested in order to examine the simulation results from the coupled FE with ANN material models. Figure 5.13 shows an FE model used in this simulation. A quarter shape of a rectangular coupon is modeled. The width and height are 0.875in (2.22cm) and 6in (15.24cm), respectively. The thickness is 0.5in (1.27cm) and the hole radius is 0.25in (0.635cm). The finite element model is composed of approximately 600 nodes and 550 plane-stress type elements (CPS4R). This FE model is implemented with the ANN user material modules and the new coupled ANN-FE code was verified for simple homogeneous cases. The choice of structural modeling for a transversely oriented thick-

section and notched composite plate was made because of the relatively large nonlinear responses expected. Remote uniform displacement is applied.

Figure 5.14 shows the experimental set-up for the notched plate and schematic drawings of the test and FE mesh. The upper and lower parts of the coupon were gripped by the jaws of MTS-810. Monotonic tension was applied as a uniform end displacement along with relative displacement that was acquired from a 2" extensometer attached on the specimen, as shown in Figure 5.12b, and located symmetrically about the mid-plane. Figure 5.15 shows the remote nominal stress versus the normalized extensometer displacement (strain) for both the FE-ANN simulation and the test. The FE-ANN coupled model is capable of predicting the overall behavior of the composite plate, while the experimental and FE-ANN extensometer response is linear. The local response around the open hole is nonlinear as shown in Figure 5.16.

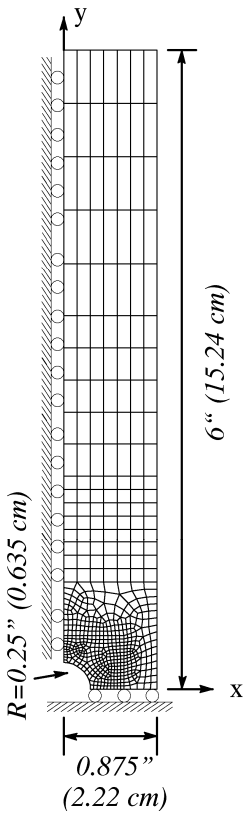

Figure 5.13 Geometry of the quarter FE model with hole

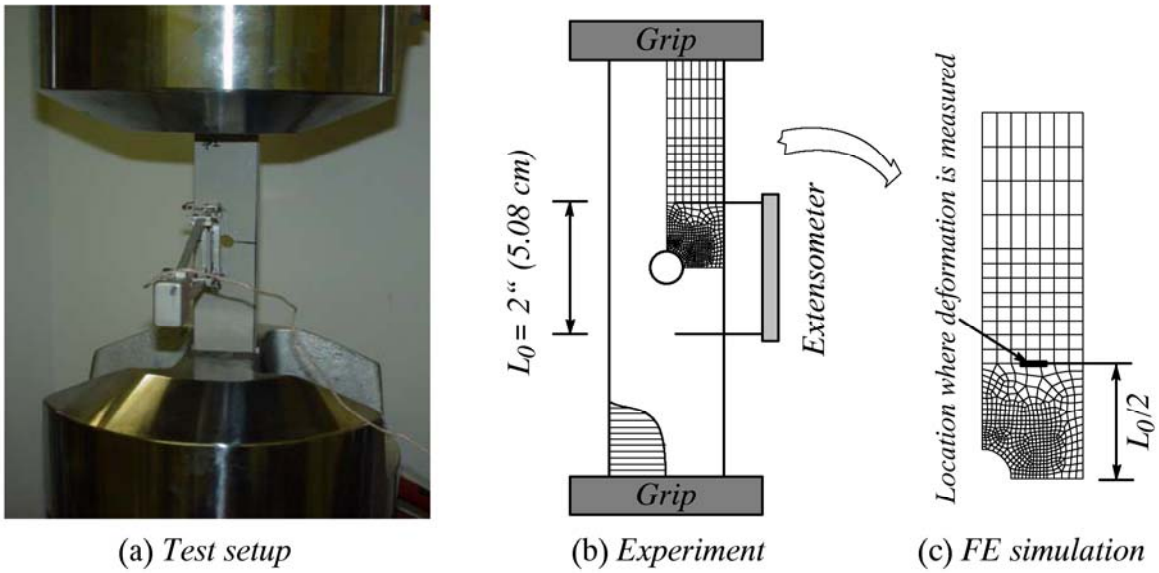

Figure 5.14 Schematic drawing of the experiment and FE simulation used in the verification

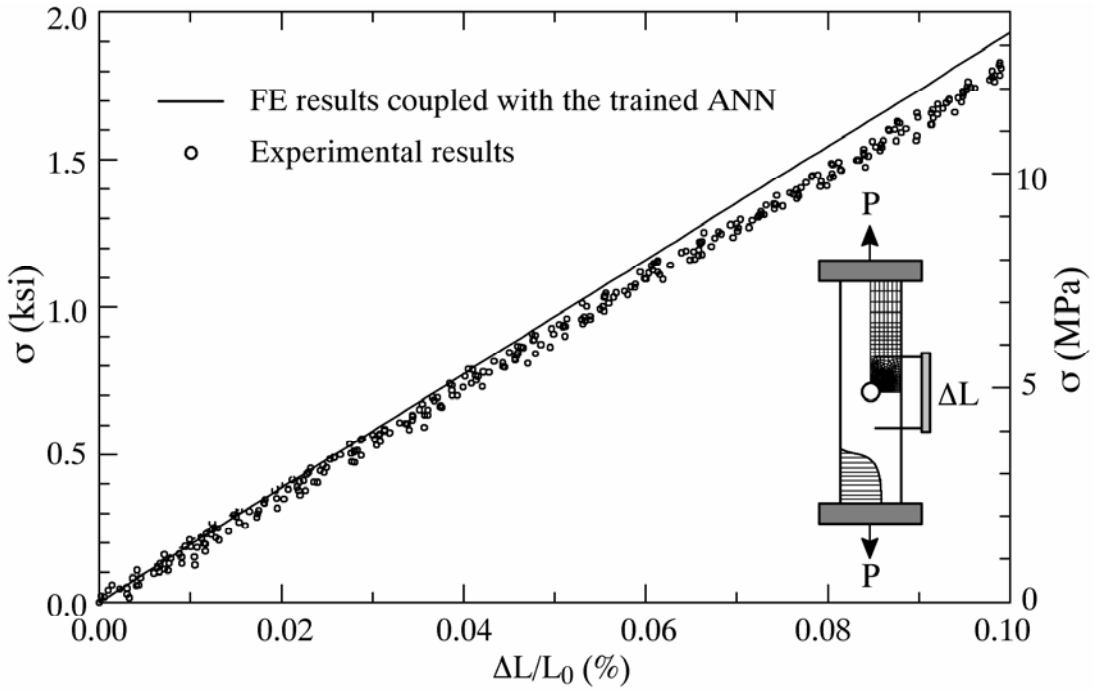

Figure 5.15 Prediction for the remote stress-strain curves obtained from experiments and FE simulations implemented with the proposed ANN material model

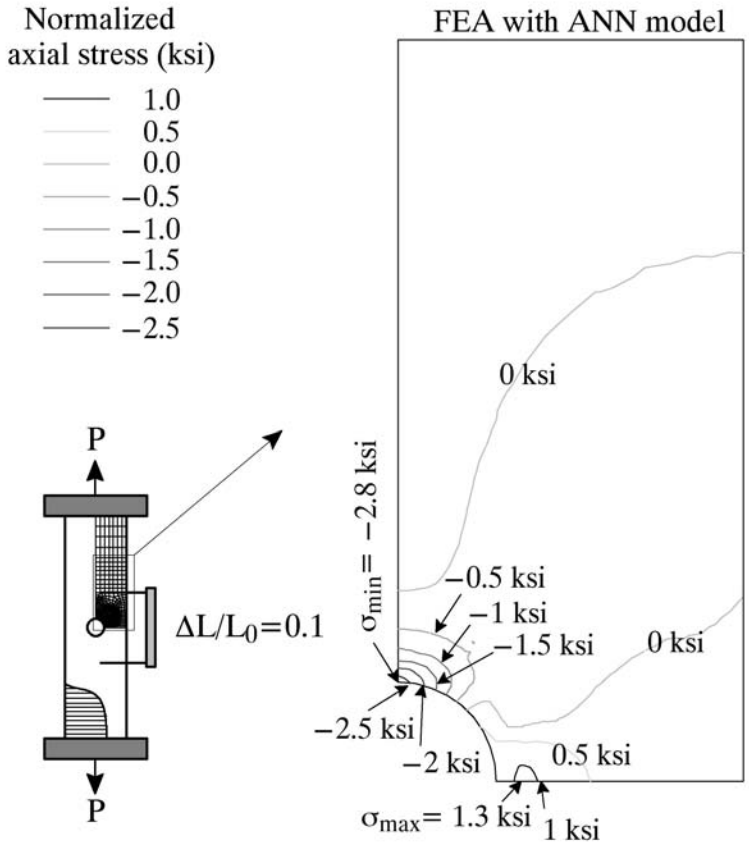

Figure 5.16 Normalized axial stress contours generated from the proposed ANN material model

The FE-ANN simulations are limited to the range of the trained ANN material models that are about 2% strain in axial and transverse directions. This explains why the global response is linear, and the local response can be nonlinear. Figure 5.17 schematically illustrates the unstable fluctuating ANN response beyond the training limit points. This leads to unsmooth FE convergence and ultimately divergence. The fact that the local stress has exceeded the training ANN level indicates the presence of local damage. Artificial neural network with damage capability is beyond the scope of this chapter.

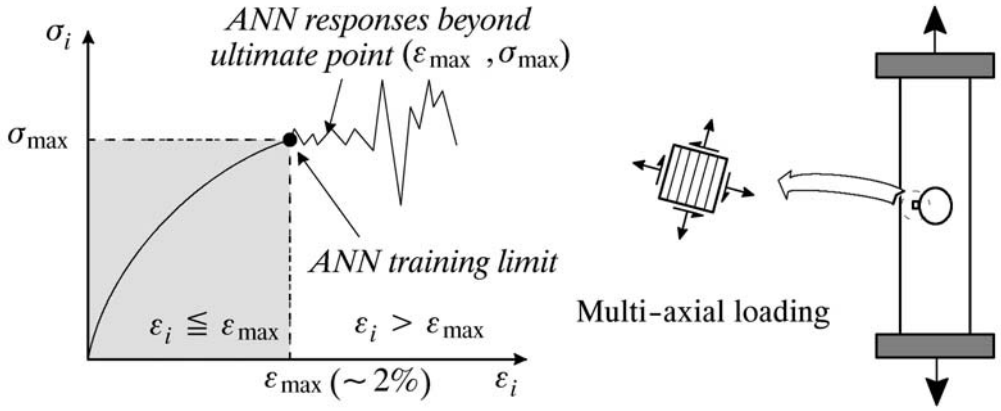

Figure 5.17 Schematic drawing of the ANN response out of range of the training data

CHAPTER 6: Micromechanical ANN Material Models with Damage Formulation

Classical analytical micromechanical material models with damage have been proposed based on phenomenological and empirical observations of damage behavior, such as crack between fiber and matrix, and fiber breaking for fiber reinforced materials (e.g., Caiazzo and Costanzo, 2000a and 2000b). Lemaitre (1992) and Maugin (2000) used energy release rate (ERR) to describe the damage material behavior in composite with thermodynamics of irreversible process (TIP) formulation. However, it is a challenge to describe the ERR because mathematical models need to explicitly recognize the crack system and their interaction. In addition, there are difficulties in calibrating the different material and damage parameters. Artificial neural network (ANN) can provide a new powerful tool to generate micromechanical models with damage behavior.

Haj-Ali et al. (2001) were among the first to use ANNs as micromechanical models to generate effective stress-strain response with different damage levels. They considered an interfacial crack between the fiber and matrix as their damage variable and used crack angle as a damage parameter in their UC models for uni-directional metal matrix composite. Their ANN models trained with 3D FE simulation results generated accurate effective plane stress-strain responses compared to the FE simulation results. However, damage dissipation was not fully considered in their ANN models.

This section presents micromechanical ANN models used to generate damaged material behavior and damage dissipation for different level of damage in fiber reinforced materials. Towards that goal, two micromechanical ANN models are proposed to generate effective stress and energy release rate, respectively for different damage and damage rate. The input/output variables of the

proposed two ANN models are selected based on the analytical observation of the thermodynamics of irreversible process (TIP). This chapter is divided into three parts. The first part presents formulation of energy release rate (ERR) in both continuum and fracture mechanical points of view. From the TIP, damage dissipation is formulated with strain energy density release rate, which is referred to as energy release rate (ERR) in fracture mechanics.

The second part deals with the proposed two ANN models and finite element (FE) unit cell (UC) model to train the proposed ANN models. The first micromechanical ANN model is to generate effective stress behaviors for different damage vector, while the second ANN model is to produce the energy release rate for different damage vector and its rate. The first ANN model includes effective strain and damage vector as input variable, while the effective stress is output. The second ANN has damage rate in addition to the first ANN input variables as inputs, while the output is energy release rate (ERR). They can be used separately, but two ANN models need to be used to characterize ERR that can describe damage dissipation from the effective stress-strain response. In order to examine the proposed micromechanical ANNs, three dimensional (3D) finite element (FE) unit cell (UC) model including cylindrical void in matrix (i.e., considered as damage in this chapter) is simulated with different void sizes.

The third part provides the ANN training result and demonstration of characterizing the damage and damage dissipation behavior from given effective stress-strain response. The training results of the two proposed ANNs are compared with FEA results. The trained micromechanical ANN models are also used to solve an inverse problem: characterizing the damage state and dissipation from an effective stress-strain response including softening (damage) behavior. Their prediction results are discussed at the end of this chapter.

6.1 Damage Formulation

In this study, energy release rate (ERR) is used to describe damage dissipation behavior of fiber reinforced materials. The formulation of ERR is derived from two different perspectives: In continuum level of materials and in fracture mechanics. The derived energy release rate (ERR) formulations in two different perspectives have the same definition, and they are used to determine the structure of ANN models proposed in this chapter. In addition, experimental method (i.e., ASTM STP 514) to calculate energy release rate (ERR) is also mentioned.

Energy Release Rate in Continuum Mechanics

In continuum level of materials, energy release rate (ERR) can be derived from the thermodynamics of irreversible process (TIP). In TIP, the free energy (ψ) is described with state variables (e.g., $\varepsilon_{ij}, T, \varepsilon_{ij}^{e}, \varepsilon_{ij}^{p}, r, \alpha_{ij}, D_m$) derived from experimental and analytical observations as follows (e.g., Lemaitre, 1992):

$$\psi = \psi(\varepsilon_{ij}, T, \varepsilon_{ij}^{e}, \varepsilon_{ij}^{p}, r, \alpha_{ij}, D_m) \tag{6.1}$$

Under the isothermal condition, the above equation is simplified by removing the temperature variable (T). In addition, strain variables can be replaced with only one variable of elastic strain (i.e., $\varepsilon_{ij} - \varepsilon_{ij}^{p} = \varepsilon_{ij}^{e}$).

$$\psi = \psi(\varepsilon_{ij}, \varepsilon_{ij}^{e}, \varepsilon_{ij}^{p}, r, \alpha_{ij}, D_m) = \psi([\varepsilon_{ij} - \varepsilon_{ij}^{p}], r, \alpha_{ij}, D_m) = \psi(\varepsilon_{ij}^{e}, r, \alpha_{ij}, D_m) \tag{6.2}$$

The simplified formulation of free energy can be decomposed into elastic and inelastic parts with the reduced number of state variables.

$$\psi = \psi(\varepsilon_{ij}^{e}, r, \alpha_{ij}, D_m) = \psi^{e}(\varepsilon_{ij}^{e}, D_m) + \psi^{p}(\alpha_{ij}, r) \tag{6.3}$$

By taking the partial differential equation (PDE) of the elastic part of the free energy, stress is formulated and can be expressed as effective stress $(\overline{\sigma}_{ij})$ including elastic strain and damage vector as its variables as follows:

$$\sigma_{ij} = \rho \frac{\partial \psi}{\partial \varepsilon_{ij}^{e}} = \rho \frac{\partial \psi^{e}(\varepsilon_{ij}^{e}, D_m)}{\partial \varepsilon_{ij}^{e}} \equiv \overline{\sigma}_{ij}(\varepsilon_{ij}^{e}, D_m) \tag{6.4}$$

Strain energy density release rate is also derived from the elastic part of the free energy.

$$Y_m = -\rho \frac{\partial \psi}{\partial D_m} = -\rho \frac{\partial \psi^{e}}{\partial D_m} \tag{6.5}$$

From the inelastic part of the free energy, the other thermodynamic forces can be formulated as follows:

$$R = \rho \frac{\partial \psi^{p}}{\partial r} \text{ and } X_{ij} = \rho \frac{\partial \psi^{p}}{\partial \alpha_{ij}} \tag{6.6}$$

Here, ρ: constant material density; r: the damage accumulated plastic strain, whose associated variable is the isotropic strain hardening variable R. α_{ij}: the back strain tensor, whose associated variable is the back stress X_{ij}^{D}.

Equation 6.5 can be re-formulated by using the effective stress instead of the PDE of free energy relating to the elastic strain variable in Equation 6.7. The re-formulated strain energy density

release rate is dependent on effective stress, elastic strain, and damage vector, as well as their rates as shown in Equation 6.8.

$$Y_m = -\rho \frac{1}{\partial D_m} \partial \psi^e = -\frac{1}{\partial D_m} \int_0^{\varepsilon^e} \rho \frac{\partial \psi^e}{\partial \varepsilon_{ij}^e} d\varepsilon_{ij}^e = -\frac{1}{\partial D_m} \int_0^{\varepsilon^e} \overline{\sigma}_{ij}(\varepsilon_{ij}^e, D_m)\, d\varepsilon_{ij}^e \tag{6.7}$$

$$Y_m = -\int_0^{\varepsilon^e} \frac{\overline{\sigma}_{ij}(\varepsilon_{ij}^e, D_m)}{\partial D_m} d\varepsilon_{ij}^e \tag{6.8}$$

Where, Y_m is the positive quantity of the strain energy density release rate; and D_m is the damage variable with m damage modes.

The strain energy density release rate derived from the TIP (i.e., Equation 6.5) has the same definition as the one of the ERR in fracture mechanics. From the fracture mechanics perspective, the energy release rate can be described as shown in Equation 6.9. Using chain rule, the strain energy density release rate (in Equation 6.5) becomes proportional to the energy release rate. If the damage area and damage vector for different damage modes are the same, the strain energy density release rate can be expressed as energy release rate dependent on damage vector as shown in Equation 6.11.

$$G = -\frac{d(U - W)}{dA} = -\frac{d\psi^e}{dA} \tag{6.9}$$

$$Y_m = -\rho \frac{\partial \psi^e}{\partial D_m} = -\rho \frac{\partial \psi^e}{\partial A_m} \frac{\partial A_m}{\partial D_m} \propto G \frac{\partial A_m}{\partial D_m} \tag{6.10}$$

$$Y_m \cong G(D_m) \tag{6.11}$$

Where, $G(D_m)$ is the energy release rate; (U) is strain energy; and (W) is work done by external forces in fracture mechanics.

Energy Release Rate in Fracture Mechanics

In fracture mechanics, energy release rate (ERR) is commonly formulated from the potential energy to describe fracture mechanism such as crack and damage dissipation for structural materials (Anderson, 2005). The potential energy (Π) is defined as a subtraction of work (W) done by external forces from strain energy (U), and the general formulation of ERR is described by taking differential equation of the potential energy (Π) with damage area (A).

$$G = -\frac{d\Pi}{dA} = -\frac{d(U-W)}{dA} \tag{6.12}$$

For the linear elastic material and structural behavior, Equation 6.9 is simplified into two following Equations 6.13 and 6.14 under constant load and constant displacement, respectively. Figure 6.1 shows the schematic drawing of the load-displacement response to derive the ERR under the constant load and displacement.

$$G = -\frac{d\Pi}{dA} = \frac{P}{2}\frac{d\Delta}{dA} \text{ (Under constant load)} \tag{6.13}$$

$$G = -\frac{d\Pi}{dA} = \frac{\Delta}{2}\frac{dP}{dA} \text{ (Under constant displacement)} \tag{6.14}$$

Where, the potential energy of elastic body: $\Pi = U - W = -\frac{1}{2}P\Delta = -U$; strain energy: $U = \int_0^{\Delta} P\, d\Delta = \frac{P\Delta}{2}$; damage or crack area: A; and work done by external forces: $W = P\Delta$.

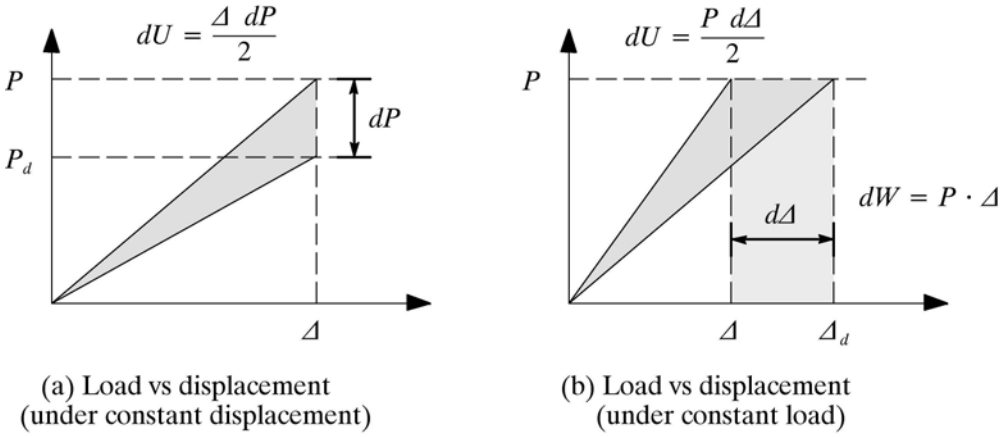

Figure 6.1 Linear load and displacement response including damage under constant displacement and load

In the case of (heterogeneous) composite materials, nonlinear load-displacement responses can be generated due to their different material constituents (e.g., different mechanical behavior of fiber and matrix). Therefore, an integral formulation of the ERR may be needed to explain the nonlinear load-displacement response. The derived integral-type formulation of the ERR under the constant displacement and load are described in Equations 6.16 and 6.18, respectively. Figure 6.2 shows the schematic drawing of the integral-type of formulation of the ERR for the nonlinear load-displacement response.

$$G = -\frac{d(U-W)}{dA} = -\frac{1}{dA}\left(\int_0^{\Delta} dP \cdot d\Delta - dP \cdot \Delta\right) \tag{6.15}$$

$$G = \frac{dP}{dA} \cdot \Delta - \frac{1}{dA}\int_0^{\Delta} dP \cdot d\Delta \quad \text{(constant displacement)} \tag{6.16}$$

Where, the differential of strain energy: $dU = \int_0^{\Delta} dP \cdot d\Delta$ and the differential of work: $dW = dP \cdot \Delta$.

$$G = -\frac{d(U-W)}{dA} = -\frac{1}{dA}\left(\int_0^P d\Delta \cdot dP - P \cdot d\Delta\right) \tag{6.17}$$

$$G = \frac{d\Delta}{dA} \cdot P - \frac{1}{dA}\int_0^P d\Delta \cdot dP \quad \text{(constant load)} \tag{6.18}$$

Where, the differential of strain energy: $dU = \int_0^P d\Delta \cdot dP$ and the differential of work: $dW = P \cdot d\Delta$.

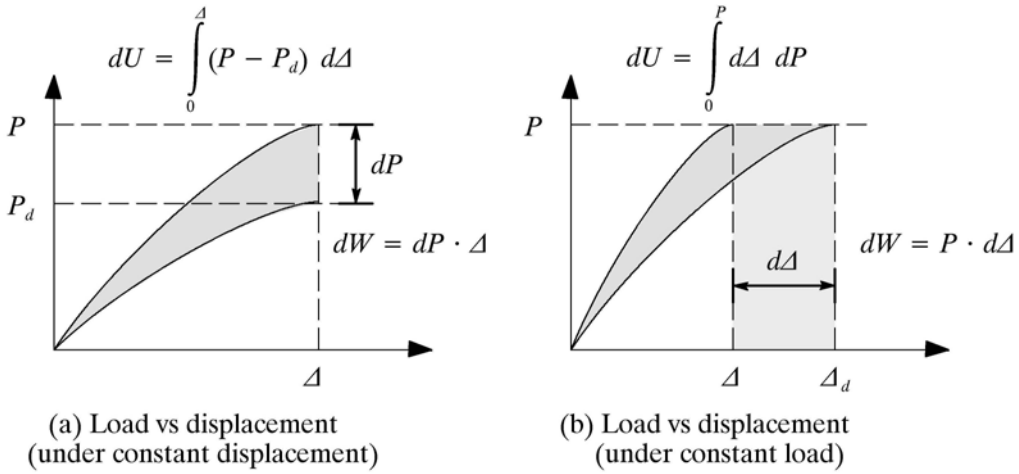

(a) Load vs displacement (under constant displacement)

(b) Load vs displacement (under constant load)

Figure 6.2 Nonlinear load and displacement response including damage under constant displacement and load

Energy Release Rate in Experiments

Landes and Begley (1972a and 1972b) were among the first to measure J, which is energy release rate in nonlinear inelastic materials, from the experimental results. Figure 6.3 shows the schematic drawing of their measurement of ERR. The procedure of this method can be divided into three steps. In the first step, a series of testing coupons with the same size, material, and geometry, but different crack length (a) are prepared and tested. The testing result (i.e., load-displacement response for different crack length) is achieved. In the second step, the strain energy versus crack length response is obtained by calculating the area under the load-displacement response for different crack length (a). In the third step, energy release rate versus displacement response is plotted by taking the slope of the $U-a$ response measured in the second step. For linear elastic materials, the measured energy release rate J becomes G. In this chapter, this method is used to calculate energy release rate (G).

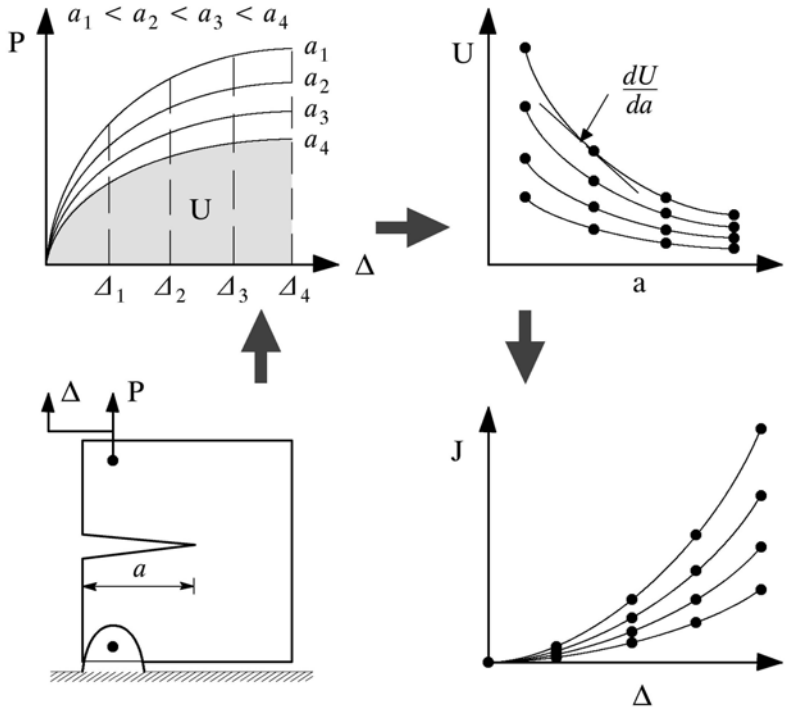

Figure 6.3 Schematics of experimental measurement of energy release rate performed by Landes and Begley, ASTM STP 514 (Adapted from Anderson, 2005)

6.2 Proposed Micromechanical ANN Models including Damage Dissipation

In this chapter, two different micromechanical ANN models are proposed to generate in-plane stress response for different damage levels and energy release rate describing damage dissipation, respectively. These two ANN models are inspired from the two derived relations as shown in Equations 6.4 and 6.8, respectively. Figure 6.4 shows the schematic drawing of the two proposed micromechanical ANN models. The first ANN includes in-plane strain components and damage variable as its input, while corresponding stress components are its output. The input of the second ANN is incremental variable. It includes strain components for next increment (n+1), current damage variable, and current damage rate as its input variables, while the output is energy release rate for next increment (n+1). These two ANN models can be individually or simultaneously used for their purposes. For example, if we need to characterize the damage vector from given stress-strain response, only the first ANN model can be used. However, if we need to identify the damage dissipation from the given stress-strain response, both the first and second ANN models should be sequentially used to characterize ERR because the second ANN model needs the damage level as its input. In addition, the inverse-type ANNs to characterize stress-strain response with different damage level from given ERR can be generated.

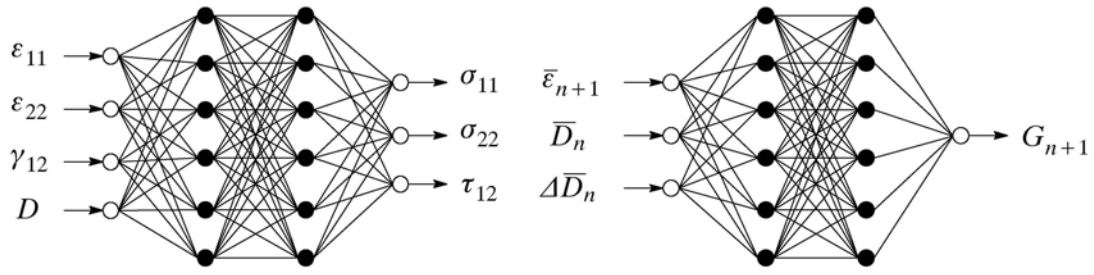

(a) ANN to generate effective in-plane stresses for different damage levels

(b) ANN to generate energy release rate for different damage rates

Figure 6.4 Schematic drawing of two proposed micromechanical ANN models to generate effective in-plane stress responses with different damage vector and energy release rate to describe damage dissipation, respectively.

Figure 6.5 shows the schematic drawing of the proposed ANN models as a material subroutine of displacement-based FEA software. From given input variables, damage rate is checked. If there is damage dissipation $(\Delta\overline{D}_n \neq 0)$, appropriate strain increment $(\Delta\overline{\varepsilon}_n^{new})$ is calculated for current damage rate using damage evolution models. Strain components and damage vector for next step $(n+1)$ are updated with the calculated or given strain and damage increments. The proposed ANN models are then used to generate effective stress components and energy release rate corresponding to the updated strain and damage for the next step.

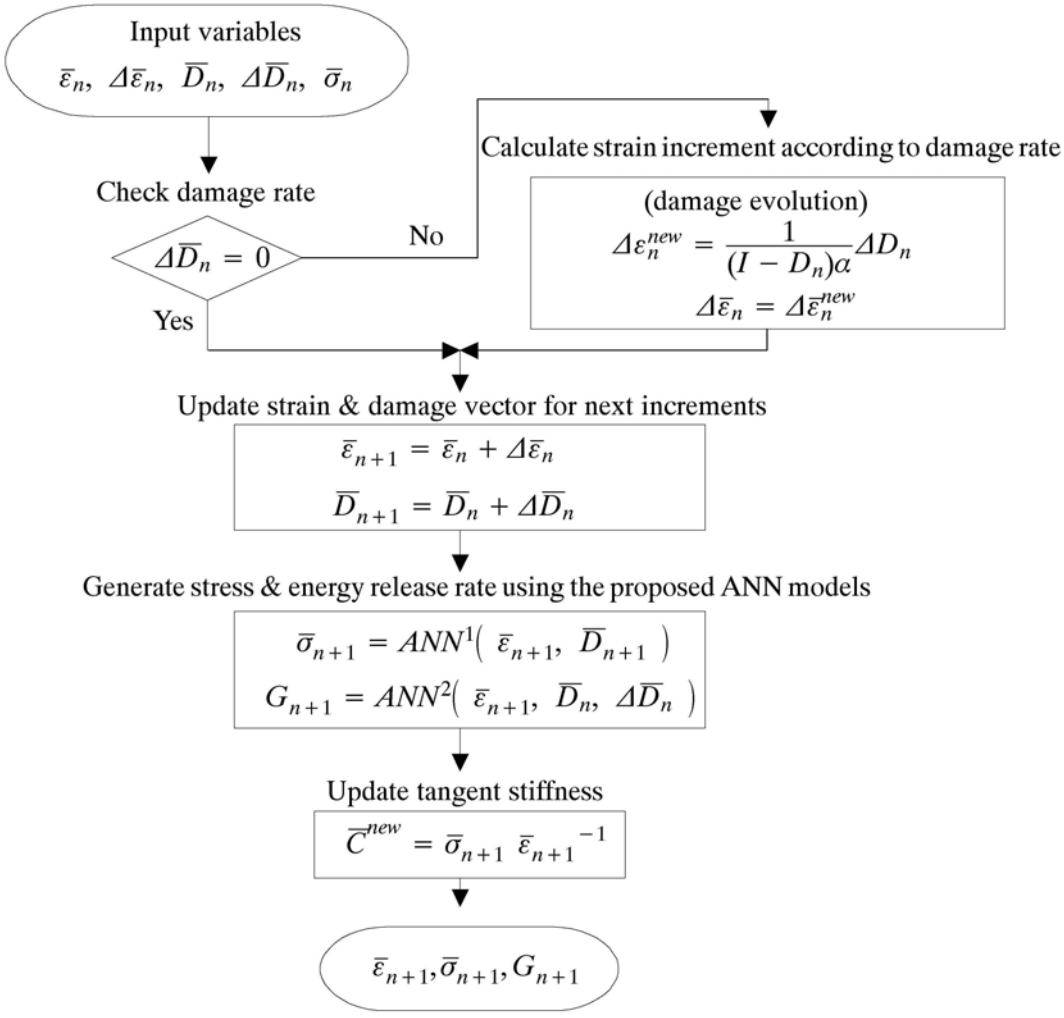

Figure 6.5 Schematic drawing of the proposed ANN models as a material subroutine of FEA software

Finite Element Unit-Cell for Fiber Reinforced Materials with Parametric Void Damage

In order to train the proposed micromechanical ANN models, a three dimensional (3D) finite element (FE) unit cell (UC) model including void damage is developed using an auto-mesh generator, TrudGrid (XYZ scientific applications, 1999). All dimensions of the FE-UC model are parameterized, so various FE-UC models including different sizes of void can be easily generated. In the chapter, seven different void volume fractions (i.e., $V_v = A_v = 0$, 0.01, 0.03, 0.06, 0.09, 0.12, and 0.15) are considered. The corresponding radiuses of void are listed: 0, 0.0564, 0.0977, 0.138, 0.169, 0.195, and 0.218. Figure 6.6 shows the schematic drawing of the developed FE-UC models. The FE-UC model is a cubic with three equal length of l and has the FVF of 0.3. The generated FE-UC models are composed of about 2200 linear brick-type elements with 8 nodes (C3D8). They have the same number of nodes and elements, even though they include different radiuses of void.

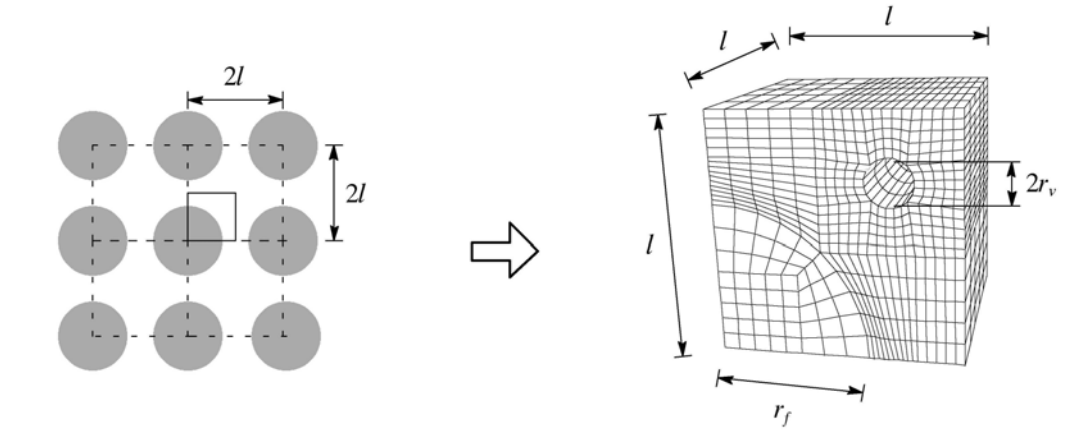

(a) Fiber-matrix material structure (b) Finite element (FE) unit cell (UC) model

Figure 6.6 Schematic drawing of finite element (FE) unit cell (UC) model including void damage used in this study: (a) Fiber-matrix material structure and (b) Finite element (FE) unit cell (UC) model.

Where, r_f: radius of fiber; r_v: radius of void; volume of the unit cell (UC), $V_T = 1$; volume of fiber is $V_f = \frac{\pi r_f^{\,2}}{4} = A_f$; volume of matrix is $V_m = 1 - V_f$; volume of void is $V_v = \pi r_v^{\,2}$; and the fiber volume fraction (FVF) of the UC model is $FVF = A_f = V_f$

The FE simulation with different sizes of cylindrical void is performed to generate training data, e.g., effective stress-strain response and energy release rate with different damage variable. In the FE simulation, it is postulated that the size of initially applied void does not change during FE simulation. A simple material and loading system (i.e., linear elastic material and one dimensional loading, only $\sigma_{22} \neq 0$) is considered to demonstrate if the proposed ANNs can characterize both damage and damage dissipation from given effective stress-strain response. Material properties of fiber and matrix used in the FE simulation are shown in Table 6.1. The FE simulation is performed with displacement control. The FE-UC models including different radiuses of void are pulled with an amount of displacement, and their responses, i.e., reactions are measured during the FE simulation. The boundary condition of FE-UC models is considered as roller supports. Three sides of FE-UC models (i.e., x-y, y-z, and x-z planes) from origin are constrained not to move to their normal directions. This FE simulation is performed until the displacement (i.e., effective strain) becomes 0.1 with strain increment less than 200. The training data for the first ANN model (i.e., effective stress-strain response for different radiuses of void) is generated through this FE simulation.

Table 6.1 Material properties of fiber and matrix used to generate training data (Haj-Ali et al., 2001)

	E_1 (10^3 ksi)	E_2 (10^3 ksi)	G_{12} (10^3 ksi)	v_{12}	v_{23}
AS4 Graphite	27	2.5	5	0.3	0.25
3501 Epoxy	0.73			0.4	

Figure 6.7 shows the training data generated from the FE-UC models with different damage levels (i.e., different size of voids). Figure 6.7a shows the effective stress-strain response (i.e., 777 data sets) for different damage values, training data for the first micromechanical ANN model proposed in this chapter. It shows that the effective stress-strain responses decrease as damage level

increases. Figures 6.7b and 6.7c shows the strain area versus void area, and ERR versus effective strain responses used to generate training data for the second ANN model, respectively. A total of 310 data sets are generated from these two relations, and their calculation is reported in ASTM STP 514.

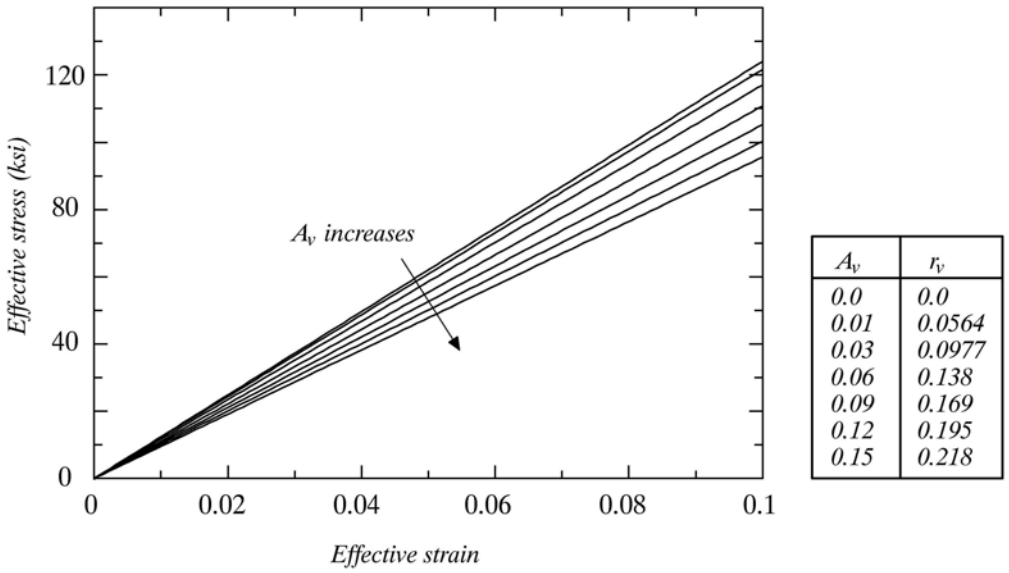

(a) Training data (effective stress−strain response) with void areas

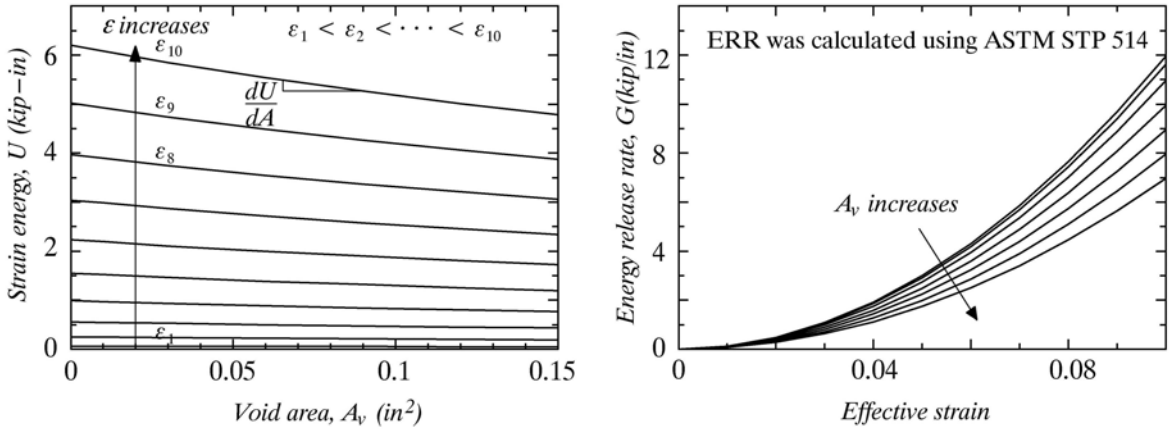

(b) Strain energy vs void area

(c) Energy release rate vs effective strain

Figure 6.7 Training data with different damage levels: (a) Effective stress-strain response; (b) strain energy-void area; and (c) energy release rate-effective strain

6.3 Verifications

The proposed two micro-mechanical ANN models were trained with their training data (see Figure 6.7) using adaptive training method. The training of both the first and second ANNs started with 5 neurons, but they are ended up with different final neuron numbers of 10 and 13 neurons, respectively. Figure 6.8 shows the first ANN training result, i.e., effective stress-strain responses. The ANN prediction and training data are described as solid and dashed lines, respectively. The trained first ANN is less sensitive when there is no damage or the damage level is relatively small, e.g., $r_v = 0.0564$. However, the first trained ANN model generates overall accurate responses compared to the training data for different damage levels.

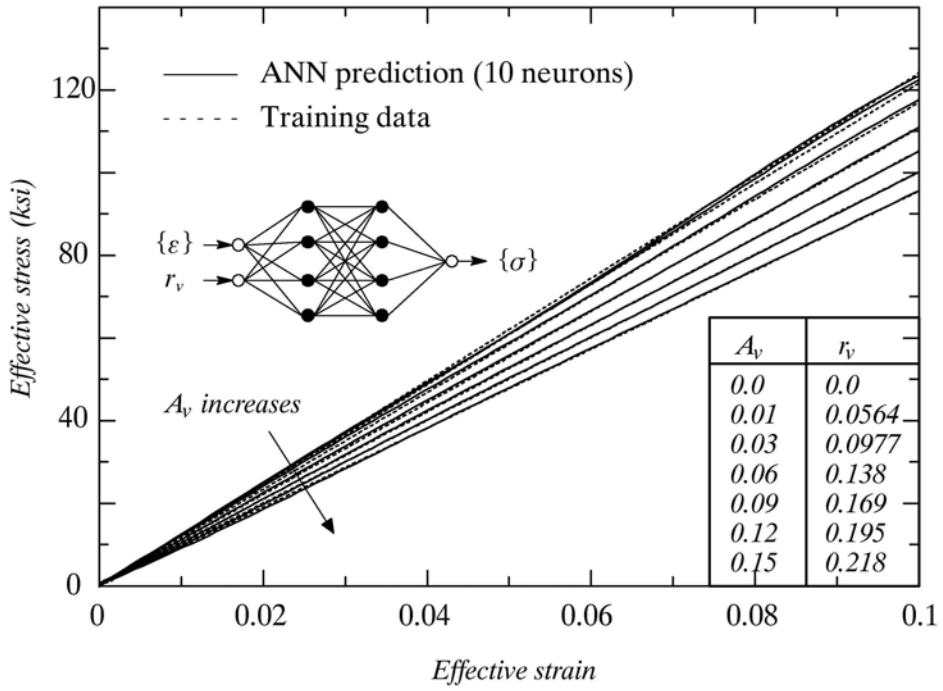

Figure 6.8 The first ANN training result (i.e., effective stress-strain response)

The trained first ANN model is also used to solve an inverse problem, to characterize damage level for a given effective stress-strain response. In order to examine the use of the proposed ANN model in solving the inverse problem, damage softening behavior is artificially added to the effective stress-strain response with the radius of 0.0977. This is called as Behavior-1 in the later of this part. The effective stress-strain response of Behavior-1 is equal to the one with the radius of 0.0977 for the strain of 0 to 0.08. However, smooth damage (softening) behavior is created for the strain of 0.08 to 0.09 within the damage levels of 0.0977 and 0.218. Figure 6.9 shows the effective stress-strain responses of training data, artificial damage behavior (i.e., Behavior-1), and ANN prediction, as well as predicted damage state (i.e., radius of void) from Behavior-1. Training data is described as dashed line, while Behavior-1 and ANN prediction are showed with diamond symbols and solid line, respectively. The effective stress-strain response predicted from the trained ANN show a good agreement with Behavior-1.

Figure 6.9 also shows the radius of void predicted from Behavior-1 using the trained first ANN. From strain range of 0 to 0.08, predicted radius ranges from 0.1 to 0.123, while the applied radius in Behavior-1 is 0.0977. The predicted radius shows irregular damage behavior of negative rate (i.e., the material can heal itself). The trained ANN model is used to directly characterize damage parameter without any constraints or restrictions (e.g., the Clausius-Duhem inequality and its following Kuhn-Tucker conditions) in the training or in solving this inverse problem. This prediction error or difference can be explained by the different sensitivity of the trained ANN for low values of effective strains. Thus, the damage variable is less sensitive to effective stress-strain response. However, the predicted radius becomes closer to the applied radius as strain increases. When strain is 0.08, predicted radius is 0.1 almost the same as the applied radius of 0.0977. This sensitivity can be improved by using training data with good quality or adding more neurons. However, the trained ANN produces accurate radius compared to the applied radius beyond the strain of 0.08 where damage dissipation is artificially created. When strain is 0.09, both the applied and predicted radiuses

are the same as 0.218. This examination demonstrates that the proposed ANN model can estimate damage levels from given effective stress-strain response.

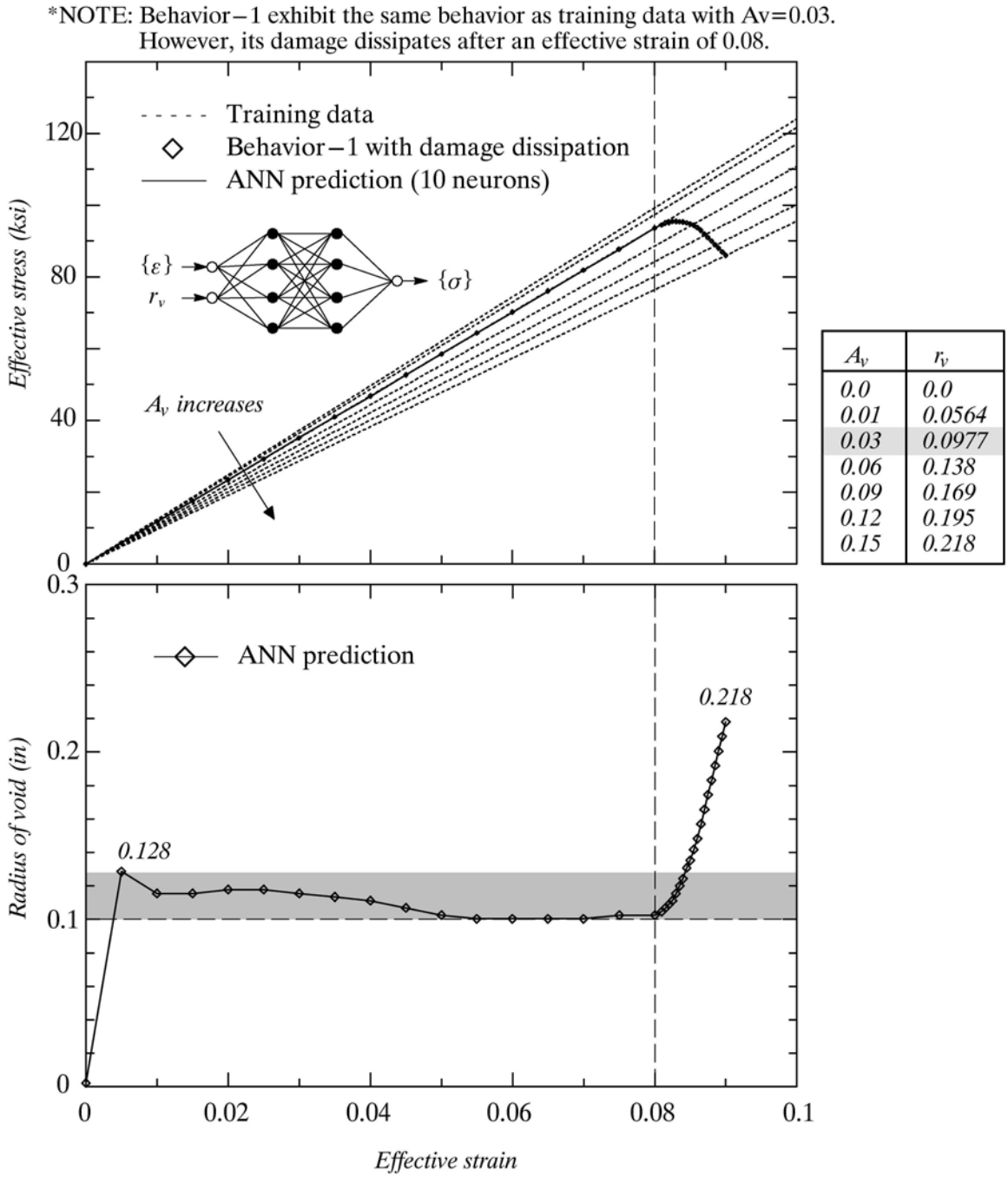

Figure 9.9 ANN prediction of damage level (i.e., radius of void) for a given effective strain-stress response

Figure 6.10 shows that training result of the second ANN model. The predicted energy release rate (ERR) for different damage and damage rates that is used in the training data is expressed with training data as diamond symbols. The diagonal solid line describes the quality of the ANN training, if ANN prediction is identical to the training data. As shown in this figure, the trained ANN generated accurate energy release rate for different damage cases compared to the training data. In addition, the proposed second ANN is used to characterize the ERR of Behavior-1 from the given effective stress-strain response with damage behavior. The radius of the void predicted from the first ANN is used as the part of input for the second ANN.

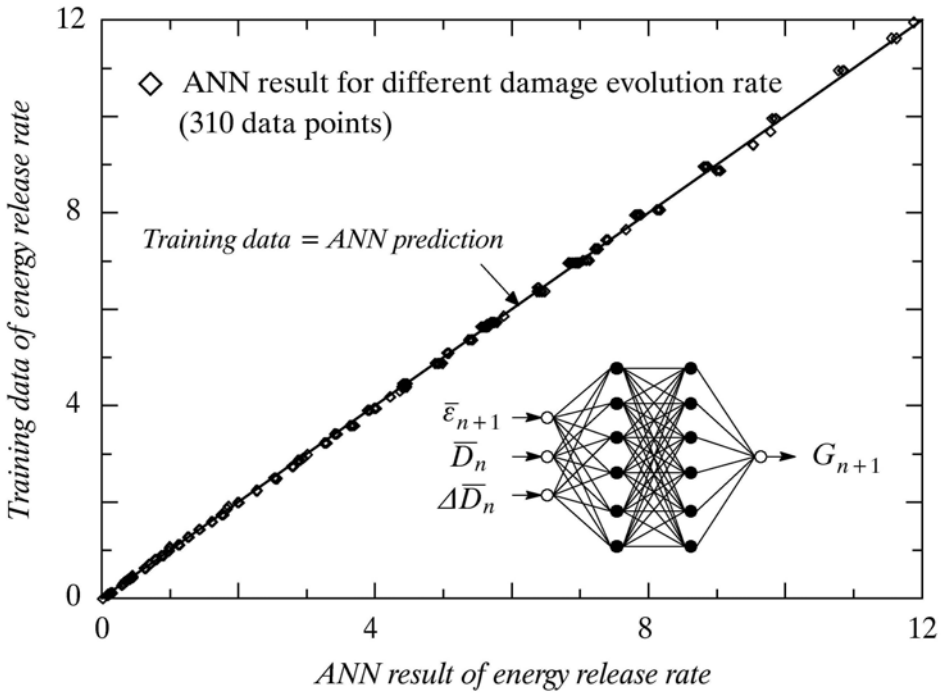

Figure 6.10 ANN training result (i.e., energy release rate for different input variables)

The damage evolution rate of Behavior-1 is proposed in this section (i.e., void growth in the matrix). The proposed damage rate follows the well-known Gurson's model (1977) that describes both nucleation and growth of void in metal plasticity. The Gurson's damage variable rate and plastic

strain rate for isotropic metallic materials are shown in Equation 6.19. However, a general rate is used in this study in order to demonstrate the developed ANN formulation. The developed damage evolution describes the relation between the damage variable rate and effective strain rate. In order to describe the relation, we postulate that effective strain is proportional to average strain in matrix, such as $\partial \varepsilon^m / \partial t = B(\partial \varepsilon / \partial t)$. Equation 6.21 shows the generalized damage rate.

$$\frac{\partial f}{\partial t} = (1 - f)\frac{\partial \varepsilon^{pl}}{\partial t} : I \tag{6.19}$$

$$\frac{\partial D}{\partial t} = A(1-D)\frac{\partial \varepsilon^m}{\partial t} = AB(1-D)\frac{\partial \varepsilon}{\partial t} = \alpha(1-D)\frac{\partial \varepsilon}{\partial t} \tag{6.20}$$

$$\Delta D_n = \alpha(1 - D_n)\Delta \varepsilon_n \tag{6.21}$$

Where, f : modeling parameter of Gurson's model; ε^{pl} : plastic strain; ε^m : average strain in matrix; A, B, and α : parameters; and ΔD_n : damage rate in step n.

Figure 6.11 shows parameter calibration result for Behavior-1. From the training data for the second ANN, parameter (α) is calculated for different damage, damage rate, and effective strain using Equation 6.21. Using a linear function, the responses are calibrated for specific range from 0.08 to 0.09, where damage dissipation occurs. Both the calculated and calibrated parameters (α) for Behavior-1 are described with diamond symbols and dashed line, respectively.

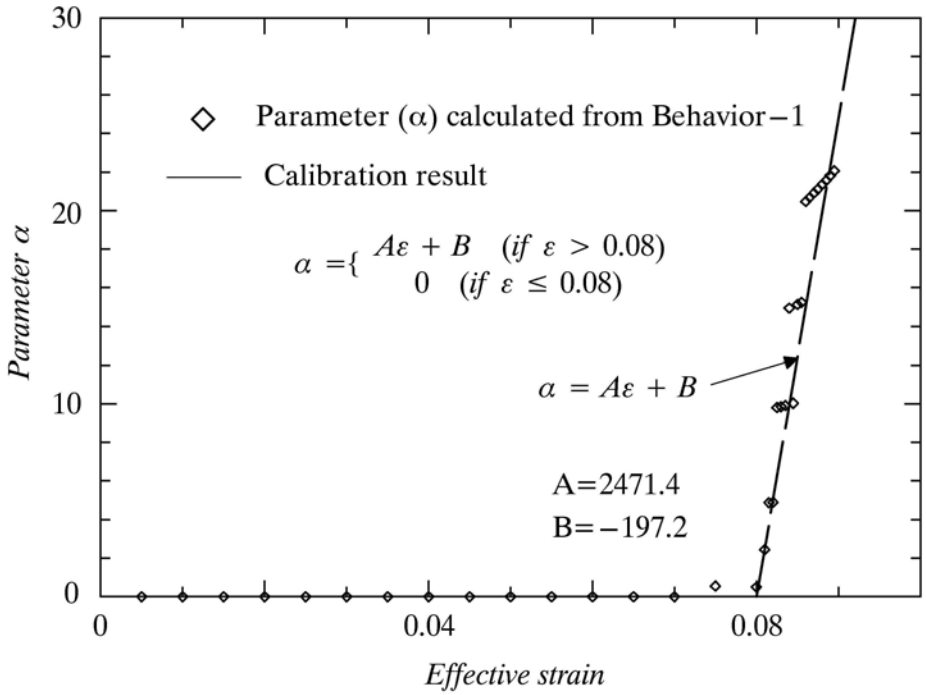

Figure 6.11 Calibration of parameter (α) for Behavior-1

Figure 6.12 shows the energy release rate for different damage levels and ANN prediction result for Behavior-1. The predicted ERR and training data are described as solid line with diamond symbols and dashed line, respectively. The ERR of Behavior-1 is generated using the two proposed ANN models. Specially, when there is damage dissipation (from 0.08 to 0.09) new strain rate considering damage rate is calculated using Equation 6.20. The procedure is described in Figure 6.5. The predicted ERR exhibits the same response with the training data with the radius of 0.0977 during strain range from 0 to 0.08. And then the slope of the predicted ERR begins to decrease beyond the strain of 0.08, and the ANN generates the ERR value of 5.64 when the strain is 0.09. That is the same value of training data with the radius of 0.218. This simple example shows that the proposed ANNs can be used in solving an inverse problem to characterize damage levels and energy release rate from given stress-strain response.

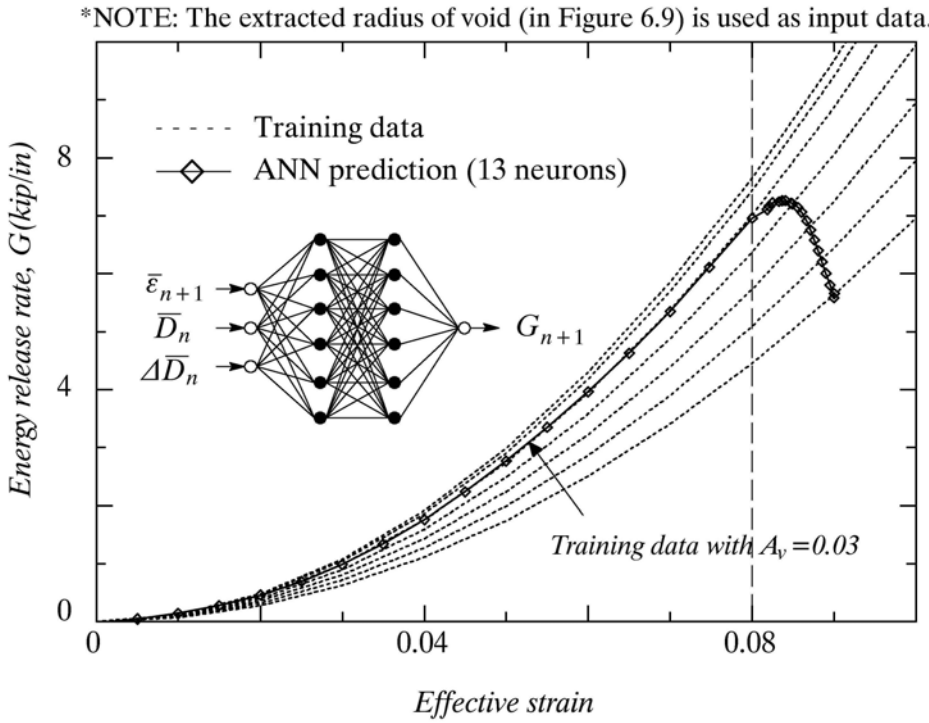

Figure 6.12 ANN prediction of energy release rate

CHAPTER 7: Summary and Future Recommendations

In this study, a new class of nonlinear multi-scale ANN constitutive models was proposed and verified. The ANN constitutive models included different dimensionless input/output variables and were generated both at the micro- and macro-scales of the material systems. For example, ANN models were trained using nanoindentations for metallic and polymeric material systems with and without thin films as a top layer. Complete plane-stress nonlinear ANN models were also generated for orthotropic composite material system and successfully trained from experiments conducted in this study. Nonlinear ANN constitutive models were also investigated for metallic and polymeric material systems with emphasis on new unique characteristics and aspects. The first was to characterize the in-situ nonlinear and time-dependent material properties of micro- and nano-scaled materials from static and time-dependent nanoindentation test results, respectively. The second was to generate multi-axial ANN stress-strain responses at the macro-scale and micromechanical material behavior with damage for FRP composites. The proposed ANN models were successfully trained with simulated FEA data or others from experimental results, such as off-axis tension/compression and pure shear tests for FRP composites. The proposed nonlinear multi-scale ANN constitutive models were shown to be effective and efficient through numerical and experimental verifications by comparing the ANN predictions against simulated FEA or experimental results that were not part of the ANN training data. This chapter presents a summary, major conclusions, and future recommendations.

7.1 Summary

The proposed ANN modeling approach was successfully applied to generate and characterize nonlinear material behaviors for metallic, polymeric, and composite material systems. Constitutive

ANN models were generated for FRP composites and nano- and micro-scaled substrate-film metallic systems. The ANN models were trained and used to generate the overall nonlinear material behaviors, such as the multi-axial response of FRP composites with and without in-situ mechanical material variables. Numerical and experimental verifications were carried out to demonstrate the capability and potential of the proposed ANN constitutive models.

ANN as nonlinear nanoindentation models for metallic systems

In this study, some in-situ nonlinear material parameters at the micro- and nano-scales of metallic materials were effectively coupled with the typical load-displacement nanoindentation test data using a new class of dimensionless ANN constitutive models. Towards that goal, different ANN constitutive models were generated and successfully trained with simulated FEA results. Only the monotonic loading part of the nanoindentation responses for various material systems was used to train the ANN constitutive models. These innovative ANN models included dimensionless input/output variables along with in-situ material parameters, such as stress limits and hardening, so these dimensionless ANNs could cover a wider range of metallic materials than previously proposed ANN models. The predicted ANN nonlinear material behavior and properties were compared with nanoindentation experimental data performed on Cu-ECAE. In addition, inverse problems were performed using the trained ANN to determine in-situ material parameters from given nanoindentation test data. The proposed ANN constitutive models generated accurate nonlinear stress-strain behaviors from the nanoindentation test results. The capability of the proposed ANN modeling approach to effectively and efficiently characterize the in-situ nonlinear material behavior from the nanoindentation test result was demonstrated. The proposed class of ANNs with dimensionless variables can be extended to include different inelastic and damage variables.

ANN as time-dependent constitutive models for polymeric materials

The proposed ANN modeling approach was also used to characterize the in-situ time-dependent material properties of micro- and nano-scaled polymeric materials from nanoindentation load-deflection creep test results. Three ANN constitutive models with different sets of input variables were trained with simulated FEA nanoindentation creep results performed with a wide range of polymeric viscoelastic material parameters. The trained ANNs were compared with experimental and simulated FEA results that were not used in their training. The most successful one among the trained three ANN models had elastic modulus, creep compliances, and logarithmic time as input variables. The output was the deflection. This ANN was effectively used in an inverse-problem to back-calculate the in-situ elastic modulus and creep compliance coefficients from given nanoindentation creep test results of a Polycarbonate polymeric material. The proposed ANN constitutive models are effective and can be used to characterize the material constitutive time-dependent material properties (ANN variables) from creep test results. The proposed ANN constitutive models can be extended to identify more complex time-dependent material parameters at the micro-scale including viscoplastic or nonlinear viscoelastic behaviors.

ANN as anisotropic constitutive models for FRP composites

The proposed ANN modeling approach was used as multi-axial nonlinear ANN constitutive models for macro-scaled FRP composites. The ANN constitutive models were used to generate the nonlinear multi-axial stress-strain response for FRP composites under plane-stress conditions. Different ANN models with a vector and a scalar-type output were generated and trained with experimental data from off-axis tension/compression and pure shear (Arcan) tests. The predictions of the trained ANN models were compared with experimental results especially those that were not used in the training. The trained ANN with a vector output was directly implemented as a user-defined material module in displacement-based and layered shell FE. The new FE-ANN was used to model the response of a notched plate. The ANN was able to provide the needed nonlinear multi-axial

material responses at the Gaussian integration points of each FE. The generated FE-ANN result, i.e., normalized plate load-displacement, was accurate compared to the result of a tested plate made from pultruded FRP E-glass/polyester material. The proposed ANN constitutive models were effectively implemented and could be coupled with FE analysis to provide the multi-axial nonlinear material response. The proposed FE-ANN simulation code can be directly used for the analysis of other layered composite materials and structures.

ANN as micromechanical damage models for FRP composites

The proposed ANN modeling approach was also used as micromechanical damage models for FRP composites. The proposed micromechanical ANN models were successfully trained with simulated FEA results for different damage levels and used to characterize the growth of void damage and its associated energy release rate from stress-strain responses. The trained ANN models were capable of generating effective damage behavior and damage dissipation at different damage levels.

7.2 Future Recommendations

Relatively few ANN constitutive models have been proposed in engineering mechanics compared to the traditional mathematical and analytical models. The early proposed ANN models were limited because they were not fully developed as comprehensive and complete ANN constitutive models. The ANN modeling approach with multi-scale parameters is effective and can overcome the limitations of traditional mathematical and analytical approaches in complex composite material behavior with nonlinear and damage response. Therefore, further studies need to be performed on how to generate more accurate and practical ANN constitutive models based with multi-scale parameters. Specific recommendations for future research are as follows:

The current dimensionless ANN constitutive models to characterize the in-situ material parameters of micro-scaled materials from the nanoindentation test response are more suited to the relatively stiff material that does not include the material softening. The proposed ANN constitutive models can be extended for softer materials by including the softening or damage material parameters as input/output variables. In addition, more practical and general ANN constitutive models can be achieved by training the proposed ANNs with the wider range of material properties.

The current ANN polymeric models for characterizing the in-situ elastic modulus and creep compliances are limited to the effective response of the homogenized material. More practical and sophisticated ANN constitutive models can be developed by including dimensionless input/output variables for various material properties at the micro-structural level. These ANN time-dependent models can be extended to viscoplastic time-dependent material behavior of metallic materials. Nonlinear and rheologically complex viscoelastic behavior can also be achieved using ANN.

The current ANN constitutive models for FRP composites can effectively generate the effective homogenized nonlinear multi-axial stress-strain behavior. However, the proposed ANN constitutive model integrated with an FEA could not fully generate a stable and consistent material response especially at higher strain levels, e.g., in localized stress-concentration areas beyond the training range. In order to be fully coupled the FEA to the proposed ANN models, we need to effectively expand ANN training range. This can be achieved by extending the training data beyond the ultimate state or by adding numerical algorithms to generate a damage material behavior.

The current micromechanical ANN models with damage formulation can effectively generate damage and damage dissipation behavior. However, they are not complete as full constitutive models. The damage formulation needs to be further investigated especially for the case of nonlinear material behaviors combined with interacting damage systems. Based on the current ANN modeling approach

with damage formulation, more effective and general micromechanical ANN models can be further developed.

REFERENCES

Abaqus Analysis User's Manual: Version 6.4. (2003). Abaqus, Inc.

Aboudi, J. (1991). *Mechanics of Composite Materials: A Unified Micromechanical Approach*. Amsterdam: Elsevier.

Abu, A.-R., Rashid, K., & Voyiadjis, G. Z. (2006). A physically based gradient plasticity theory. *International Journal of Plasticity, 22*(4), 654-684.

Al-Haik, M. S., Garmestani, H., & Savran, A. (2004). Explicit and implicit viscoplastic models for polymeric composite. *International Journal of Plasticity, 20*(10), 1875-1907.

Al-Rub, A., K., R., & Voyiadjis, G. Z. (2004). Analytical and experimental determination of the material intrinsic length scale of strain gradient plasticity theory from micro- and nano-indentation experiments. *International Journal of Plasticity, 20*(6), 1139-1182.

Anand, L., & Ames, N. M. (2006). On modeling the micro-indentation response of an amorphous polymer. *International Journal of Plasticity, 22*(6), 1123-1170.

ASTM-D3039/D3039M. (2000). *Standard Test Method for Tensile Properties of Polymeric Matrix Composite Materials*: Annual Book of ASTM standards.

ASTM-D3410/D3410M. (2003). *Standard Test Method for Compressive Properties of Polymeric Matrix Composite Materials with Unsupported Gage Section by Shear Loading*: Annual Book of ASTM standards.

ASTM-D4762. (2004). *Standard Guide for Testing Polymer Matrix Composite Materials*: Annual Book of ASTM standards.

Avery, W. B., & Herakovich, C. T. (1986). Effect of fiber anisotropy on thermal stresses in fibrous composites. *Journal of Applied Mechanics, Transactions ASME, 53*(4), 751-756.

Bansal, S., Saxena, A., & Tummala, R. R. (2004). *Nanocrystalline copper and nickel as ultra high-density chip-to-package interconnections.* Paper presented at the Proceedings-54th Electronic Components and Technology Conference.

Bansal, S., Toimil-Molares, E., Saxena, A., & Tummala, R. R. (2005). *Nanoindentation of single crystal and polycrystalline copper nanowires.* Paper presented at the Proceedings of 55th Electronic Components and Technology.

Begley, J. A., & Landes, J. D. (1972). J integral as a fracture criterion. *ASTM Special Technical Publication*, 1-23.

Bhattacharya, A. K., & Nix, W. D. (1991). Finite element analysis of cone indentation. *International Journal of Solids Structures, 27*(8), 1047-1058.

Caiazzo, A. A., & Costanzo, F. (2000). On the constitutive relations of materials with evolving microstructure due to microcracking. *International Journal of Solids and Structures, 37*(24),

3375-3398.

Caiazzo, A. A., & Costanzo, F. (2000). On the effective elastic properties of composites with evolving microcracking. *Journal of Reinforced Plastics and Composites, 19*(2), 152-163.

Chakraborty, D. (2005). Artificial neural network based delamination prediction in laminated composites. *Materials and Design, 26*(1), 1-7.

Chen, D., Li, M., & Wu, S. (2003). Modeling of microstructure and constitutive relation during superplastic deformation by fuzzy-neural network. *Journal of Materials Processing Technology, 142*(1), 197-202.

Chen, W. F., McCarron, W. O., & Yamaguchi, E. (1994). *Constitutive Equations for Engineering Materials*: John Wiley & Sons.

Chen, W. F., & Saleeb, A. F. (1982). *Constitutive Equations for Engineering Materials*: John and Wiley & Sons.

Choi, Y., Lee, H. S., & Kwon, D. (2004). Analysis of sharp-tip-indentation load-depth curve for contact area determination taking into account pile-up and sink-in effects. *Journal of Materials Research, 19*(11), 3307-3315.

Crisfield, M. A. *Nonlinear Finite Element Analysis of Solids and Structures* (Vol. 1: Essentials). London, UK: John Wiley & Sons.

DARPA Neural Network Study. (1988). Lexington, MA: M.I.T. Lincoln Laboratory.

Demuth, H., Beale, M., & Hagan, M. (2005). *Neural Network Toolbox 5: User's Guide*: The MathWorks, Inc.

Den Toonder, J. M. J., Ramone, Y., Van Dijken, A. R., Beijer, J. G. J., & Zhang, G. Q. (2005). Viscoelastic characterization of low-dielectric constant SiLK films using nanoindentation in combination with finite element modeling. *Journal of Electronic Packaging: Transaction of the ASME, 127*(3), 276-285.

Fang, T. H., & Chang, W. J. (2004). Nanoindentation characteristics on polycarbonate polymer film. *Microelectronics Journal, 35*(7), 595-599.

Feng, G., & Ngan, A. H. W. (2002). Effects of creep and thermal drift on modulus measurement using depth-sensing indentation. *Journal of Materials Research, 17*(3), 660-668.

Fu, Q., Hashash, Y. M. A., Jung, S., & Ghaboussi, J. (2007). Integration of laboratory testing and constitutive modeling of soils. *Computers and Geotechnics, 34*(5), 330-345.

Gerberich, W. W., Mook, W. M., Cordill, M. J., Carter, C. B., Perrey, C. R., Heberlein, J. V., et al. (2005). Reverse plasticity in single crystal silicon nanospheres. *International Journal of Plasticity, 21*(12), 2391-2405.

Ghaboussi, J., Pecknold, D. A., Zhang, M., & Haj-Ali, R. M. (1998). Autoprogressive training of neural network constitute models. *International Journal for Numerical Methods in Engineering, 42*, 105-126.

Ghaboussi, J., & Sidarta, D. E. (1998). New nested adaptive neural networks (NANN) for constitutive modeling. *Computers and Geotechnics, 22*(1), 29-52.

Ghosh, A. K. (1980). Physically-based constitutive model for metal deformation. *Acta Metallurgical, 28*(11), 1443-1465.

Griffin, O. H., Kamat, M. P., & Herakovich, C. T. (1981). Three-dimensional finite element analysis of laminated composites. *Journal of Composite Materials, 15*, 543-560.

Hahn, H. T. (1973). Nonlinear behavior of laminated composites. *Journal of Composite Materials, 7*, 257-271.

Hahn, H. T., & Tsai, S. W. (1973). Nonlinear elastic behavior of unidirectional composite laminate. *Journal of Composite Materials, 7*, 102-118.

Haj-Ali, R., & Kilic, H. (2002). Nonlinear behavior of pultruded FRP composites. *Composites Part B:Engineering, 33*(3), 173-191.

Haj-Ali, R., Kilic, H., & Zureick, A. H. (2001). Three-dimensional micromechanics based constitutive framework for analysis of pultruded composite structures. *ASCE J. Engineering Mechanics, 127*(7), 653-660.

Haj-Ali, R., & Muliana, A. (2004). A multi-scale constitutive framework for the nonlinear analysis of laminated composite materials and structures. *International Journal of Solids and Structures, 40*(13), 3461-3490.

Haj-Ali, R., & Muliana, A. H. (2006). Multiscale nonlinear framework for the long-term behavior of layered composite structures. *Journal of Engineering Mechanics, 132*(12), 1354-1362.

Haj-Ali, R. M., Kilic, H. (2003). Nonlinear constitutive models for pultruded FRP composites. *Mechanics of Materials, 53*, 791-801.

Haj-Ali, R. M., & Muliana, A. H. (2003). A micromechanical constitutive framework for the nonlinear viscoelastic behavior of pultruded composite materials. *International Journal of Solids and Structures, 40*(5), 1037-1057.

Haj-Ali, R. M., & Muliana, A. H. (2004). A multi-scale constitutive formulation for the nonlinear viscoelastic analysis of laminated composite materials and structures. *International Journal of Solids and Structures, 41*(13), 3461-3490.

Haj-Ali, R. M., & Pecknold, D. A. (1996). *Hierarchical material models with microstructure for nonlinear analysis of progressive damage in laminated composite structures* (No. 611): Department of Civil Engineering, University of Illinois at Urbana-Champaign.

Haj-Ali, R. M., Pecknold, D. A., & Ahmad, M. F. (1993). *Combined micromechanical and structural finite element analysis of laminated composites.* Paper presented at the ABAQUS User's conference, Achen, Germany.

Haj-Ali, R. M., Pecknold, D. A., Ghaboussi, J., & Voyiadjis, G. Z. (2001). Simulated micromechanical models using artificial neural networks. *Journal of Engineering Mechanics, 127*(7), 730-738.

Hart, E. W. (1976). Constitutive relations for the nonelastic deformation of metals. *Journal of*

Engineering Materials and Technology: Transactions of the ASME, 98(3), 193-202.

Hashin, Z. (1962). The elastic moduli of heterogeneous materials. *Journal of Applied Mechanics, 29,* 143.

Hashin, Z. (1990). Thermoelastic properties and conductivity of carbon/carbon fiber composites. *Mechanics of Materials, 8*(4), 293-308.

Hashin, Z., & Rosen, B. W. (1964). The elastic moduli of fiber reinforced materials. *Journal of Applied Mechanics, 31,* 223-232.

Hay, J. C., Bolshakov, A., & Pharr, G. M. (1999). Critical examination of the fundamental relations used in the analysis of nanoindentation data. *Journal of Materials Research, 14*(6), 2296-2305.

Hay, J. L., & Pharr, G. M. (Eds.). (2000). *Instrumented Indentation Testing* (Vol. 8: Mechanical Testing and Evaluation).

Herakovich, C. T. (1998). *Mechanics of Fibrous Composites*. New York: John Wiley & Sons.

Hill, R. (1964). Theory of mechanical properties of fiber-strengthened materials. *Journal of the Mechanics and Physics of Solids, 12,* 199-212.

Huber, N., Nix, W. D., & Gao, H. (2002). Identification of elastic-plastic material parameters from pyramidal indentation of thin films. *Proceedings of the Royal Society, A*(458), 1593-1620.

Hwang, K. C., Guo, Y., Jiang, H., Huang, Y., & Zhuang, Z. (2004). The finite deformation theory of Taylor-based nonlocal plasticity. *International Journal of Plasticity, 20*(4-5), 831-839.

Jones, R. M., & Nelson, D. A. R. J. (1975). A new material model for the nonlinear biaxial behavior of ATJ-S Graphite. *Journal of Composite Materials, 9,* 251-265.

Jung, S., & Ghaboussi, J. (2006). Neural network constitutive model for rate-dependent materials. *Computers & Structures, 84*(15-16), 955-963.

Knott, T. W., & Herakovich, C. T. (1988). *Effect of fiber morphology on composite properties.* Paper presented at the CCMS-88-09, VPI-E-88-16, Virginia Tech, Blacksburg.

Knott, T. W., & Herakovich, C. T. (1991). Effect of fiber orthotropy on effective composite properties. *Journal of Composite Materials, 25*(6), 732-759.

Landes, J. D., & Begley, J. A. (1972). Effect of specimen geometry on J//I//c. *ASTM Special Technical Publication,* 24-39.

Lemaitre, J. (1992). *A Course on Damage Mechanics*. Berlin, Germany: Springer-Verlag.

Lin, C.-T., & Lee, C. S. G. (1996). *Neural Fuzzy Systems: A Neuro-Fuzzy Synergism to Intelligent Systems*. Upper Saddle River, NJ: Prentice Hall.

Lu, H., Wang, B., Ma, J., Huang, G., & Viswanathan, H. (2003). Measurement of creep compliance of solid polymers by nanoindentation. *Mechanics Time-Dependent Materials, 7*(3-4), 189-207.

Malvern, L. E. (1969). *Introduction to the Mechanics of a Continuous Medium*. Englewood Cliffs, NJ:

Prentice-Hall.

Matthews, F. L., & Rawlings, R. D. (1994). *Composite Materials: Engineering and Science*. London SE1 8HK, UK: Chapman & Hall.

Maugin, G. A. (2000). On the universality of the thermomechanics of forces driving singular sets. *Archive of Applied Mechanics, 70*(1-3), 31-45.

Muliana, A., & Haj-Ali, R. (2005). Multiscale modeling for the long-term behavior of laminated composite structures. *AIAA Journal, 43*(8), 1815-1822.

Muliana, A., Steward, R., Haj-Ali, R. M., & Saxena, A. (2002). Artificial neural network and finite element modeling of nanoindentation tests. *Metallurgical and Materials Transactions A (Physical Metallurgy and Materials Science), 33A*(7), 1939-1947.

Muliana, A. H., & Haj-Ali, R. M. (2004). Nested nonlinear viscoelastic and micromechanical models for the analysis of pultruded composite materials and structures. *Mechanics of Materials, 36*(11), 1087-1110.

Okafor, A. C., Chandrashekhara, K., & Jiang, Y. P. (1996). Delamination prediction in composite beams with built-in piezoelectric devices using modal analysis and neural network. *Smart Materials and Structures, 5*(3), 338-347.

Oliver, W. C., & Pharr, G. M. (1992). An improved technique for determining hardness and elastic modulus using load and displacement sensing indentation experiments. *Journal of Material Response, 7*(6), 1564-1583.

Ootao, Y., Tanigawa, Y., & Nakamura, T. (1999). Optimization of material composition of FGM hollow circular cylinder under thermal loading: A neural network approach. *Composites Part B: Engineering, 30*(4), 415-422.

Oyen, M. L. (2005). Spherical indentation creep following ramp loading. *Journal of Materials Research, 20*(8), 2094-2100.

Oyen, M. L., & Cook, R. F. (2003). Load-displacement behavior during sharp indentation of viscous-elastic-plastic materials. *Journal of Materials Research, 18*(1), 139-150.

Paley, M., & Aboudi, J. (1992). Micromechanical analysis of composites by the generalized cells model. *Mechanics of Materials, 14*(2), 127-139.

Pan, H., Thamburaja, P., & Chau, F. S. (2007). Multi-axial behavior of shape-memory alloys undergoing martensitic reorientation and detwinning. *International Journal of Plasticity, 23*(4), 711-732.

Panich, N., & Sun, Y. (2004). Effect of penetration depth on indentation response of soft coatings on hard substrates: a finite element analysis. *Surface and Coatings Technology, 182*(2-3), 342-350.

Paul, B. (1960). Prediction of elastic constants of multiphase materials. *Transactions of AIME, 218*, 36-41.

Petit, P. H., & Waddoups, M. E. (1969). A method of predicting the nonlinear behavior of laminated

composites. *Journal of Composite Materials, 3*, 2-19.

Pidaparti, R. M. V., & Palakal, M. J. (1993). Material model for composites using neural networks. *AIAA Journal, 31*(8), 1533-1535.

Pindera, M. J., & Herakovich, C. T. (1983). *An endochronic model for the response of unidirectional composites under off-axis tensile load.* Paper presented at the Proceedings IUTAM symposium on Mechanics of Composite Materials.

Qu, S., Huang, Y., Pharr, G. M., & Hwang, K. C. (2006). The indentation size effect in the spherical indentation of iridium: A study via the conventional theory of mechanism-based strain gradient plasticity. *International Journal of Plasticity, 22*(7), 1265-1286.

Reuss, A. (1929). Calculation of flow limits of mixed crystals on basis of plasticity of monocrystals

Berechnung der Fliessgrenze von Mischkristalle. *Zeitschrift fuer Angewandte Mathematik und Mechanik, 9*(1), 49-58.

Sakai, M., & Shimizu, S. (2001). Indentation rheometry for glass-forming materials. *Journal of Non-Crystalline Solids, 282*(2-3), 236-247.

Sankarasubramanian, G., & Rajasekaran, S. (1996). Constitutive modeling of concrete using a new failure criterion. *Computers and Structures, 58*(5), 1003-1014.

Sidarta, D. E., & Ghaboussi, J. (1998). Constitutive modeling of geomaterials from non-uniform material tests. *Computers and Geotechnics, 22*(1), 53-71.

Simo, J. C., & Hughes, T. J. R. (2000). *Computational Inelasticity*: Springer.

Steinberg, D. J., Cochran, S. G., & Guinan, M. W. (1980). A constitutive model for metals applicable at high-strain rate. *Journal of Applied Physics, 51*(3), 1498-1504.

Sun, C. T., & Chen, J. L. (1989). A simple flow rule for characterizing nonlinear behavior of fiber composites. *Journal of Composite Materials, 23*, 1009-1020.

Sun, Y., Bell, T., & Zheng, S. (1995). Finite element analysis of the critical ratio of coating thickness to indentation depth for coating property measurements by nanoindentation. *Thin Solid Films, 258*(1-2), 198-204.

Swearengen, J. C., Rohde, R. W., & Hicks, D. L. (1976). Mechanical state relations for inelastic deformation of iron: The choice of variables. *Acta Metallurgical, 24*, 969-975.

Tho, K. K., Swaddiwudhipong, S., Liu, Z. S., & Hua, J. (2004). Artificial neural network model for material characterization by indentation. *Modeling and Simulation in Materials Science and Engineering, 12*(5), 1055-1062.

TriboIndenter User's Manual. (2001). Minneapolis, MN 55439: Hysitron Inc.

Tyulyukovskiy, E., & Huber, N. (2006). Identification of viscoplastic material parameters from spherical indentation data: Part I. Neural networks. *Journal of Materials Research, 21*(3), 664-676.

VanLandinham, M. R., Villarrubia, J. S., Guthrie, W. F., & Meyers, G. F. (2001). *Nanoindentation of polymers: An overview*. Paper presented at the Macromolecular Symposia.

Vlachos, D. E., Markopoulos, Y. P., & Kostopoulos, V. (2001). 3-D modeling of nanoindentation experiment on a coating-substrate system. *Computational Mechanics, 27*(2), 138-144.

Voigt, W. (1889). Uber die beziehung zwischen den beiden elastizitatskonstanten isotroper korper. *Wied Ann, 38*, 573-587.

Wasserman, P. D. (1989). *Neural Computing: Theory and Practice*. New York: Van Nostrand Reinhold.

Wei, Y., Shu, S., Du, Y., & Zhu, C. (2005). Size, geometry and nonuniformity effects of surface-nanocrystalline aluminum in nanoindentation test. *International Journal of Plasticity, 21*(11), 2089-2106.

Wilkins, M. L., & Guinan, M. W. (1973). Impact of cylinders on a rigid boundary. *Journal of Applied Physics, 44*(3), 1200-1206.

Wire, G. L., Ellis, F. V., & Li, C. Y. (1975). Work hardening and mechanical equation of state in some metals in monotonic loading. *Acta Metallurgical, 24*, 677-685.

XYZ Scientific Applications, I. (1999). *TrueGrid Mannual: Version 2.1.0*: XYZ Scientific Applications, Inc.

Yang, S., Zhang, Y. W., & Zeng, K. (2004). Analysis of nanoindentation creep for polymeric materials. *Journal of Applied Physics, 95*(7), 3655-3666.

Zhang, C. Y., Zhang, Y. W., & Zeng, K. Y. (2004). Extracting the mechanical properties of a viscoelastic polymeric film on a hard elastic substrate. *Journal of Materials Research, 19*(10), 3053-3061.

Zhang, F., Saha, R., Huang, Y., Nix, W. D., Hwang, K. C., Qu, S., et al. (2007). Indentation of a hard film on a soft substrate: Strain gradient hardening effects. *International Journal of Plasticity, 23*(1), 25-43.

Zhang, Z., Klein, P., & Friedrich, K. (2002). Dynamic mechanical properties of PTFE based short carbon fibre reinforced composites: Experiment and artificial neural network prediction. *Composites Science and Technology, 62*(7-8), 1001-1009.

VITA

Hoan-Kee Kim was born on November 23, 1975 in Seoul, Korea. He received his Bachelor and Master of Science in Civil & Environmental Engineering from Hanyang University (Korea) in 2000 and 2002, respectively. His master's thesis was on the development of optimum structural design program for Pre-stressed concrete (PSC) box girder bridges using genetic algorithms. In fall 2003, he joined the School of Civil & Environmental Engineering at Georgia Institute of Technology in Atlanta to pursue a doctorate in the area of computational mechanics of isotropic and anisotropic structural engineering materials, such as metallic, polymeric, and fiber reinforced composite materials. Selected publications during the PhD program at Georgia Tech are listed as follows:

Kim, H.K., Haj-Ali, R., and Muliana, A., "Nanoindentation creep simulations and identification of viscoelastic material properties using artificial neural networks," *International Journal for Numerical Methods in Engineering*, (Submitted)

Haj-Ali, R. and **Kim, H.K.**, "Nonlinear constitutive models for FRP composites using artificial neural networks," *Mechanics of Materials*, 39(12), Dec. 2007, p1035-1042.

Haj-Ali, R., **Kim, H.K.**, Koh, S.W., Saxena, A., and Tummala, R., "Nonlinear constitutive models from nanoindentation tests using artificial neural networks," *International Journal of Plasticity*, 24(3), Mar. 2008, p371-396.

Kim, H.K., and Haj-Ali, R., "Nonlinear FRP Constitutive Models using Artificial Neural Networks and their Integration in FE Analysis of Composite Structures," *18th ASCE Engineering Mechanics Division Conference*, Blacksburg, VA, June 2007.

Kim, H.K., Haj-Ali, R., and Muliana, A. "Nanoindentation Simulations and Material Identifications using Artificial Neural Networks," *The 7th World Congress on Computational Mechanics (WCCM-7)*, Hyatt Regency Century Plaza Hotel, Los Angeles, CA, July 2006.

Kim, H.K., Johnson, S., El-Hajjar, R., and Haj-Ali, R. "Infrared Thermography for Fatigue Damage Detection in Thick-Section FRP Composites," *The 2nd International Conference on ICSCS*, Seoul, Korea, Sept. 2004.